

# Autonomous Jumping Microrobots

*Sarah Elizabeth Bergbreiter*



Electrical Engineering and Computer Sciences  
University of California at Berkeley

Technical Report No. UCB/EECS-2007-159

<http://www.eecs.berkeley.edu/Pubs/TechRpts/2007/EECS-2007-159.html>

December 18, 2007

Copyright © 2007, by the author(s).  
All rights reserved.

Permission to make digital or hard copies of all or part of this work for personal or classroom use is granted without fee provided that copies are not made or distributed for profit or commercial advantage and that copies bear this notice and the full citation on the first page. To copy otherwise, to republish, to post on servers or to redistribute to lists, requires prior specific permission.

**Autonomous Jumping Microrobots**

by

Sarah Elizabeth Bergbreiter

B.S.E. (Princeton University) 1999

M.S. (University of California, Berkeley) 2004

A dissertation submitted in partial satisfaction of the  
requirements for the degree of  
Doctor of Philosophy

in

Engineering-Electrical Engineering and Computer Sciences

in the

GRADUATE DIVISION

of the

UNIVERSITY OF CALIFORNIA, BERKELEY

Committee in charge:

Professor Kristofer S. J. Pister, Chair

Professor Ronald S. Fearing

Professor Robert J. Full

Fall 2007

The dissertation of Sarah Elizabeth Bergbreiter is approved:

---

Chair

Date

---

Date

---

Date

University of California, Berkeley

Fall 2007

# Autonomous Jumping Microrobots

Copyright 2007

by

Sarah Elizabeth Bergbreiter

## Abstract

Autonomous Jumping Microrobots

by

Sarah Elizabeth Bergbreiter

Doctor of Philosophy in Engineering-Electrical Engineering and Computer Sciences

University of California, Berkeley

Professor Kristofer S. J. Pister, Chair

An autonomous jumping microrobot has been designed, and its mechanical components have been fabricated and tested. Millimeter-scale autonomous mobile microrobots have potential applications in mobile sensor networks as well as search and exploration tasks. However, mobility is difficult at this scale due to rugged surfaces, obstacles and locomotion efficiency. Jumping has been proposed as a locomotion method to overcome these challenges.

The microrobot design has been divided into four components: energy storage, high work density actuators, power, and control. Like its biological inspiration, the flea, a jumping microrobot requires an energy storage mechanism to store energy and release it quickly to jump. Small leg lengths require large accelerations to reach takeoff velocities required to jump 10s of cm. Silicone micro rubber bands have been fabricated and demonstrated to store and quickly release enough energy for a 10 mg robot to jump 17 cm straight

up.

To stretch these micro rubber bands, electrostatic inchworm motors have been designed and fabricated to provide high forces and large displacements with low input power requirements. Three key design innovations have been used to improve the force density of these motor designs  $37x$  over previous efforts. First, a pre-biasing actuator reduces initial electrostatic gaps below lithographic limits. Second, a toothless, friction-based clutch allows for variable step sizes and single drive actuator motors. Third, silicon nitride has been added to reduce motor size. Initial motor designs using these three new features have been fabricated and tested.

Finally, several prototypes have been built to integrate and test the four robot components. A small-scale version of the full robot with previously fabricated solar cells and an off-the-shelf microcontroller driving a small inchworm motor has been demonstrated. Separately, an inchworm motor has been used to store energy in a micro rubber band for quick release. It is hoped that many of the design and fabrication ideas presented in this work can be used to make autonomous mobile microrobots a reality.

---

Professor Kristofer S. J. Pister  
Dissertation Committee Chair

# Contents

<b>List of Figures</b>	<b>iii</b>
<b>List of Tables</b>	<b>vi</b>
<b>1 Introduction</b>	<b>1</b>
1.1 Motivation and Applications . . . . .	4
1.1.1 Sensor Networks and Robots . . . . .	4
1.1.2 Applications for Mobile Sensor Networks . . . . .	6
1.1.3 Applications for Microrobots and their Components . . . . .	7
1.2 Previous Work . . . . .	8
1.2.1 Microrobots . . . . .	8
1.2.2 Jumping Robots . . . . .	11
1.2.3 Biology . . . . .	13
<b>2 Robot Locomotion and Design</b>	<b>17</b>
2.1 Scaling . . . . .	19
2.1.1 Drag . . . . .	20
2.1.2 Power and Acceleration . . . . .	26
2.2 Jumping Locomotion . . . . .	32
2.2.1 Obstacle Avoidance . . . . .	32
2.2.2 Locomotion Efficiency . . . . .	33
2.3 Robot Component Requirements . . . . .	43
2.3.1 Energy Storage . . . . .	44
2.3.2 Actuation . . . . .	45
2.3.3 Power . . . . .	46
2.3.4 Control . . . . .	47
<b>3 Micromechanical Energy Storage</b>	<b>48</b>
3.1 Design . . . . .	49
3.1.1 Energy Density . . . . .	50
3.1.2 Spring Efficiency . . . . .	52
3.1.3 Spring Fabrication . . . . .	57

3.1.4	Spring Integration . . . . .	60
3.1.5	Spring Design Summary . . . . .	61
3.2	Fabrication . . . . .	62
3.2.1	Silicon Fabrication . . . . .	63
3.2.2	Elastomer Fabrication . . . . .	65
3.2.3	Elastomer Assembly . . . . .	69
3.2.4	Pre-Strain . . . . .	70
3.3	Characterization and Results . . . . .	72
3.3.1	Force-Displacement Curves . . . . .	72
3.3.2	Elongation at Break . . . . .	75
3.3.3	Quick Release . . . . .	77
<b>4</b>	<b>High Work Density Motors</b>	<b>80</b>
4.1	Design . . . . .	84
4.1.1	Motor Travel . . . . .	86
4.1.2	Force Density . . . . .	87
4.1.3	Motor Design Summary . . . . .	102
4.2	Fabrication . . . . .	103
4.2.1	Froghopper Process . . . . .	103
4.2.2	Layout Guidelines . . . . .	107
4.3	Characterization and Results . . . . .	112
4.3.1	Process Characterization . . . . .	113
4.3.2	Motor Characterization . . . . .	116
<b>5</b>	<b>Power, Control, and Integration</b>	<b>118</b>
5.1	Power . . . . .	119
5.2	Control . . . . .	122
5.3	Integration . . . . .	124
5.4	Prototypes . . . . .	125
5.4.1	Solar Cells, Microcontroller, and Inchworm Motor . . . . .	126
5.4.2	Inchworm Motor and Micro Rubber Band . . . . .	127
5.4.3	Final Robot Mockup . . . . .	128
<b>6</b>	<b>Conclusions and Future Work</b>	<b>129</b>
6.1	New Locomotion Paradigms . . . . .	130
6.2	New Fabrication Techniques . . . . .	131
6.3	New Component Applications . . . . .	134
	<b>Bibliography</b>	<b>137</b>

# List of Figures

1.1	Sensor Networks and Robots . . . . .	5
1.2	Previous Work in Microrobots . . . . .	9
1.3	A 10 mg Solar-Powered Microrobot . . . . .	10
1.4	Previous Work in Jumping Robots . . . . .	11
1.5	Oriental Rat Flea and Froghopper . . . . .	14
2.1	Jumping Trajectories with Different Initial Kinetic Energies . . . . .	18
2.2	Height v. Length for Various Robots and Insects Demonstrating Drag Losses. . . . .	21
2.3	Jumping Trajectories with Different Initial Kinetic Energies and Drag . . . . .	22
2.4	Optimal Mass . . . . .	25
2.5	Optimal Angle . . . . .	26
2.6	Jumping Robot Model. . . . .	27
2.7	Height v. Length for Various Robots and Insects Demonstrating High Powers Required. . . . .	28
2.8	Jumping Robot Model Position and Acceleration. . . . .	30
2.9	Jumping Robot Model Velocity and Power. . . . .	31
2.10	Simple Walking Microrobot Model . . . . .	35
2.11	Simple Wheeled Microrobot Model . . . . .	37
2.12	Simple Running Microrobot Model . . . . .	39
2.13	Force/Displacement Requirements for a Linear Spring . . . . .	45
3.1	Strain Energy in Bending and Tension. . . . .	50
3.2	Force/Distance Tests for Latex and Polyurethane. . . . .	54
3.3	Energy Delivered from Linear and Constant Force Springs. . . . .	56
3.4	Linear Spring in a Nonlinear Force/Distance Profile Configuration. . . . .	57
3.5	Nonlinear Spring Force. . . . .	58
3.6	Silicon Hook for Assembling Micro Rubber Bands. . . . .	64
3.7	Two Mask SOI Process for Fabricating Silicon Components. . . . .	64
3.8	Laser Cutting Process . . . . .	66
3.9	Laser Cut Rubber Bands . . . . .	67
3.10	Elastomer Molding Process . . . . .	68
3.11	Molded Rubber Bands . . . . .	69

3.12	Silicon Hook with Assembled Elastomer . . . . .	69
3.13	Tethered Moving Part Before Assembly . . . . .	70
3.14	Effect of Fabricated Pre-strain on Energy Storage with Stiffer Springs . . . . .	71
3.15	Effect of Fabricated Pre-strain on Energy Storage with More Compliant Springs . . . . .	72
3.16	Force/Distance Test Structure for Characterizing Micro Rubber Bands . . . . .	73
3.17	Force/Displacement Curves for Laser Cut Micro Rubber Bands . . . . .	74
3.18	Force/Displacement Curves for Molded Micro Rubber Bands . . . . .	75
3.19	Elongation at Break Tests for Laser Cut and Molded Micro Rubber Bands . . . . .	76
3.20	Test Structure for Quick Release of Energy from Energy Storage System . . . . .	77
3.21	Before and After Frames from Quick Release Test Video . . . . .	78
4.1	Actuator Force Density v. Displacement . . . . .	81
4.2	Actuator Force Density v. Velocity . . . . .	83
4.3	Inchworm Motor Operation . . . . .	85
4.4	Assembled Staples to Increase Motor Travel . . . . .	86
4.5	Cell Size for a Gap Closing Actuator . . . . .	87
4.6	Aspect Ratio and Lithographic Limitations in GCA Actuators . . . . .	90
4.7	Pre-Biasing Transmission Design . . . . .	91
4.8	Gear Teeth on Inchworm Motor Shuttle . . . . .	94
4.9	New Inchworm Motor Operation with Friction Clutch . . . . .	96
4.10	Electrostatic v. Flexure Clutch Forces . . . . .	97
4.11	Friction Clutch Preset . . . . .	99
4.12	Integrated Nitride Gap Stops . . . . .	100
4.13	Two Approaches to Mechanical Connection with Electrical Isolation . . . . .	101
4.14	New Inchworm Motor Layout . . . . .	102
4.15	Frogopper Process Including Nitride Isolation . . . . .	104
4.16	Silicon Nitride Trench Etch . . . . .	105
4.17	Low-Stress Silicon Nitride Deposition . . . . .	106
4.18	Nitride Trenches After Oxide Release . . . . .	107
4.19	Effect of Lateral Etch on Fabricated Devices . . . . .	108
4.20	Fabricated Transmission Interface . . . . .	109
4.21	Fabricated Friction Clutch . . . . .	109
4.22	Fabricated Silicon Nitride Gap Stops . . . . .	111
4.23	Fabricated Silicon Nitride Bump . . . . .	112
4.24	Pull-In Test with Varied Gap Stop Spacing . . . . .	113
4.25	Coefficient of Friction Test Structure . . . . .	114
4.26	Fabricated Inchworm Motor . . . . .	116
4.27	Frames from New Inchworm Motor Operation . . . . .	117
5.1	High Voltage Solar Cells . . . . .	120
5.2	EM6580 Programmable Microcontroller . . . . .	123
5.3	Microrobot Assembly through Wirebonds . . . . .	124
5.4	Flexible Printed Circuit Board for Microrobot Assembly . . . . .	125
5.5	System Integration Test . . . . .	126
5.6	Inchworm Motor Stretching a Micro Rubber Band . . . . .	127

5.7	Fully Integrated Mockup . . . . .	128
6.1	Proposed Silicon/Elastomer Process . . . . .	133
6.2	Microjet Injector . . . . .	134
6.3	Inchworm Motor Robot Crawling along a Wire . . . . .	135

# List of Tables

1.1	Comparison of Jumping Robots with Proposed Microrobot. . . . .	13
1.2	Comparison of Jumping Insects with Proposed Microrobot. . . . .	15
2.1	Comparison of Jumps in Vacuum and Air. . . . .	24
2.2	Comparison of Kinetic Energy at Take-off and Landing. . . . .	24
2.3	Scale Dependence of Takeoff Variables. . . . .	29
2.4	Comparison of Microrobots Overcoming Obstacles. . . . .	33
2.5	Ideal Cost of Transport for Locomotion Models . . . . .	41
2.6	Cost of Transport for Microrobots. . . . .	42
2.7	Target Sizes for Robot Components . . . . .	43
3.1	Possible Spring Material Characteristics . . . . .	50
3.2	Fabrication Complexity for Spring Materials and Designs . . . . .	59
3.3	Spring Sizes for Different Materials in Tension . . . . .	60
3.4	Motor Forces Required by Spring Designs . . . . .	61
3.5	Spring Design Tradeoff Summary . . . . .	62
4.1	Clutch Area Based on Coefficient of Friction . . . . .	98
4.2	New Inchworm Motor Design Summary. . . . .	103
5.1	Power Requirements for Autonomous Jumping Microrobot . . . . .	121

## Acknowledgments

There are countless people to thank, but not enough space or time to thank them all. If I forgot major or minor contributors, I apologize in advance. First I would like to thank my advisor, Professor Kris Pister. His enthusiasm has helped push my knowledge and efforts beyond what I originally would have thought possible. I would also like to thank my qualifying exam and dissertation committees for their guidance and support – Professor Ron Fearing, Professor Bob Full, and Professor Shankar Sastry.

More thanks go to Seth Hollar and Anita Flynn for allowing me to tag along on their initial microrobot adventure during my first couple years. Not only did I gain valuable insight on building microrobots, I also picked up the Microlab and engineering intangibles that both of them possessed. Anita has continued to be an excellent mentor throughout my years in graduate school and I feel very fortunate to have come across her path.

Speaking of the UC Berkeley Microlab, countless microlab students have taught and entertained me over the last five years. In particular, Matt Last possessed an enormous amount of fabrication expertise and I was lucky to capture even a small fraction of it. He was also a constant presence at design reviews and provided many comments and ideas used in this dissertation. Many more BSAC students helped point me in the right direction on more than one occasion. The Microlab staff were also instrumental in setting up some of my more bizarre microlab needs – especially Phill Guillory. Overall, the UC Berkeley Microlab provided an outstanding wealth of fabrication knowledge and equipment for testing new ideas in MEMS and microrobotics.

I would also like to thank all of the graduate and undergraduate students in 471

Cory. Subramaniam Venkatraman helped read through this dissertation and was a fun cycling partner. Steven Lanzisera has been a great friend and I always feel better after telling him about my triumphs and defeats, but we can never drink together again. Ankur Mehta did a good job of pushing me beyond my boundaries for fear and provided solace when the Bears crashed and burned on the football field. Brett, Lixia, Seth, Lance, Brian, Matt, Steven, Chinwuba, Subbu, Mike, Ankur, Ben, Kaz, and Erika have provided both insight in group meetings and lots of laughs and fun outside of work. I've been lucky enough to have several undergraduate students contribute to this dissertation as well. Stratos, Leo, and Deepa helped me refine my own mentoring skills and also contributed test setups and new results for this dissertation and other papers.

I've also enjoyed talking with students in Ron Fearing's and Shankar Sastry's labs over the years. Aaron Hoover proved to be invaluable in helping me to laser cut micro rubber bands. Bruno Sinopoli and Phoebus Chen kept me in contact with the world of control and sensor networks. Erik, Ranjana, Rob, Srinath, and Rick also provided lots of discussions on micro and milli robots.

Finally, I would like to thank my family. I couldn't have gotten to this point without my parents, Dave and Lynne, and my sister Amy and our numerous secret sister chats. As a chemist, my father helped re-teach me many of the things I had forgotten since high school. My in-laws have provided tremendous enthusiasm for my work and I've always loved talking to them about it. Most of all, I'd like to thank my husband Joe. Not only has he suffered through countless descriptions of my research, late nights, and read more papers than he should have, I most definitely couldn't have done it without him.

# Chapter 1

## Introduction

Despite their relative simplicity, modern day mobile robots capture the imagination by offering mobility in robust and controllable packages. While it would have been an enormous challenge to send humans to Mars, the Mars exploration rovers, Spirit and Opportunity, have done the job of exploring the planet in our place [1]. Search and rescue robots from the University of South Florida were used to search for disaster survivors during 9/11 in situations too difficult or dangerous for humans [2]. In addition, mobile robots are beneficial in situations non-dangerous to humans as well. Instead of saving lives, the Roomba<sup>®</sup> from iRobot<sup>®</sup> saves people from tedious vacuuming [3].

Each of these robots is relatively large and works alone or requires a human operator. Science fiction novels have long imagined very small robots working by themselves or in groups to do the same tasks of a larger robot, or even accomplishing jobs much larger robots would find impossible. In *The Diamond Age*, Neal Stephenson describes microscopic robots used for surveillance and inherent in everyday life [4]. Michael Crichton depicted micro-

robots which could assemble other microrobots, as well as swarm together to create larger organisms in *Prey* [5]. In a non-fictional context, Richard Feynman proposed very small micromachines working together as microfactories during his famous 1959 talk “There’s Plenty of Room at the Bottom,” and even offered a reward for the first functioning electric micromotor [6]. Tiny mobile robots, and in particular, many tiny mobile robots networked together can theoretically accomplish feats that large autonomous mobile robots cannot.

A great deal of progress has been made in the decades since Feynman’s speech, but microrobots still have a long way to go to reach the fantastic capabilities attributed to them in fictional works and Feynman’s imagination. Even the term ‘microrobot’ is not well defined. In 1992, Dario defined a microrobot as robot sized on the order of a few cubic microns [7]. In 1997, a paper from his lab was titled “A One Cubic Centimeter Mobile Microrobot with a Steering Control” [8]. While Dario’s definitions are still quite useful, it is important to note that in the same lab, the length scale of a microrobot could vary 4 orders of magnitude! The autonomous mobile microrobots in this dissertation are defined as robots with dimensions on the order of millimeters and feature sizes on the order of microns. They carry power and control on-board for autonomy and their mobility allows them to move through a specified (and preferably arbitrary) environment.

Given this definition, many challenges still remain to accomplish the goal of this work – the design and fabrication of autonomous mobile microrobots. At this size, even mobility proves difficult. Ants and other insects can easily crawl over obstacles, but it is much more difficult for robots to do so, even at larger size scales. To overcome the limitation of leg length, the microrobots of this dissertation are designed to jump over obstacles instead.

Building the robots is another non-trivial problem. Micromotors and micromechanisms are not available off-the-shelf, and microrobot components still need to be custom-fabricated – often a tedious and expensive process. While there are no off-the-shelf components available, this work will show that high work density motors and interesting mechanisms for jumping can be fabricated in a relatively simple process. Finally, these components need to be integrated with a power supply and a controller to build a fully functional microrobot. The autonomous jumping microrobots in this dissertation are powered by solar cells and controlled by an off-the-shelf programmable microcontroller.

This dissertation begins with the motivation for building autonomous jumping microrobots as well as application scenarios in which autonomous jumping microrobots would be particularly useful. Because this work draws from other fields in addition to microrobots, previous work in jumping robots and previous research in biology on jumping insects is also discussed in Chapter 1. Chapter 2 describes the design and analysis of the newly proposed autonomous jumping microrobot and describes in detail many of the new challenges that jumping entails. A discussion of the design, fabrication, and results of a micromechanical energy storage system used for jumping is provided in Chapter 3, and Chapter 4 highlights the high work density motors used to drive the robot. The power and control systems on this microrobot as well as their integration with the other robot components are described in Chapter 5. Finally, conclusions are drawn and many of the future directions provided by this research are detailed in Chapter 6.

## 1.1 Motivation and Applications

When the field of MicroElectroMechanical Systems (MEMS) was in its infancy, the dream of finally building the very small robots science fiction promised did not appear far from reality. MEMS, along with advances in integrated circuit design, offered sensing, actuation, and a lot of computing power all in very small packages. If all of these pieces could be put together, microrobots would be feasible. In fact, the dream of building microrobots using MEMS technologies encouraged the IEEE Robotics and Automation Society to sponsor a 1987 workshop on Micro Robots and Teleoperators in Hyannis, MA which eventually transitioned into the IEEE MEMS conference [9].

### 1.1.1 Sensor Networks and Robots

While MEMS was improving microrobot components like motors and sensors, integrating the motors, sensors, power supplies, and controllers together still proved to be quite difficult. Consequently, Warneke simplified the problem by removing the actuators and legs to create Smart Dust [10]. Smart Dust combined many of the parts required to build a networked microrobot including a microcontroller, sensors, communication, and solar cells all in a  $16 \text{ mm}^3$  package. Much like their microrobot counterparts, the idea of thousands of dust-sized sensors networked together was so powerful that a commercially available off-the-shelf (COTS) version of Smart Dust soon followed [11]. COTS Dust and TinyOS, a compact operating system designed to support large numbers of networked sensors, soon enabled countless applications for sensor networks from surveillance to environmental monitoring [12, 13].

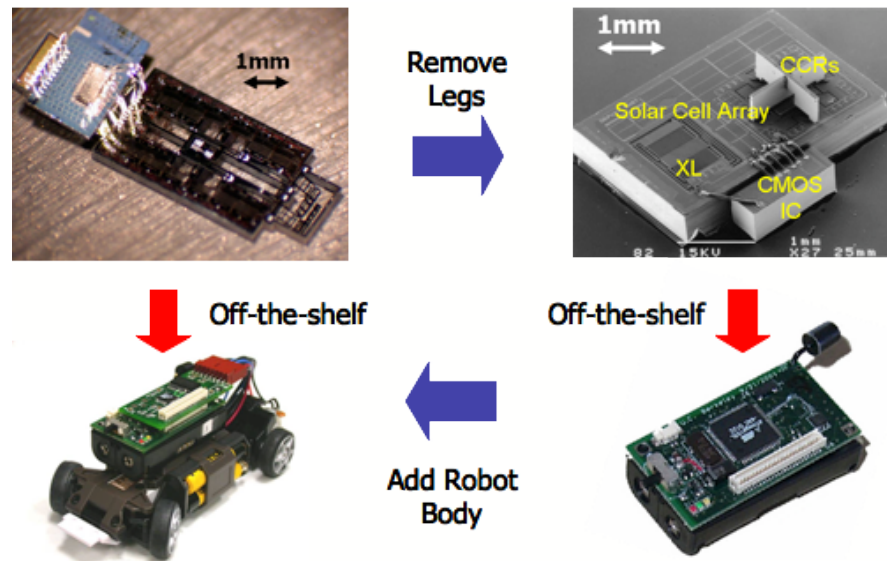


Figure 1.1: Sensor Networks and Robots. Even though microrobots were first proposed early on, they proved difficult to build. By removing the legs, Smart Dust was born and off-the-shelf sensor networks came soon after. Providing a parallel in the robot world, the CotsBots were built from off-the-shelf Smart Dust (COTS Dust).

However, as researchers began deploying the first large-scale sensor networks, they soon discovered an important component was missing – mobility. Once a sensor network was deployed, it was often desirable to move the sensors around to obtain a higher resolution sensor map of a particular event or move more capable sensors to where they were most needed [14]. Similar to COTS Dust, an off-the-shelf approach for mobile sensors followed with the CotsBots [15]. The goal behind the CotsBots was to provide a platform to easily research the application space for many small, networked robots – an application space that would be critical for the original and still elusive goal of autonomous mobile microrobots. Figure 1.1 shows the inter-relationships between sensor networks and mobile robots.

### 1.1.2 Applications for Mobile Sensor Networks

Merging mobile robots with sensor networks enhances many of the applications enabled by static sensor networks in areas like search and rescue, surveillance, and environmental monitoring. Autonomous robots can be used within a sensor network to detect interesting events at higher resolution or move more capable sensors into better positions. This idea was demonstrated for a security application in [12]. A static sensor network composed of 100s of sensor nodes communicated the location of ‘evaders’ in the network to mobile robots acting as ‘pursuers’. For environmental monitoring, Hamilton demonstrated the utility of mobile sensors by stringing cable robots between trees [13]. These mobile robots used cameras with greater efficiency and utility than would have been possible with static sensors to capture more information about changes in the environment.

As the size of sensors shrink to sub-millimeter scales, an important research challenge remains to shrink the size of the robots carrying these sensors within mobile sensor networks. Stealth requires that the robot or mobile sensor is hidden from the object or person being monitored. Small mobile sensors also minimize environmental impact and remain out of sight for environmental monitoring. In one of the first environmental monitoring applications on Great Duck Island in Maine, the birds being monitored took great offense to the sensors and reacted by burying them and pecking off the LEDs [16]. Those sensors that weren’t buried often had their antennas chomped off by hares enjoying the taste of plastic. All of the animals being monitored undoubtedly behaved differently in the presence of sensors.

### 1.1.3 Applications for Microrobots and their Components

While microrobots integrated with sensor networks facilitate a number of the scenarios described above, the microrobots themselves are useful in their own applications as well. One example is search and rescue; very small mobile robots can reach places and possible survivors that larger robots might not. This could be particularly important in search and rescue situations where mobile sensors or robots might want to move through small cracks after an initial scatter deployment. In addition to search and rescue, microrobots also provide a unique opportunity for planetary research and exploration. 17.4 million 10 mg microrobots could replace the 174 kg Spirit rover used to explore Mars, where jumping would be particularly advantageous in low gravity environments. Jumping microrobots also have the unique ability to attach themselves to larger mobile hosts, much like a flea on a dog. This approach could lead to a quick method of deploying sensors or a fairly insidious way of tracking people or other moving objects.

The robots themselves do not provide the only applications for this work however. The components used to build the robots enable their own applications. In addition to their use for autonomous jumping microrobots, the energy storage system used to store the energy for a jump could be used as a high power injector, MEMS catapult or for any other MEMS application requiring a high mechanical output power for a short period of time. High force, large displacement actuators have application beyond microrobots as well. Actuators matching these characteristics will soon be introduced to cell phone cameras for autofocus and zoom capabilities [17] and can also be used for medical or biological manipulation [18]. While applications for jumping microrobots might still be the work of science fiction for

the near future, the components used to build these microrobots could have immediate use today.

## 1.2 Previous Work

A great deal of previous research has influenced this dissertation. Many groups have designed and built mobile microrobots with varying degrees of autonomy over the last fifteen years and a separate body of literature exists for larger scale jumping robots. In addition, the autonomous jumping microrobots described here were originally inspired by jumping insects which biologists have been studying for decades. While the mechanisms evolved in jumping insects are by no means optimal for jumping robots, studying how nature accomplishes a task can provide new insight or inspiration in robot design.

### 1.2.1 Microrobots

The world of centimeter-sized robots was first introduced by Seiko-Epson in 1993, when the company sold the first cubic centimeter sized robot, Monsieur, to highlight its ultra small and ultra low power product technologies (Figure 1.2a) [19]. While there have been a number of sub-cm<sup>3</sup> robots since then, another notable robot was released by Sandia in 2001 [20]. This 0.25 in<sup>3</sup> robot was intended to carry chemical sensors, microphones, or even cameras and used a number of commercially available components (Figure 1.2c). The Micromechanical Flying Insect (MFI) is a 2.5 cm-sized robot designed at Berkeley to fly [21]. While not yet flying, the MFI uses folded carbon fiber linkages with piezoelectric actuators to generate lift forces of over 500  $\mu\text{N}$  for a single wing (Figure 1.2e).

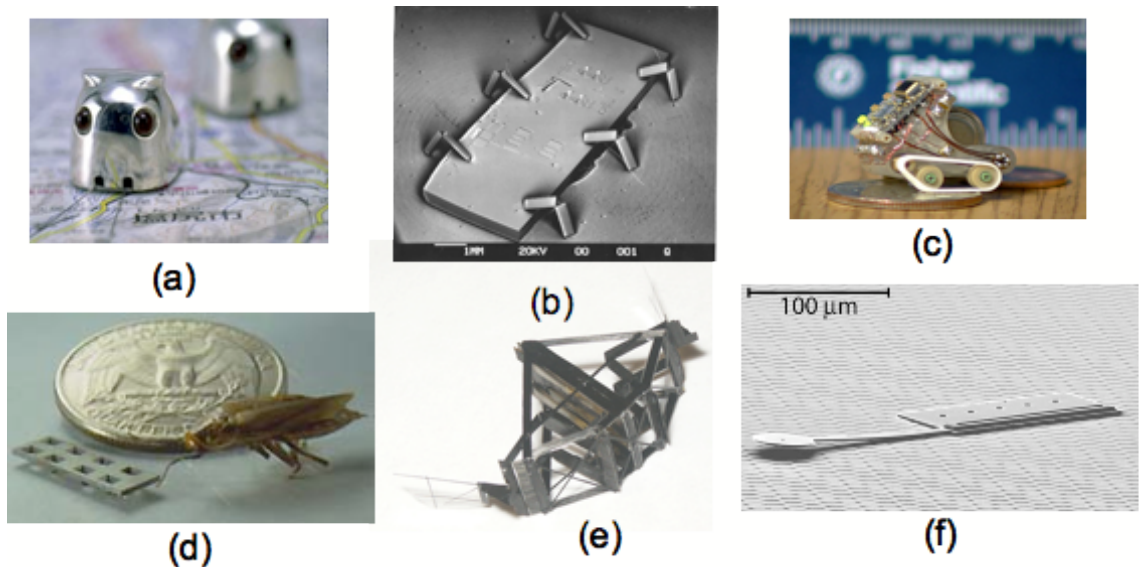


Figure 1.2: Previous Work in Microrobots. (a) The Seiko Monsieur Robot is approximately  $1 \text{ cm}^3$  and made from 98 separate pieces [19]. (b) Articulated legs designed to work with low-power electrostatic motors for a walking microrobot in [22]. (c) Sandia's  $0.25 \text{ in}^3$  answer to Monsieur [20]. (d) A thermally powered  $15 \times 5 \text{ mm}^2$  microrobot which can lift 30 times its own mass [23]. (e) The micromechanical flying insect (MFI) [21]. (f) Donald's  $60 \mu\text{m} \times 250 \mu\text{m}$  cantilever robot [24].

Moving down in size to sub-centimeter length scales, many early microrobots scavenged power from external sources such as vibrating, magnetic or electric fields [25, 26, 24]. The smallest of these is a simple  $60 \mu\text{m} \times 250 \mu\text{m} \times 10 \mu\text{m}$  silicon cantilever (Figure 1.2f) which is actuated and controlled by providing a control signal through the surface which the robot moves on. While the moving piece is small, power and control are integrated into the surface and it is therefore not autonomous by the definition used in this dissertation.

Other microrobots used tethers to supply power. Ebefors demonstrated a  $15 \times 5 \text{ mm}^2$  walking robot which could carry 30 times its own weight (Figure 1.2d), but its power-hungry thermal actuators required attached wires to provide power [23]. Mohebbi used a similar leg design on a cilia robot, but this design also required a tethered power

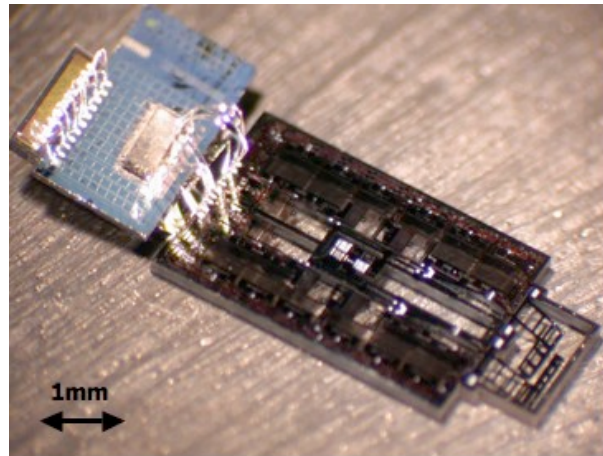


Figure 1.3: A 10 mg Solar-Powered Microrobot. This robot uses two 1-DOF legs to drag itself forward [28].

supply [27]. In a step towards power autonomy, Yeh designed and fabricated low power electrostatic motors and mechanisms (Figure 1.2b) appropriate for a millimeter-sized silicon robot although these were never integrated into a fully functioning microrobot [22].

In 2003, Hollar designed and fabricated the first autonomous microrobot – a 10 mg, solar-powered microrobot which also included an on-board controller [28]. While it can be argued that solar cells are not truly a self-contained power supply, when outdoors or in bright light, the microrobot is not limited to a particular terrain and does not require artificially generated fields for power. The robot (Figure 1.3) was designed with two 1-DOF legs to drag the microrobot forward. While it did not ultimately demonstrate forward motion due to force limitations in its motors, this robot did demonstrate autonomous “pushups” and some non-intended shuffling due to foot slippage.

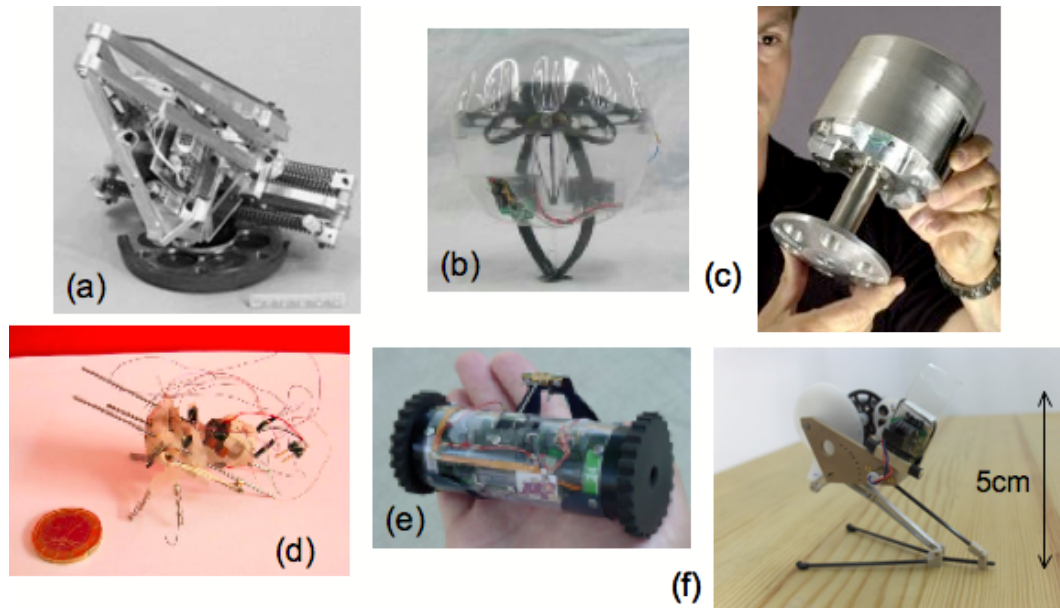


Figure 1.4: Previous Work in Jumping Robots. (a) Burdick’s jumper weighs 1.3 kg and can jump 2 m in distance [29]. (b) The MIT Microbot uses dielectric elastomer actuators to jump almost 4 times its own height [30]. (c) Sandia’s combustion driven piston can jump for almost 5 miles on a 20 g tank of gas [31]. (d) Grillo is only 15 g and uses passive forelegs to absorb impact energy [32]. (e) The University of Minnesota Scout robot uses a winch and leaf spring in conjunction with normal wheels to get around [33]. (f) EPFL’s unpublished 7 g jumping robot that jumps 1.4 m (27x the robot’s body length) [34].

### 1.2.2 Jumping Robots

Researchers have built a number of jumping robots for tasks ranging from climbing stairs to celestial exploration (Figure 1.4). These robots are ballistic jumpers which jump, pause to reset after landing, and jump again. Ballistic jumpers are different from hopping robots which jump continuously by reusing energy stored while landing. Hopping robots have been heavily studied due to the interesting control problems they pose but there are surprisingly few jumping robots in the literature. While it would certainly be interesting and beneficial for microrobots to store some energy upon landing for the next jump, that will not be discussed in this dissertation.

One of the earliest jumping robots was designed by Burdick and Fiorini for exploration on Mars [29]. This 1.3 kg robot was built using a spring for energy storage and a clever design requiring only a single motor to store energy in the spring as well as right and orient the robot after landing (Figure 1.4a). Another interesting feature was a 6-bar mechanism combined with a simple linear spring in order to change the force profile of the spring for greater efficiency in energy release. Demonstrations showed the robot jumping approximately 1 m high and 2 m in distance. The Grillo robot shown in Figure 1.4d is much smaller at 15 g and uses passive forelegs in order to dissipate energy upon impact and potentially store energy for the next jump, although this has not yet been demonstrated in action [32]. A similarly sized 7 g robot from EPFL (Figure 1.4f) has been demonstrated jumping 1.4 m high, but has not yet been published [34]. The primary purpose of this jumping robot is to launch Kovac's gliding robot in [35]. Finally, another jumping robot intended for planetary exploration is the MIT Microbot [30] in Figure 1.4b. This robot measures 10 cm across, weighs 100 g, and its spherical shape also allows it to roll after a jump to increase travel distance. The Microbot has been shown to jump approximately 40 cm straight up and uses a dielectric elastomer actuator (DEA) which combines the energy storage system with the actuator in one component. DEAs have also been used for SRI's jumping robots in [36].

In addition to robots designed to jump as a primary mode of locomotion, jumping capabilities have been added to other robots to improve their mobility when encountering obstacles. The 200 g Scout robots from the University of Minnesota (Figure 1.4e) use a motor to bend a leaf spring which is then released to jump up stairs [33]. Case Western's

Mini Whegs robots use a similar jumping mechanism to jump over small obstacles or up stairs as well [37].

Table 1.1: Comparison of Jumping Robots with Proposed Microrobot.

	Burdick [29]	Scout [33]	Proposed Microrobot
Mass (g)	1300	200	0.01
Length (mm)	150	110	6
Time between Jumps (sec)	30	63	20
Takeoff Velocity (m/s)	13.9	15.8	1.4
Takeoff Angle	50°	60°	45°
Jump Height (cm)	90	30	4.7
Average Energy in Jump (J)	125	25	0.00001

Finally, some jumping robots have departed from the more traditional designs of using a motor to store energy in a simple spring. Using shape memory alloy (SMA) spokes to deform an elastic exoskeleton, Sugiyama and Hirai have demonstrated a 40 mm diameter soft-bodied robot which jumps to heights of 300 mm by deforming its own skeleton [38]. Researchers at Sandia National Labs have demonstrated an explosive jumping robot pictured in Figure 1.4c [31]. Using a combustion driven piston, these robots have been demonstrated to jump over 9 m high. Typically a tank of gas can propel the robot for approximately 4000 jumps or up to 5 miles.

### 1.2.3 Biology

While the autonomous jumping microrobots in this dissertation are not intended to mimic biology, their design does draw inspiration from the natural world. Biologists have studied small jumping insects that provide much of the functionality required for the scenarios listed in Section 1.1 for the last several decades. Jumping animals range in

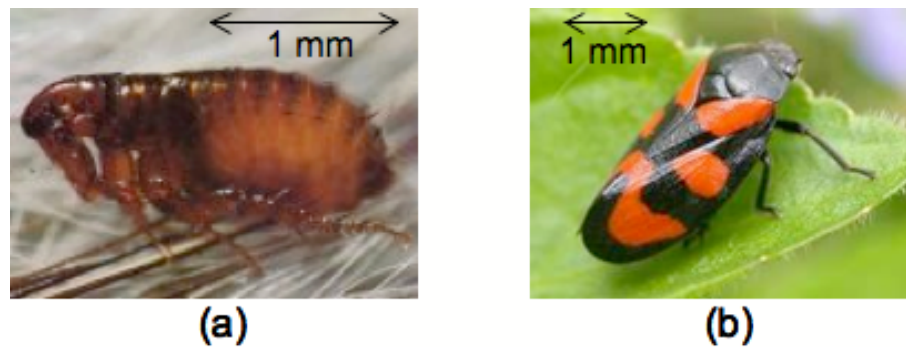


Figure 1.5: Oriental Rat Flea and Froghopper. Jumping insects provided the initial inspiration for this work and two of the jumping champions are the flea (a) and the froghopper (b).

size from several meters in length to sub-millimeters, although jumping mechanisms vary considerably through these length scales [39]. Two of the more interesting insects due to their small size and significant jumping abilities are fleas and froghoppers (Figure 1.5).

Fleas jump for a variety of reasons including latching on to a passing host, as well as an escape mechanism from anything resembling danger. Despite the commonplace nature of fleas, as of 40 years ago their jump was still not well understood. Their muscles simply could not provide the accelerations and powers observed during jumps. The flea's jump was first seriously studied by Bennet-Clark and Rothschild [40, 41]. A variety of flea types were used in the study, but some of the most well known work was done with the oriental rat flea *Xenopsylla cheopis*. *Xenopsylla* measures 1-2 mm in length, 0.21 mg when unfed, and can jump to a height of 90 mm – 50-100 times its own body length. These insects use approximately 180 nJ of energy for each jump translating to output power densities on the order of 1 W/g.

Using high speed cameras to capture the flea's jump on film, Rothschild and

Bennet-Clark demonstrated that the jump acceleration was too high to be caused by a single muscle contraction, but must instead be a product of the muscle combined with an elastic protein called resilin. Resilin is a rubber-like material which stores energy and can then release it quickly and efficiently for a jump. Fleas use their muscles to compress the resilin and therefore store energy. Releasing this stored energy quickly and efficiently like a catapult allows the fleas to achieve their phenomenal accelerations and jump heights.

While the flea is an excellent jumper, the reigning champion of the jumping insect world is the froghopper insect or spittlebug *Philaenus spumarius*. Burrows first examined the froghopper jump using high-speed photography techniques in 2003 [42]. *Philaenus* has an average length of 6.1 mm, mass of 12.3 mg, and the champion jumpers can reach heights over 700 mm – over 100 times their body length. For an average jump, the froghopper requires 49  $\mu\text{J}$  of kinetic energy released in approximately 1 ms for an incredible 36 W/g output power density. Table 1.2 compares the flea and froghopper properties to the proposed jumping microrobot.

Table 1.2: Comparison of Jumping Insects with Proposed Microrobot.

	Flea [41]	Froghopper [42, 43]	Proposed Microrobot
Mass (mg)	0.21	12.3	10
Length (mm)	1-2	6.1	6
Time between Jumps (sec)	3.5	3	20
Takeoff Velocity (m/s)	1.3	2.8	1.4
Jump Height (cm)	9	42.8	4.7
Average Energy in Jump ( $\mu\text{J}$ )	0.18	49	10
Average Power Output (W/g)	0.86	36	1

Despite the vast resources from previous work studying jumping mechanisms in biology, building larger-scale versions of these jumping mechanisms for robots, and design-

ing tiny components for microrobots, there are still a number of challenges for designing a millimeter-scale autonomous robot which can move quickly and efficiently through its environment. As seen in small insects, jumping is a particularly attractive means of moving large distances and overcoming obstacles in relatively short periods of time. However, a jumping robot requires a micromechanical energy storage system for fast accelerations and high work density actuators to store energy for a jump. The energetics of jumping microrobots in addition to the component design challenges will be addressed in [Chapter 2](#).

## Chapter 2

# Robot Locomotion and Design

The ultimate goal of this work is to create an autonomous jumping microrobot that can move around in unstructured environments. This robot will be several millimeters in length and width and be able to jump many centimeters several times per minute. While the jumping gait was initially inspired by biology, this chapter will describe the challenges that result from scaling a jumping robot to millimeters in size, as well as a detailed analysis of jumping in comparison to other locomotion methods. In addition, this chapter presents the basic requirements for each robot component based on the locomotion analysis. The robot components have been divided into four primary challenges: energy storage, actuation, power, and control. Due to the size scale of this robot, none of these items are readily available off-the-shelf and each will need to be designed and fabricated separately.

Before tackling the challenges of designing a jumping microrobot, it is important to understand the characteristics of a jump. Looking back to introductory projectile physics, the jump trajectory is determined by the initial kinetic energy provided to the jumper at

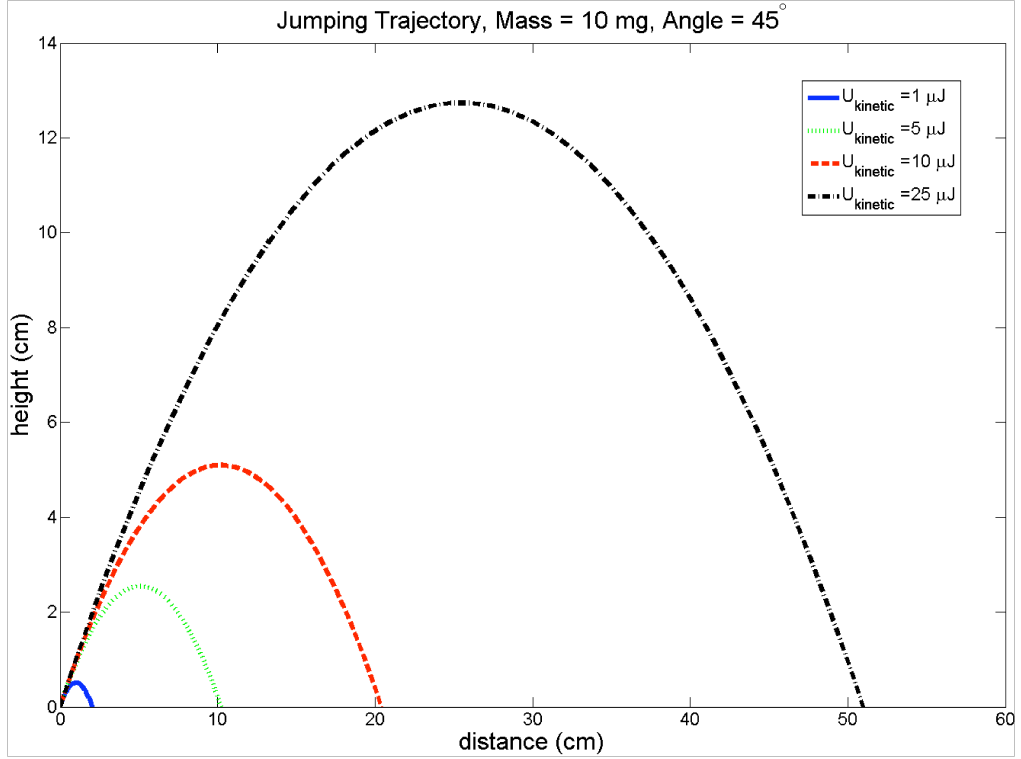


Figure 2.1: Jumping Trajectories with Different Initial Kinetic Energies. The trajectories shown are given for a take-off angle of  $45^\circ$  and robot mass of 10 mg.

take-off. To examine the initial kinetic energies required to produce centimeter-sized jumps, a simple model describing the robot as a point mass is used to plot jumps in Figure 2.1.

$$y(t) = -\frac{1}{2}gt^2 + (v \sin \theta) t + y_0 \quad (2.1)$$

$$x(t) = (v \cos \theta) t + x_0 \quad (2.2)$$

where  $g$  is gravity,  $\theta$  is the take-off angle,  $x_0$  and  $y_0$  define the initial position of the robot, and  $v$  is the initial velocity derived from the kinetic energy ( $U_{kinetic}$ ) given to the robot of mass  $m_{robot}$ .

$$v = \sqrt{\frac{2U_{kinetic}}{m_{robot}}} \quad (2.3)$$

Given a specified kinetic energy at the jump take-off, the final height and distance

(without drag which is considered in Section 2.1) are calculated from the above model.

$$d = \frac{2U_{kinetic}}{mg} \sin 2\theta = \frac{v^2}{g} \sin 2\theta \quad (2.4)$$

$$h = \frac{U_{kinetic}}{mg} (\sin \theta)^2 = \frac{v^2}{2g} (\sin \theta)^2 \quad (2.5)$$

Several facts become apparent from the jump defined by equations (2.4) and (2.5).

The take-off angle,  $\theta$  will have a significant impact on maximizing the height versus distance jumped. Height is maximized if  $\theta$  is  $90^\circ$  and distance is maximized when  $\theta$  is  $45^\circ$ . The second important point is that both height and distance increase as the ratio of kinetic energy to mass increases. Therefore, if attempting to maximize jump height or distance, it is important to minimize mass and/or increase the initial kinetic energy. Minimizing mass will be highly dependent on both the size of the robot and the material used, both of which are fabrication-dependent. Increasing the initial kinetic energy will also increase take-off velocity and accelerations. As the size of the jumping robot decreases, this take-off velocity will greatly affect drag forces experienced by the robot which can decrease performance as discussed in Section 2.1.

## 2.1 Scaling

As a jumping robot decreases in size, many challenges arise due to shorter dimensions and correspondingly smaller mass. Significantly larger surface area to mass ratios make drag forces significant at this scale, and short legs result in high power requirements and high accelerations. In addition, as the robot dimensions grow smaller, the obstacles around the robot grow correspondingly larger and the environment presents itself as significantly more rugged than it might appear to a larger robot as will be discussed in Section

2.2.1. Finally, energy efficiency becomes a significant problem. This dissertation discusses an ‘autonomous’ robot implying that the robot carries its own power supply. With a limited amount of energy available, it is important that the chosen gait remain relatively efficient (Section 2.2.2).

### 2.1.1 Drag

While fluidic drag forces may only seem important for flying or swimming robots, jumping microrobots also experience fluidic drag when traveling through the air. Two substantial drag forces are viscous drag and pressure drag. An important means of determining the dominance of each of these drag forces is the nondimensional Reynolds number, where  $\rho$  is the fluid density,  $v$  is the velocity,  $L$  is a characteristic length, and  $\mu$  is the fluid viscosity.

$$Re = \frac{\rho v L}{\mu} \quad (2.6)$$

The Reynolds number is the ratio of inertial forces to viscous forces. If this ratio is smaller than 1, viscous or frictional drag forces are especially dominant. Solem discusses microrobots with Reynolds numbers less than 1 in [44]. For jumping microrobots with take-off velocities on the order of 1.5 m/s and a characteristic length of approximately 5 mm, the Reynolds number in air is approximately 500. While viscous drag forces will still have some effect on the robot’s motion, pressure drag will be the dominant drag force for these microrobots.

While drag may not be critical for larger jumping robots, it is important to look at the dependence of this force on characteristic length (Figure 2.2). As the jumping robot decreases in size, the ratio of its surface area to volume increases. Surface area is

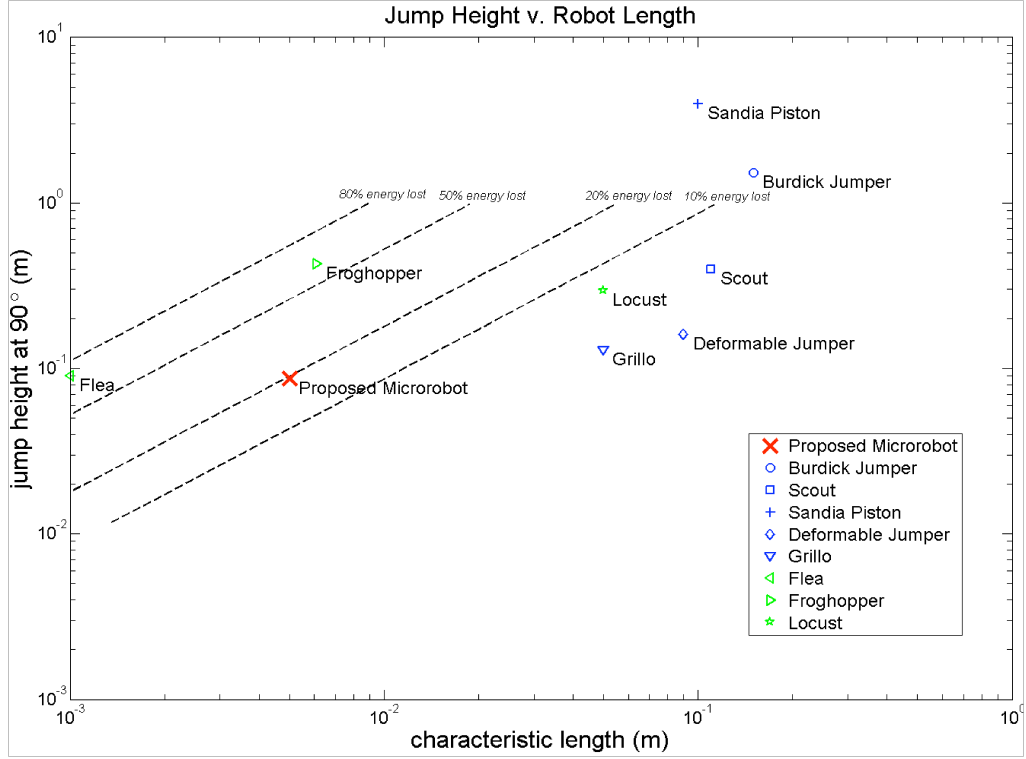


Figure 2.2: Height v. Length for Various Robots and Insects Demonstrating Drag Losses. Drag forces are dependent on the microrobot’s characteristic length and initial takeoff velocity. As the robot grows in size, drag forces are less important, but a robot the size of a flea can lose as much as 80% of its initial energy to drag.

proportional to  $l^2$  while mass is proportional to  $l^3$ . Drag force is described in Equation 2.7 where  $C_D$  is the drag coefficient,  $\rho$  is the density of the fluid through which the robot is jumping, and  $A$  is related to the robot’s cross-sectional surface area in the direction of motion.

$$F_{drag} = \frac{C_D \rho A v^2}{2} = C_D \rho U_{kinetic} \frac{A}{m} \propto \frac{1}{l} \quad (2.7)$$

In general, the drag force will increase as the length scale decreases. Another important part of this equation is the drag coefficient. The drag coefficient is primarily related to the shape and texture of the robot. Bennet-Clark investigated the effect of drag

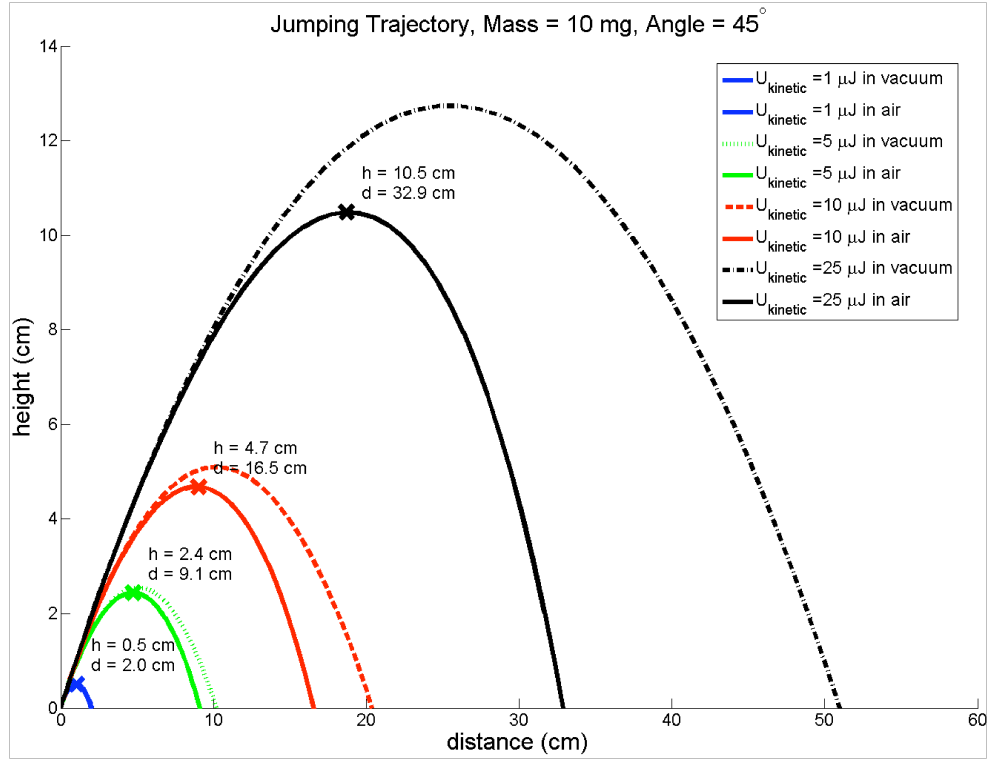


Figure 2.3: Jumping Trajectories with Different Initial Kinetic Energies and Drag. The trajectories shown are given for a take-off angle of  $45^\circ$ , robot mass of 10 mg,  $C_D$  of 1.5,  $A$  of  $20 \text{ mm}^2$ , and air density of  $1.2 \text{ kg/m}^3$ .

on jumping insects in varying states of wholeness by catapulting them into both air and vacuum to calculate the drag coefficients [45]. In general, these insects had drag coefficients of approximately 0.8 - 1.5 where the upper end of the spectrum included winged flies that still had their legs and wings attached while the lower end included the same flies with legs and wings removed. To remain conservative in this analysis, a drag coefficient of 1.5 was chosen to model the microrobot in this work.

Including drag, the equations of motion solved in Equations 2.1 can be modified

as follows.

$$m \frac{dy^2}{dt^2} + \frac{C_D \rho A_y}{2} \left( \frac{dy}{dt} \right)^2 + mg = 0 \quad (2.8)$$

$$m \frac{dx^2}{dt^2} + \frac{C_D \rho A_x}{2} \left( \frac{dx}{dt} \right)^2 = 0 \quad (2.9)$$

These equations are solved to give the following positions given the initial velocity in the x and y direction,  $v_{ix}$  and  $v_{iy}$  respectively.

$$y(t) = \frac{2m}{C_D A \rho} \ln \left[ \cos \left( \sqrt{\frac{C_D A \rho g}{2m}} t \right) + \sqrt{\frac{C_D A \rho}{2mg}} v_{iy} \sin \left( \sqrt{\frac{C_D A \rho g}{2m}} t \right) \right] + y_0 \quad (2.10)$$

$$x(t) = \frac{2m}{C_D A \rho} \ln \left( 1 + \frac{C_D A \rho}{2m} v_{ix} t \right) + x_0 \quad (2.11)$$

The final height and distance including drag in air, may then be calculated.

$$h_{air} = \frac{m}{C_D A \rho} \ln \left( 1 + \frac{C_D A \rho}{2mg} v_{iy}^2 \right) + y_0 \quad (2.12)$$

$$d_{air} = \frac{2m}{C_D A \rho} \ln \left[ 1 + 2 \sqrt{\frac{C_D A \rho}{2mg}} v_{ix} \arctan \left( \sqrt{\frac{C_D A \rho}{2mg}} v_{iy} \right) \right] + x_0 \quad (2.13)$$

As seen in Figure 2.3, drag substantially effects the height and distance traveled by the robot. For a more quantitative view, Table 2.1 lists the height and distance jumped in air versus the height and distance jumped in vacuum for different takeoff energies. At lower initial kinetic energies and take-off velocities, the trajectory is not altered substantially while the effect is significantly more noticeable at higher energies.

Especially noticeable at higher take-off velocities is the effect on distance. Due to drag, the robot's trajectory in air is no longer parabolic and the horizontal velocity decreases throughout the jump. From both Figure 2.3 and Table 2.1 it is obvious that the robot can be significantly more efficient if it takes many small jumps instead of larger jumps.

Table 2.1: Comparison of Jumps in Vacuum and Air.

$U_{kinetic,i}$ ( $\mu\text{J}$ )	Takeoff Velocity (m/s)	Height/Distance in Vacuum (cm)	Height/Distance in Air (cm)	Height/Distance Efficiency
1	0.45	0.51/2.0	0.50/2.0	0.99/0.98
5	1.0	2.5/10.2	2.4/9.2	0.96/0.90
10	1.4	5.1/20.4	4.7/16.6	0.92/0.81
25	2.2	12.7/51.0	10.5/33.1	0.82/0.65

Table 2.2: Comparison of Kinetic Energy at Take-off and Landing.

$U_{kinetic,i}(\mu\text{J})$	$U_{kinetic,i}(\mu\text{J})$	% Energy dissipated (takeoff angle = $45^\circ$ )
1	0.97	3.5
5	4.3	14
10	7.8	22
25	16	35

In addition, due to the decreasing horizontal velocity, the robot loses some of its energy to drag and will therefore need to dissipate less energy on landing than it might otherwise. By the same reasoning, less energy is dissipated as the takeoff angle increases and the jump becomes more vertical. While microrobot landing is not discussed in this work, it will be a critical component of future work and a comparison of kinetic energies at take-off and landing is given in Table 2.2.

Drag has another effect on the design of the robot in addition to dissipating energy on landing and reducing the overall height and distance reached in the robot's trajectory. Due to drag, the jumping microrobots have an optimal mass dependent on their take-off energy,  $U_{kinetic}$ . If the robot is quite massive, the take-off velocity is lower which will reduce the overall jump height. If the robot is very light, drag plays an increasing role. Therefore, as seen in Figure 2.4, an optimal mass exists for the robot. Given the range of energies

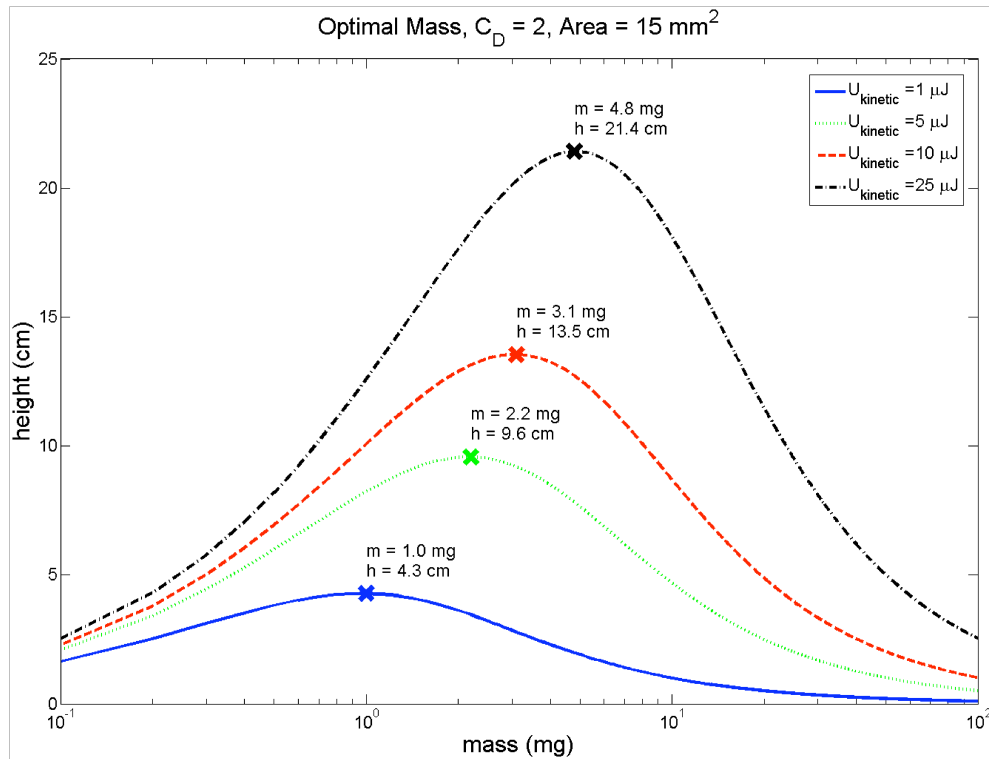


Figure 2.4: Optimal Mass. Given a fixed drag coefficient  $C_D$  and area  $A$ , the jump height is plotted when the 10 mg robot takes off at  $90^\circ$ . At low masses, the robots have difficulty overcoming drag, while at higher masses the robots have low takeoff velocities.

available to the jumping microrobot in this dissertation, the optimal mass is on the order of milligrams. If the drag coefficient and/or surface area are reduced, this optimal mass is even lower due to the smaller effect of drag. Regardless, if the engineering allows, it is still beneficial to make the robot lighter than the 10 mg target used to generate Figure 2.3.

In addition, drag implies that the optimal take-off angle to maximize distance is not  $45^\circ$  as seen in Equation 2.4. Intuitively, this is due to the fact that the trajectory is no longer parabolic. As seen in Figure 2.3, the descent is steeper than the ascent due to the decreasing forward velocity. Lowering the takeoff angle allows the microrobot to spend more time travelling forward when its velocity is highest. The optimal takeoff angle decreases as

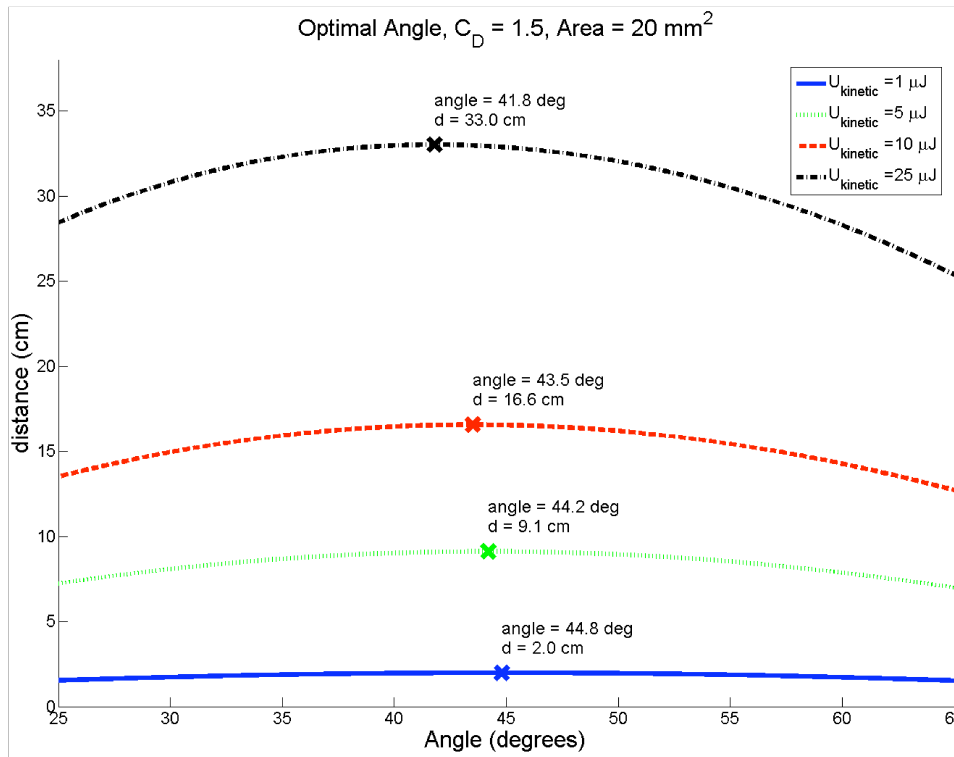


Figure 2.5: Optimal Angle. Given a fixed drag coefficient  $C_D$ , mass, and area, the jump distance is plotted when the 10 mg robot takes off at various angles. As the effect of drag increases, distance will be maximized at angles less than  $45^\circ$ .

the effect from drag increases (Figure 2.5).

### 2.1.2 Power and Acceleration

In addition to drag, there are other consequences to shrinking a jumping robot to millimeter size scales. The jumping robot model in Figure 2.6 simplifies the jumping robot to a point mass  $m_{\text{robot}}$  attached to a spring leg with stiffness  $k_{\text{leg}}$ . The robot is taking off from a surface assumed to be significantly stiffer than the robot leg.

Assuming for now that the spring is linear, the trajectory of the robot jumping

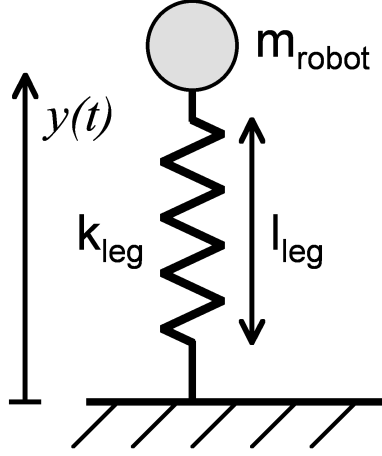


Figure 2.6: Jumping Robot Model. The jumping robot is simplified to a point mass  $m_{robot}$  attached to a linear spring-loaded leg of stiffness  $k_{leg}$ . The spring is compressed a distance  $l_{leg}$  before takeoff and this length is assumed to be characteristic of the length of the robot.

vertically ( $\theta = 90^\circ$ ) before the leg leaves the ground can be described as follows.

$$y(t) = l_0 (1 - \cos \omega t) \quad (2.14)$$

where  $l_0$  is the leg length adjusted by gravity ( $l_{leg} - m_{robot}g/k_{leg}$ ) and  $\omega$  is the resonant frequency of the robot  $\sqrt{k_{leg}/m_{robot}}$ . Taking the derivative of this position gives the velocity of the robot over time and the second derivative shows the accelerations experienced by the robot.

$$\dot{y}(t) = l_0 \omega \sin \omega t \quad (2.15)$$

$$\ddot{y}(t) = l_0 \omega^2 \cos \omega t \quad (2.16)$$

If the robot takes off from the ground when the leg is fully extended and all of the energy has been released from the spring, the takeoff time  $t_{takeoff}$  is derived from  $y(t_{takeoff}) = l_0$  as

$$t_{takeoff} = \frac{\pi}{2\omega} \quad (2.17)$$

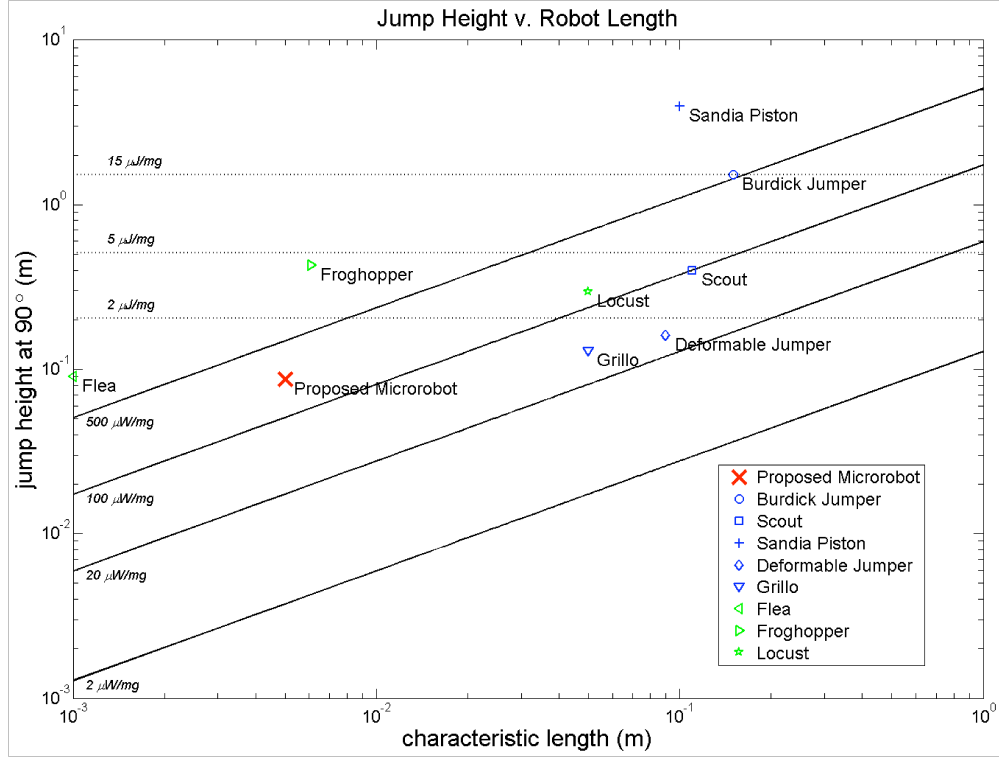


Figure 2.7: Height v. Length for Various Robots and Insects Demonstrating High Powers Required. Insects like fleas and froghoppers produce high power densities over  $500 \mu\text{W}/\text{mg}$  to reach 10s of cm heights. A practical upper limit for direct power from muscles is  $100 \mu\text{W}/\text{mg}$  [39].

This section primarily pertains to how accelerations scale as the length scale of the robot changes (Figure 2.7). It has already been shown that  $m_{robot}$  scales as  $l^3$ , but leg stiffness  $k_{leg}$  and resonant frequency  $\omega$  are a little less intuitive. Intuition says that as the robot gets bigger, the leg stiffness will increase because the leg needs to support the weight of the robot. In theory, if all robots are given the same energy density, they should be able to jump to the same height (Equation 2.5) neglecting drag. Assuming height is invariant to length scale,

$$h = \frac{v(t_{takeoff})^2}{2g} = \frac{l_0^2 k_{leg}}{2gm} \propto \frac{l^2 k_{leg}}{l^3} \quad (2.18)$$

While the assumption that energy density is constant across length scale is not entirely true, it is a close enough approximation to show that  $k_{leg} \propto l$ . Therefore, it can also be shown that  $\omega \propto 1/l$ . Given these approximations, Table 2.3 shows the scale dependence of takeoff time, takeoff velocity, acceleration, force density, and power density.

Table 2.3: Scale Dependence of Takeoff Variables.

	scale
takeoff time	$l$
velocity	1
acceleration	$1/l$
force density	$1/l$
power density	$1/l$

The first point of interest from Table 2.3 is the takeoff time  $t_{takeoff}$ . Intuitively, it makes sense that as the leg lengths shrink, the time before reaching takeoff velocity also becomes shorter. A shorter takeoff time also implies greater accelerations experienced by the robot. For a 10 mg robot with  $k_{leg} = 0.8$  mN/mm, the robot's vertical position and acceleration are plotted in Figure 2.8. A jumping microrobot with these characteristics accelerates to a takeoff velocity of 1.38 m/s in 5.6 msec and experiences an acceleration of  $40g$ !

While these accelerations are small compared to nature's flea or frog hopper which experience several hundred  $g$ , it is important to consider the robot's ability to withstand these accelerations. Large accelerations imply that the robot needs to both generate and withstand high forces. Fabrication will need to take into account stresses on the robot body and the actuators will need to generate the high force densities required for these accelerations. In fact, many insects use folding legs to increase their leg length and therefore

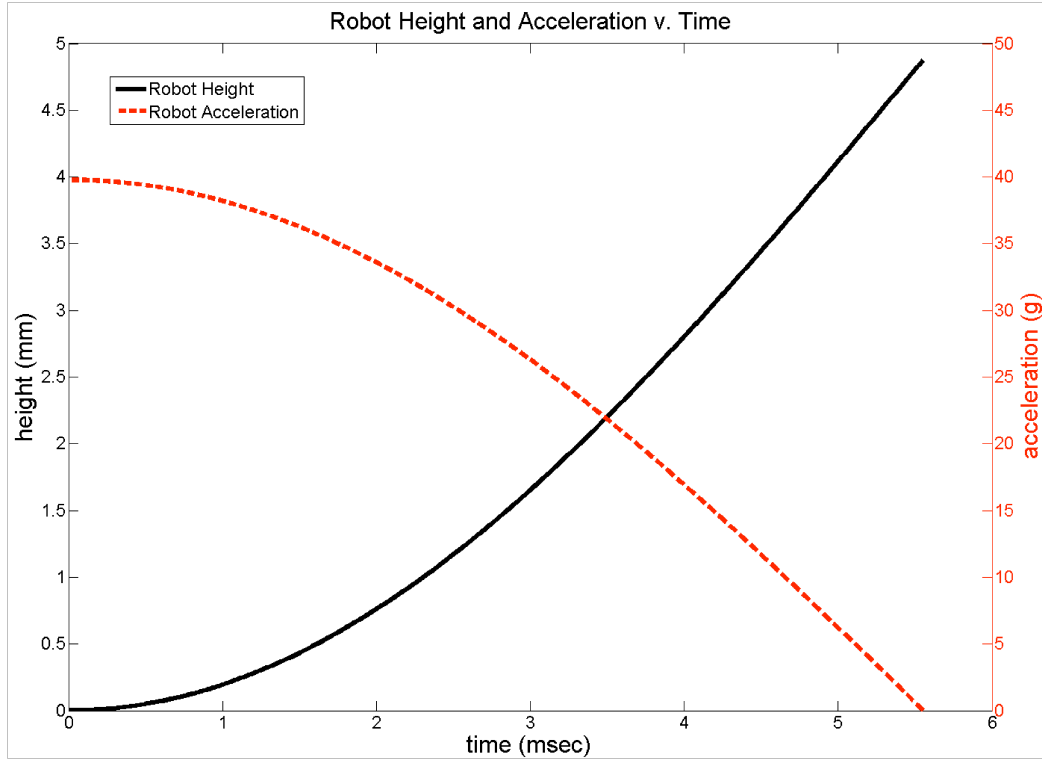


Figure 2.8: Jumping Robot Model Position and Acceleration. The position and acceleration of the jumping robot model in Figure 2.6 is plotted versus time.  $m_{robot} = 10mg$ ,  $k_{leg} = 0.8mN/mm$ ,  $l_{leg} = 5mm$

lower these forces and accelerations [39].

In addition, the power density required by the motors increases as the robot scales down in size. The energy available for the robot's jump needs to be released in milliseconds for millimeter-scale robots. The power delivered by the robot is derived below.

$$P(t) = F(t)v = \frac{1}{2}k_{leg}l_0^2\omega \sin 2\omega t \quad (2.19)$$

The power generated by the robot during takeoff is plotted in Figure 2.9. While 2.7 mW may not appear to be a large amount of power at first, this is equivalent to 270  $\mu W/mg$  for a 10 mg robot. Power density is related to the robot length in Figure 2.7. Two of

the diagonal lines in in Figure 2.7 represent muscle at  $100 \mu \text{ W/mg}$  [39] and electrostatic inchworm actuators power at  $1.7 \mu \text{ W/mg}$  [46]. A similar discovery in power discrepancy for small jumping insects early on led scientists to discover that these insects use a catapult mechanism to increase power output [40]. By storing energy first and releasing it quickly, these insects could overcome the power limitations of their muscles and jumping microrobots will require a similar energy storage component.

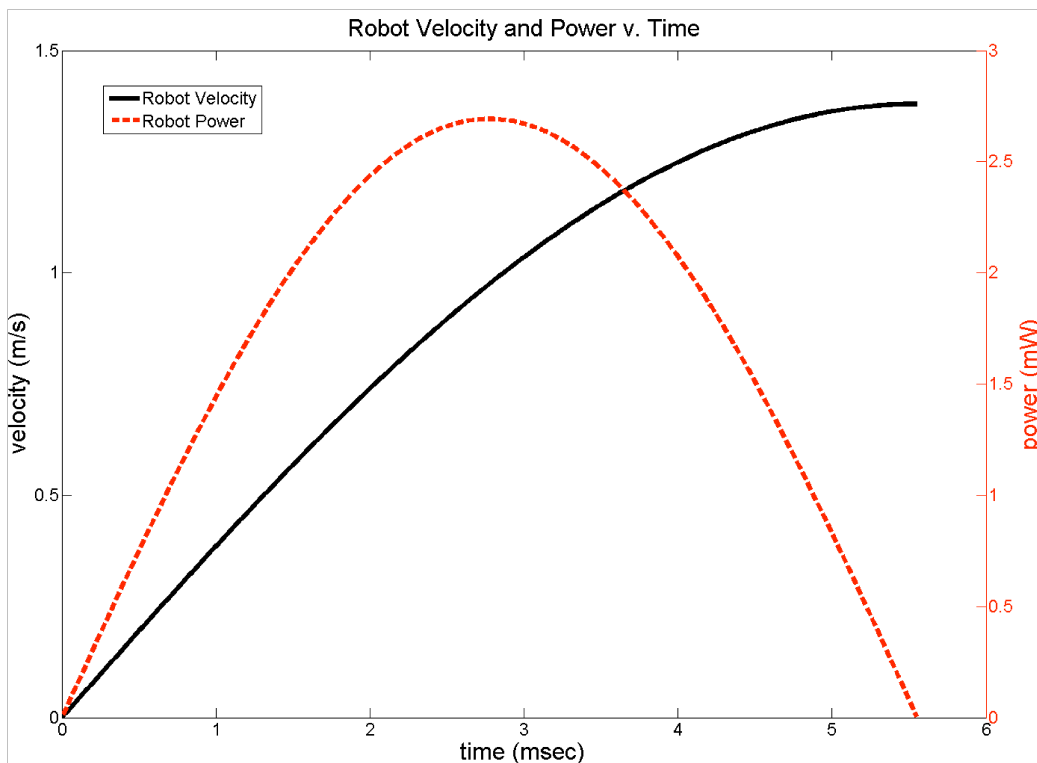


Figure 2.9: Jumping Robot Model Velocity and Power. The velocity and power of the jumping robot model in Figure 2.6 is plotted versus time.  $m_{robot} = 10mg$ ,  $k_{leg} = 2N/m$ ,  $l_{leg} = 5mm$

## 2.2 Jumping Locomotion

Despite the challenges in scaling a jumping robot down to millimeter sizes, jumping offers potentially beneficial trade-offs that alternative locomotion schemes cannot. As the robot decreases in size, a number of challenges arise for moving around in an unstructured environment. For example, as the robot dimensions grow smaller, the obstacles around the robot grow correspondingly larger and the environment presents itself as significantly more rugged than it might appear to a larger robot. Energy efficiency also becomes a significant problem since the robot will be carrying its own power supply. With a limited amount of energy available, it is important that the chosen gait remain relatively efficient.

### 2.2.1 Obstacle Avoidance

Now that the jump has been defined, Figures 2.1 and 2.3 display one of the biggest advantages of jumping for locomotion. The robot can simply jump over reasonably-sized obstacles. As the robot shrinks in size, objects and obstacles around the robot grow proportionally larger from the robot's perspective. The surface becomes increasingly less planar and more rugged. Even at larger size scales, programming robots to understand and move around obstacles autonomously has always been difficult, and jumping provides an interesting mechanical solution to a difficult artificial intelligence problem.

Legged, walking robots can generally overcome obstacles sized similarly to its legs although this may be improved with leg articulation, number of legs, and number of body segments. In addition, wheeled robots are generally limited to overcoming obstacle sizes equivalent to half of the wheel diameter. In fact, the Scout and Mini Whegs robots described

previously in Section 1.2.2 use jumping as an extra means of locomotion to overcome the obstacle avoidance deficiencies of legged and wheeled locomotion [33, 37]. Jumping provides a similar functionality for microrobots as seen in Table 2.4.

Table 2.4: Comparison of Microrobots Overcoming Obstacles.

	Hollar [28]	Ebefors [23]	Donald [24]	Proposed Microrobot
Mass (mg)	10	80	0.0003	10
Leg Length (mm)	1	1	0.1	6
Obstacle Height ( $\mu m$ )	$\sim 10$	$\sim 100$	$\sim 1$	10000
Common Object	ragweed pollen	hair	E. coli bac- teria	lego brick

Even if they had been able to walk autonomously, the walking microrobots designed and built by Hollar and Ebefors would only be able to overcome obstacles the size of a human hair or smaller [28, 23]. In addition to requiring a special surface for power and control, the microrobot fabricated by Donald also requires that this surface be very clean as well [24]. While walking microrobots may use greater leg articulation or adhesive surfaces in the future to overcome some of these problems, the millimeter-sized legs of millimeter-sized robots will limit the terrain in which these robots can move. Jumping provides a relatively simple solution to this problem given enough energy.

### 2.2.2 Locomotion Efficiency

While jumping provides an excellent means for autonomous mobile microrobots to overcome obstacles, it is not immediately obvious that jumping is an energetically efficient means of transport. For many insects, jumping is an energetically costly means of escape from a predator and does not provide a more general means to move around. Maintaining

energy efficiency is extremely important when carrying power on-board the microrobot. This section will study some of the factors that determine locomotion efficiency.

It is difficult to compare locomotion or gaits in a generic way. Even two robots that use the same gait can vary dramatically based on implementation. For example, a passive walking robot designed at Michigan walks at 0.44 m/s, weighs 12.7 kg and consumes 10.9 W [47]. Honda's Asimo robot uses actuators at each joint, walks at the same speed, weighs 52 kg and consumes 768 W [47]. Two robots moving at the same speed and using roughly similar gaits consume vastly different amounts of energy over the same distance traveled.

A good measure for comparing locomotion efficiencies is the dimensionless cost of transport (COT), defined as the energy required to move a given weight over a given distance.

$$COT = \frac{U}{mgd} \quad (2.20)$$

$U$  is the work done by the robot or organism of mass  $m$  to move a distance  $d$  in gravity  $g$ . While  $U$  generally indicates the total energy input into the system, the analysis below will specify only the mechanical energy used by the robot and will ignore actuation and transmission efficiencies. A lower cost of transport indicates that a microrobot requires less energy to move the same distance. The sections below detail simple locomotion models for microrobots with which to compare locomotion efficiency. As mentioned above however, varying implementations can result in radically different energy costs. For reference, a walking human has a cost of transport of approximately 0.2 [47]. Assuming no resistance to motion and a rolling gait, the cost of transport approaches 0.

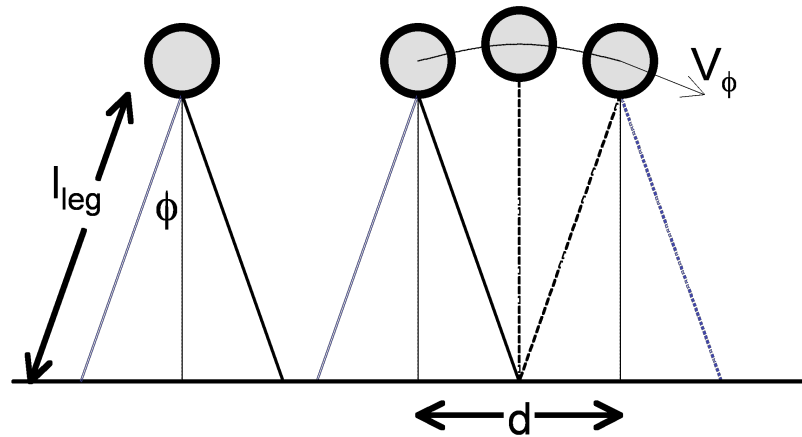


Figure 2.10: Simple Walking Microrobot Model. The simple walking model used to calculate cost of transport is a point mass,  $m$ , with rigid, mass-less legs of length  $l_{leg}$ . Both feet are on the ground only for a brief instant in which they span angle  $2\phi$ . The robot is moving forward at velocity  $v_f$ .

## Walking

A very simple model of a walking robot consists of a two-legged robot as a point mass with rigid, non-articulated, mass-less legs (Figure 2.10). – the same as the minimal walking model described by Alexander [48]. The robot body moves forward in arcs, and there is only one foot on the ground at a time except for a brief instance when weight shifts from one foot to the other. Some additional assumptions further reduce the energy required to walk. The model is not completely passive, and it is assumed that the robot is controlled or designed so that it stays balanced and horizontal forces cancel at the instant when both feet are on the ground. In addition, this model does not include any sources for internal work such as overcoming bearing friction or storing energy in flexures to move the robot legs.

Instead, the only work done in this walking model is when the feet push off the

ground. When one foot hits, the robot is traveling at velocity  $v_\phi$  tangent to the downward arc trajectory. This kinetic energy is dissipated in the foot strike. At the same time however, the other foot takes off at velocity  $v_\phi$  tangent to the upwards arc trajectory. This implies that the robot adds energy (or does work) equivalent to:

$$U_{walking} = \frac{1}{2}mv_\phi^2(\sin \phi)^2 \quad (2.21)$$

where  $2\phi$  is the angle between the legs when both feet are on the ground. The distance traveled during half a stride is proportional to the leg length,  $l_{leg}$ .

$$d_{walking} = 2l_{leg} \sin \phi \quad (2.22)$$

Therefore, the cost of transport can be calculated as

$$COT_{walking} = \frac{1}{4g} \frac{v_f^2}{l_{leg}} \frac{\sin \phi}{(\cos \phi)^2} \quad (2.23)$$

As can be seen in Equation 2.23, the cost of transport is proportional to the square of the forward velocity and inversely proportional to the leg length. As the leg length shrinks proportional to the robot size for a microrobot, more energy will be required to move for the same velocity. If maintaining velocity is not important however, and robot speed scales as leg length, the the cost of transport can in fact be smaller for walking microrobots than larger robots. A correctional factor of  $\sin \phi / (\cos \phi)^2$  implies that less energy is required if the legs sweep smaller angles. Minimizing  $\phi$  will result in practical implementation problems of balance and stride frequency however. For reference, a typical human has a  $\phi$  of  $25^\circ$  and the legs on the walking microrobot designed by Hollar have a  $\phi$  of  $15^\circ$ .

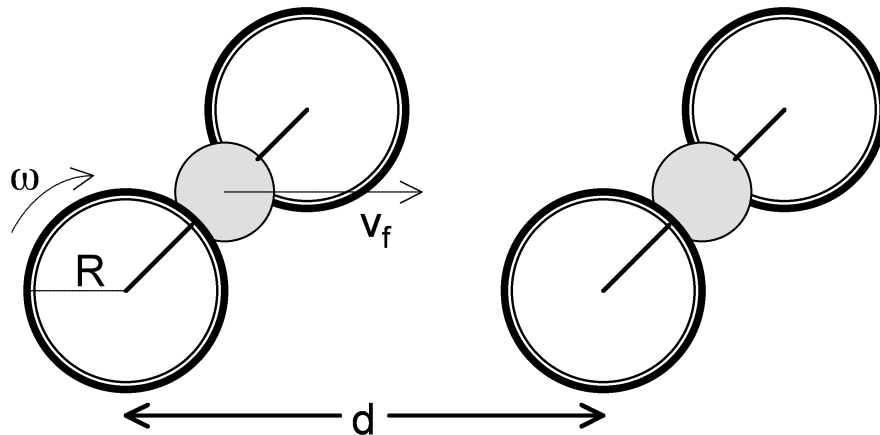


Figure 2.11: Simple Wheeled Microrobot Model. The simple wheeled microrobot model used to calculate cost of transport is a robot with mass,  $m_{robot}$  and two wheels with mass  $m_{wheel} \ll m_{robot}$  and radius  $R$ . The robot is moving forward at velocity  $v_f$ .

### Wheeled Driving

Wheels are common for larger robots, but not for microrobots. Wheeled microrobots encounter a great number of problems stemming from friction and surface adhesion. Surface forces scale as  $l^2$  while inertial forces scale as  $l^3$  giving surface forces more relevance for millimeter-sized microrobots. Surface forces are especially important in bearings that would be required for robots which roll; friction between the wheel and the ground would obviously need to be greater than the friction in the bearings. The simplest model for a wheeled robot would include frictionless bearings and wheels which do not slip and have no rolling resistance. In this model, the cost of transport would be 0 assuming the robot is already moving at speed  $v_f$ .

As a more practical approach for microrobots, wheeled robots can also be considered as direct-drive which do not require any bearings assuming that the actuator constrains the motion of the axle or wheel. In this model, the robot does not make use of momentum

which require free-spinning wheels. This very simple model shown in Figure 2.11 considers a wheeled robot of mass  $m_{robot}$  with two wheels of radius  $R$  and mass  $m_{wheel}$ . It is assumed that  $m_{robot} \gg 2m_{wheel}$ .

The work done by this wheeled microrobot is the work required to rotate the wheels and therefore move the robot mass forward. This work includes the kinetic energy given to the robot body as well as the rotational energy delivered to the wheels. Since free-spinning wheels are not considered in this model, the total energy delivered to the robot during each wheel revolution is:

$$U_{wheels} = \frac{1}{2}m_{robot}v_f^2 + I_{wheel}\omega^2 \quad (2.24)$$

where  $v_f$  is the velocity of the robot,  $I_{wheel}$  is the wheel moment of inertia, and  $\omega$  is the wheel's angular velocity. The distance traveled is simply given by the wheel circumference,  $2\pi R$ . Therefore, the cost of transport can be calculated as

$$COT_{wheels} = \frac{1}{4\pi g} \frac{v_f^2}{R} \quad (2.25)$$

The direct drive wheeled microrobot has a cost of transport similar in form to the walking microrobot. It also has a cost of transport proportional to the square of the forward velocity and inversely proportional to the wheel radius. As the wheel radius decreases and velocity stays the same, more energy will be required to move. If maintaining velocity is not important however, and robot speed scales as the wheel radius, the the cost of transport can in fact be smaller for wheeled microrobots than larger wheeled robots.

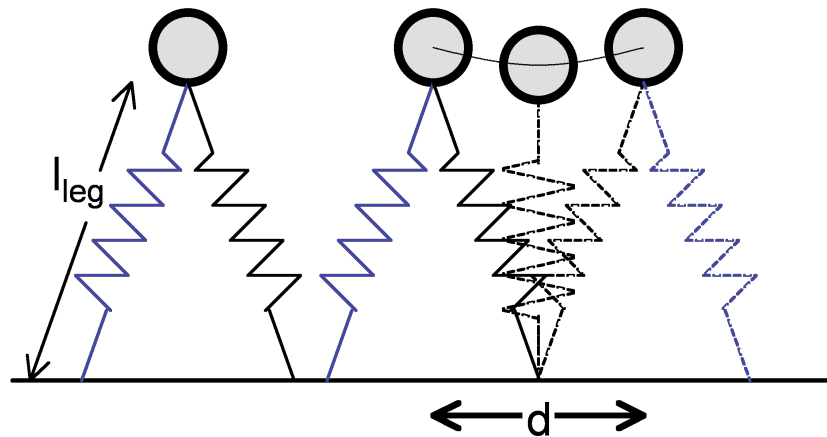


Figure 2.12: Simple Running Microrobot Model. This model includes a point mass,  $m$  and spring legs of negligible mass. In an ideal world, a running or hopping robot would have a cost of transport of 0.

## Running and Hopping

Running and hopping are both categorized by using energy storage elements to re-use energy that would otherwise be dissipated on impact. A common running model is shown in Figure 2.12. This model includes a point mass robot with spring legs of negligible mass. A similar model could be used for a hopping robot where only one leg is required. Neglecting air resistance, assuming zero friction and perfect springs, the cost of transport for both running and hopping is 0.

Hopping is clearly an attractive locomotion method for microrobots, but continuous hopping to recycle energy effectively requires relatively complex implementation. A great deal of work has been accomplished on larger-scale robots to provide the control algorithms necessary to stabilize and propel a hopping robot forward. It is hoped that in the future, the components designed for a jumping microrobot could eventually be used in a hopping microrobot for greater travel efficiency.

## Jumping

As opposed to hopping, ballistic jumping does not use the landing to store energy for the next jump. Therefore, the robot needs to do work for each jump as seen earlier in this chapter. As above, this robot is modeled simply as a point mass  $m$  able to release energy  $U_{kinetic}$  at a take-off angle of  $\theta$ . For each jump, Equation 2.4 can be used in Equation 2.20.

$$COT_{jumping} = \frac{1}{2 \sin 2\theta} \quad (2.26)$$

An important note from Equation 2.26 is that unlike walking and wheeled locomotion above, the jumping cost of transport is velocity and scale independent. Jumping may not be the most efficient mode of locomotion for microrobots in an ideal world. However, very little internal work is required to jump in a catapult style where the robot simply extends a leg like a pogo stick, stability is less of a problem, and extra energy is not required to overcome vertical obstacles.

## Cost of Transport Comparison

The sections above describe the costs of transport using very simple locomotion models for microrobots. By comparing these equations as in Table 2.5, insight may be gained into designing efficient and usable locomotion strategies at the millimeter-size scale. For example, as mentioned above, walking and wheeled locomotion have costs of transport proportional to the square of the velocity while jumping has no velocity dependence. If high speeds are required, jumping might be the most efficient locomotion choice.

Using some values that may be typical for a millimeter-sized microrobot, Table 2.5

Table 2.5: Ideal Cost of Transport for Locomotion Models

Locomotion	Cost of Transport	Typical Values
Walking	$\frac{1}{4g} \frac{v_f^2}{l_{leg}} \frac{\sin \phi}{(\cos \phi)^2}$	0.001
Wheeled	$\frac{1}{4\pi g} \frac{v_f^2}{R}$	0.001
Running and Hopping	0	0
Jumping	$\frac{1}{2 \sin 2\theta}$	0.5

also calculates some typical cost of transport numbers for the different locomotion models. For walking and wheeled locomotion, a forward velocity of 1 cm/s is used along with 1 mm leg lengths or wheel radii. The stride angle,  $\phi$  used is  $15^\circ$ . For jumping, the take-off angle is  $45^\circ$ . Using these typical numbers, the cost of transport for wheeled locomotion or walking in an ideal world is two orders of magnitude below that required for jumping.

However, the very low typical cost of transport numbers in Table 2.5 sweep a number of practical implementation issues under the rug that are especially important for building a microrobot. A microrobot cannot (yet!) carry the sensors and computational resources to provide the balance control for a two-legged or two-wheeled robot. One way around this as demonstrated by Hollar is to drag part of the robot on the ground for a third point of stability. However, friction with the ground will add a frictional cost of transport dependent on the fraction of the robot weight supported,  $\alpha$ , and the coefficient of friction  $\mu_k$ .

$$COT_{friction} = \alpha \mu_k \quad (2.27)$$

The coefficient of friction for a silicon robot walking on a flat surface can vary, but  $\mu_k = 0.1$  would not be out of the ballpark. Another way around additional control is to add additional

actuated wheels or limbs which require more energy and add more mass.

Table 2.2.2 lists the costs of transport calculated from some of the microrobots described in Chapter 1 along with an ant for comparison. While these numbers are significantly higher than those provided in Table 2.5, it is important to note that these numbers also include actuator or muscle efficiency as well as transmission efficiency. The energy or work used in this cost of transport calculation is the total input energy to the system measured by respiratory rate for the ant and electrical input power drawn from the power supply for the microrobots. In this case, the cost of transport for the jumping microrobot is two or more orders of magnitude better than the walking microrobots in [28] and [23].

Table 2.6: Cost of Transport for Microrobots.

	Ant [49]	Hollar [28]	Ebefors [23]	Donald [24]	Proposed Microrobot
Mass (mg)	12	10	80	0.0003	10
Time (min)	0.25	417	2.8	83	1
Energy (mJ)	1.5	130	180000	6.6 <sup>a</sup>	5
COT	13	1.3·10 <sup>3</sup>	2.3·10 <sup>5</sup>	4.4·10 <sup>7</sup>	67

<sup>a</sup> Calculated from  $V = 56V$ ,  $C = 12.5\epsilon_0(120 \times 60 \mu^2)/5400\text{\AA}$ ,  $f = 16kHz$ ;

Even though jumping may not provide the most efficient means of locomotion for small robots in an ideal world, jumping provides an improvement in locomotion efficiency when robot components and fabrication techniques are taken into account. The next section will describe some of the requirements for the microrobot components to overcome the scaling challenges listed in this section.

Table 2.7: Target Sizes for Robot Components

Proposed Design	Mass (mg)
Spring	< 0.1
Motors and Chassis	5
Power Supply	2
Controller	3
Total Robot	10

## 2.3 Robot Component Requirements

Given the challenges listed above for a jumping microrobot, the microrobot components have been divided into four separate challenges: an energy storage system, high force density actuators, a power supply, and a controller. The energy storage system is required to support the actuator power challenges in Section 2.1.2 by quickly releasing stored energy for a jump. High force, large displacement motors store energy in the energy storage system. Given the definition of autonomy in Chapter 1, a controller is required to control the actuators, and a power supply is required to power the actuators and the controller.

The basic requirements of each component are discussed below and more detailed requirements are given in the following chapters. Obviously each component should be small, light, and consume low power due to the cost of carrying a power supply on the robot. A list of target masses is given in Table 2.7.

### 2.3.1 Energy Storage

An energy storage system is required to support the actuator power challenges in Section 2.1.2 by quickly releasing stored energy for a jump. While details regarding materials and design are discussed in detail in Chapter 3, this section briefly discusses some of the basic requirements for an energy storage system.

As stated above, the energy storage component should be small and lightweight and Table 2.7 lists a negligible target mass (less than 0.1 mg). These restrictions will impose constraints on the fabrication methods and materials used in the energy storage system. In addition, the energy storage system should be highly efficient. The energy stored by the actuators should be delivered as efficiently as possible to the robot in flight, and efficiency will be largely determined by the material used for the spring. The energy storage system developed should also integrate easily with the motors described in the following section.

Finally, the energy storage system should be able to store relatively large amounts of energy. The jumping trajectories targeted in Figure 2.3 require initial kinetic energies of 1, 5, 10, or 25  $\mu\text{J}$ . A simple linear spring can be modeled to gain perspective on what these energy values imply for the energy storage system.

$$U_{strain} = \frac{1}{2}Fx = \frac{1}{2}kx^2 = \frac{1}{2}\frac{F^2}{k} \quad (2.28)$$

$F$  is the force applied to the spring by the actuator,  $x$  is the distance the spring is stretched by the actuator, and  $k$  is the spring constant. Figure 2.13 displays the forces and displacements that the spring should be able to withstand for the given energies.

Assuming a relatively modest 40% conversion rate from energy stored in the spring to energy available at takeoff, a force/displacement value of 10 mN/5 mm from the 25  $\mu\text{J}$

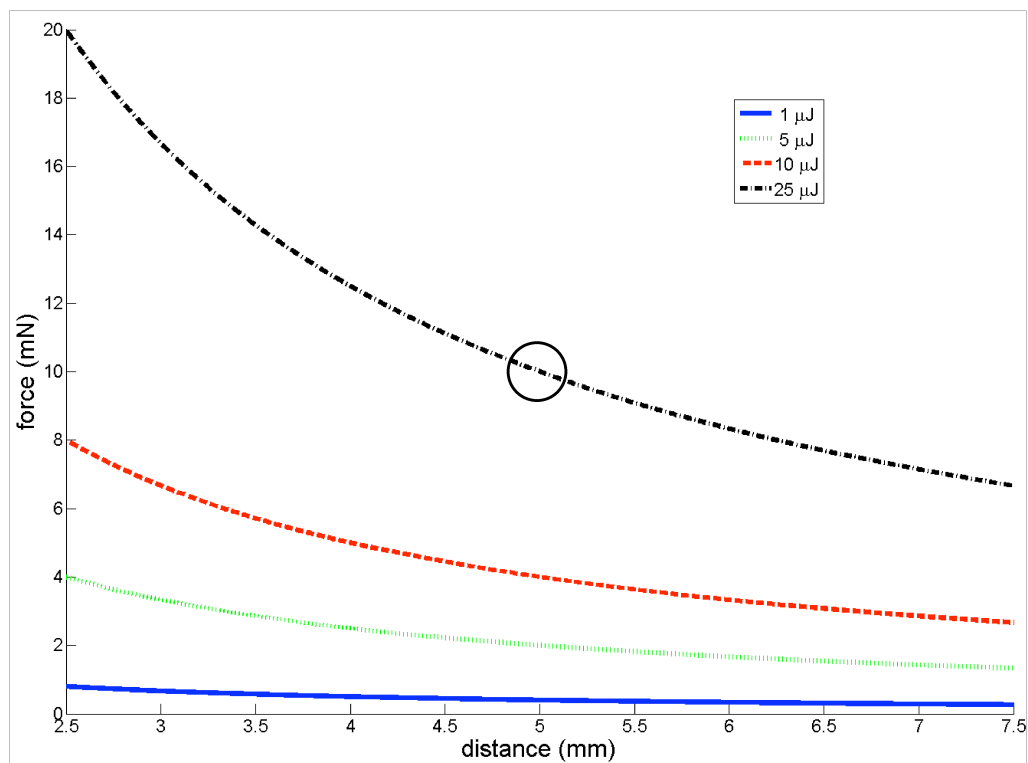


Figure 2.13: Force/Displacement Requirements for a Linear Spring.

curve should be sufficient to provide  $10 \mu\text{J}$  for the jump. While any value along this curve may be chosen, these two numbers are chosen as a starting point and design trade-offs may be made later in the design process. Regardless, the energy storage system will need to be able to withstand milliNewton forces and millimeter displacements.

### 2.3.2 Actuation

While the energy storage component quickly releases energy for a jump, an actuator is required to store the energy in the first place. The target size for the actuator is less than 5 mg. These dimensions will require a high work output to mass ratio (J/kg). The

work output can be quantified given the forces and displacements discussed in the previous section. Assuming a linear spring, the target actuator specifications are 10 mN of force and 5 mm of displacement. Previously designed actuators of this size will be discussed further in Chapter 4, but these forces and displacements are approximately an order of magnitude greater than what has been demonstrated. The actuator should also be able to provide these forces and displacements at a reasonable speed. The robot should be able to take several jumps per minute.

In addition to size, mass, force, and displacement requirements, the actuator should also provide all of these requirements given relatively low input powers at moderate voltages. The definition of autonomy in Chapter 1 requires the robot to carry its power supply on-board. Existing power supplies as discussed in Chapter 5 generally provide low power (on the order of  $\mu\text{W}$ ) and low voltages (volts to tens of volts). The actuator designed for an autonomous jumping microrobot should be matched to the chosen power supply to minimize mass. Finally, the actuator should be simply fabricated. There are multiple reasons for this requirement – quick turnaround time in the design cycle, less time in the cleanroom, and ideally, compatibility with a commercially available process.

### 2.3.3 Power

Designing an appropriate power supply for an autonomous jumping microrobot offers one of the most difficult challenges. This power supply should provide enough energy for multiple jumps (preferably rechargeable in some fashion), occupy small area and mass, and offer simple integration to the actuators. The target mass in Table 2.7 is 2 mg compared to some of the smallest and lightest batteries on the market generally around 1 g [50]. Energy

for multiple jumps will be determined by the capacity of the power supply or the availability of power in different environments from scavenging methods.

As stated in the above section, matching the power supply to the actuators is crucial for both power efficiency and added mass. Many batteries are available at low voltages, but would require additional power circuitry, and therefore significant extra mass and area, to provide the high voltages required by many actuators.

#### **2.3.4 Control**

Finally, the robot requires a controller to sequence the motors at the appropriate times. Ideally this controller can eventually be used to handle sensors on the robot as well, but for now, mobility is the only requirement for this jumping microrobot. Naturally, size and mass should be kept to a minimum and 3 mg has been budgeted in Table 2.7. Due to limited power available, the controller should draw only microWatts of power and also be well matched to the power supply. Simple integration is important as will be discussed further in Chapter 5. Finally, the controller should be as programmable as possible in order to allow for small design changes and future sensor integration.

## Chapter 3

# Micromechanical Energy Storage

As discussed in Chapter 2, a micromechanical energy storage system can help provide high mechanical output power for a jumping microrobot. While the intended use of such a system in this work is to quickly release stored energy for a jump, energy storage and quick release could potentially be useful in a number of other applications where short bursts of power are required. Microjet injectors [51], initiators [52], and even catapults for communicating with extraterrestrials [53] are among the potential applications.

Despite the utility of such a system and the broad use of systems to quickly release stored mechanical energy in the macro world, very few examples have been demonstrated in millimeter scale systems. Perhaps the most common method of energy storage is through batteries or capacitors [54, 55]. Many MEMS systems only require electrical power for sensors which makes these storage methods particularly attractive. Another related area of research is in mechanical energy scavenging. In these cases, piezoelectric or capacitive structures are used to scavenge mechanical energy which is then converted to and stored as

electrical energy to power sensors and other low power devices [56, 57]. However, in cases where direct mechanical power has been required, chemical energy has been stored in solid fuels for use in microrockets [58]. These microrockets could be considered in a similar class to the Sandia piston robot discussed in Chapter 1 [31].

Despite these other energy storage methods, only one MEMS system has been found that stores and quickly releases mechanical energy [52]. In order to demonstrate and characterize the motors and gearing developed in the Sandia SummitV process, Rodgers demonstrated a mechanical energy storage system using polysilicon bending springs and a polysilicon fuse for release. This system stored an estimated 19 nJ of energy although it is not clear that the fuse was ever blown for the energy to be released. Chapter 2 showed that the autonomous jumping microrobot will need to store and quickly release approximately 3 orders of magnitude more energy than the system demonstrated here.

### 3.1 Design

A number of factors should be considered while designing and fabricating an energy storage system for the microrobot, and a number of tradeoffs exist in the design space. While designing an energy storage system, robot jumping performance will depend on the spring linearity and material as well as the ability of the energy storage system to integrate with the motors discussed in Chapter 4. This section will examine different spring materials and designs to weigh the tradeoffs of spring energy density, efficiency, fabrication, and integration. For example, silicon springs may be simple to fabricate and integrate with certain MEMS actuators as shown in [52], but they will not integrate well with the force

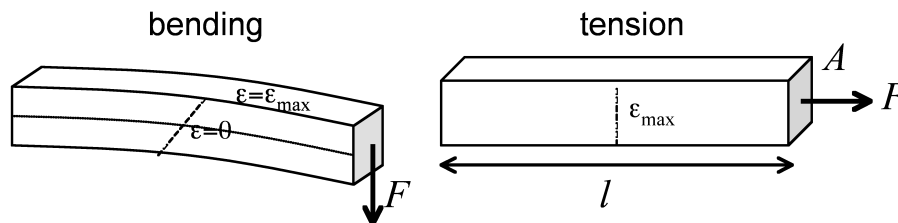


Figure 3.1: Strain Energy in Bending and Tension.

limited motors discussed in Chapter 4.

### 3.1.1 Energy Density

One of the simplest ways to store mechanical strain energy is through tension as done in rubber bands and tendons. If energy is stored in a piece of material by bending it, the strain profile is no longer constant through the material. Since energy is proportional to strain squared, bending will store less energy than providing a constant strain through the material using tension (Figure 3.1).

Table 3.1: Possible Spring Material Characteristics

Material	Young's Modulus (GPa)	Yield Strength (MPa)	Energy/Vol (mJ/mm <sup>3</sup> )	Energy/Mass (mJ/mg)
Silicon[59]	190	500	0.66	0.28
Resilin[60]	0.002	3	2.25	2.1
Locust Apodeme[60]	20	600	9	7.5
PDMS[61, 62]	0.00075	2.2	3.3	3.4
Parylene[63]	3.2	55	0.5	0.4
Polyimide[64]	3.3	64.3	0.6	0.4
Polyurethane[65]	0.0076	38	95	76
Latex[65]	0.0001	1	5	4

The energy density is dependent on material characteristics given in Table 3.1.

Given a simple beam in tension as shown in Figure 3.1, the maximum distance this beam may be elastically stretched is described by  $x_{max}$  where  $l$  is the length of the beam,  $\tau$  is the yield strength of the material,  $E$  is the Young's Modulus, and  $\epsilon_{max}$  is the maximum elastic strain supported by the material.

$$x_{max} = \frac{\tau l}{E} = \epsilon_{max} l \quad (3.1)$$

The maximum force which can be applied to the beam is described by  $F_{max}$  where  $A$  is the beam cross-sectional area.

$$F_{max} = A\tau = AE\epsilon_{max} \quad (3.2)$$

Therefore, the maximum energy which can be stored in the material is described by  $U_{max}$ .

$$U_{max} = \frac{1}{2} F_{max} x_{max} = \frac{1}{2} \frac{Al\tau^2}{E} = \frac{1}{2} AlE\epsilon_{max}^2 \quad (3.3)$$

The energy stored in a given volume of material is

$$\frac{U_{max}}{Volume} = \frac{1}{2} \frac{\tau^2}{E} = \frac{1}{2} E\epsilon_{max}^2 \quad (3.4)$$

and the energy stored in a given mass is

$$\frac{U_{max}}{Mass} = \frac{1}{2} \frac{\tau^2}{\rho E} = \frac{1}{2} E\epsilon_{max}^2 \quad (3.5)$$

Relevant material properties are given in Table 3.1. Resilin and locust apodeme (cuticle) are both materials used as springs in insects. Resilin is a soft, rubbery material used in shear and compression for very small insects like fleas, and cuticle is a stiffer material used in bending modes in somewhat larger insects like locusts. Because the energy density of these materials is so high, the mass of the spring compared to the mass of the insect often allows for the springs to be used in less efficient modes such as shear and bending compared

to tension. Silicon, poly dimethylsiloxane (PDMS or silicone), parylene and polyimide are provided as examples of materials common to microfabrication and range from stiff and brittle silicon to soft and flexible silicone. Polyurethane and latex are other elastomers available off-the-shelf with thicknesses of approximately  $50\ \mu\text{m}$  in condoms and angioplasty balloons.

As seen in this table, the practical strain limit of silicon reduces its energy storage density to over two orders of magnitude below polyurethane. However, the significance of these numbers is slight for the amount of energy in question. The spring mass required to store the  $25\ \mu\text{J}$  targeted in Chapter 2 is  $89\ \mu\text{g}$  for silicon and  $0.33\ \mu\text{g}$  for PDMS for a mass penalty of approximately  $89\ \mu\text{g} - 0.9\%$  of the total robot mass. Stiffer materials also have a number of tradeoffs including the high force or high mechanical advantage required by the actuators and robot skeleton. Low modulus materials like resilin make it simpler to integrate the spring with lower force actuators and simple skeletal structures. These integration tradeoffs will be discussed further in Section 3.1.4.

### 3.1.2 Spring Efficiency

Spring efficiency can be characterized in multiple ways, but in this section, spring efficiency will ultimately relate the amount of kinetic energy delivered to the robot during takeoff to the amount of potential energy originally stored in the spring. The spring material will affect efficiency through energy losses due to heat or other mechanisms that occur while stretching the material. The mechanical design of the spring will also have an effect however. If a significant portion of the energy delivered to the robot occurs towards the end of the ideal takeoff time, a robot that takes off before this ideal time will lose a substantial portion

of the energy stored in the spring.

All of the materials above experience some amount of energy loss as they stretch. In polymers, the long, convoluted molecular chains composing the polymers are straightened when the material is stretched, losing some amount of energy to friction and heat. In a material like silicon, very little energy is lost due to the rigid crystalline nature of the material. Polymers are somewhat more complex and energy loss can be characterized by the dissipation factor,  $\tan(\delta)$  where  $\delta$  is the ratio between the complex modulus which determines viscosity and the real modulus which governs elasticity. A higher dissipation factor indicates a more viscous material more likely to lose energy when stretched [66].

As a concrete example of this, a macro-scale experiment was set up to characterize the stress/strain curves of natural rubber latex and polyurethane. Successive masses were added to increase the force on one end of the piece of rubber while the amount stretched was measured with a ruler. These masses were then removed to measure the amount of energy released from the spring. Dissipation factor depends heavily on the rate at which the spring is stretched and released and this experiment only characterized a very slow rate due to the manual nature of adding and removing masses. As can be seen in Figure 3.2, polyurethane, which has a dissipation factor of 0.034 at 1 kHz and an even greater 0.14 at 100 Hz, clearly shows a greater hysteresis than the latex which has a dissipation factor of 0.005 at 1 kHz<sup>1</sup> [65]. In fact, only 55% of the energy stored in the polyurethane is returned versus 97% for the latex. Latex and any other material with a similarly low dissipation factor will remain a highly efficient spring material and will allow most of the energy stored

---

<sup>1</sup>Polyurethane and latex dissipation factor numbers are given for materials similar to the commercially available materials tested in Figure 3.2

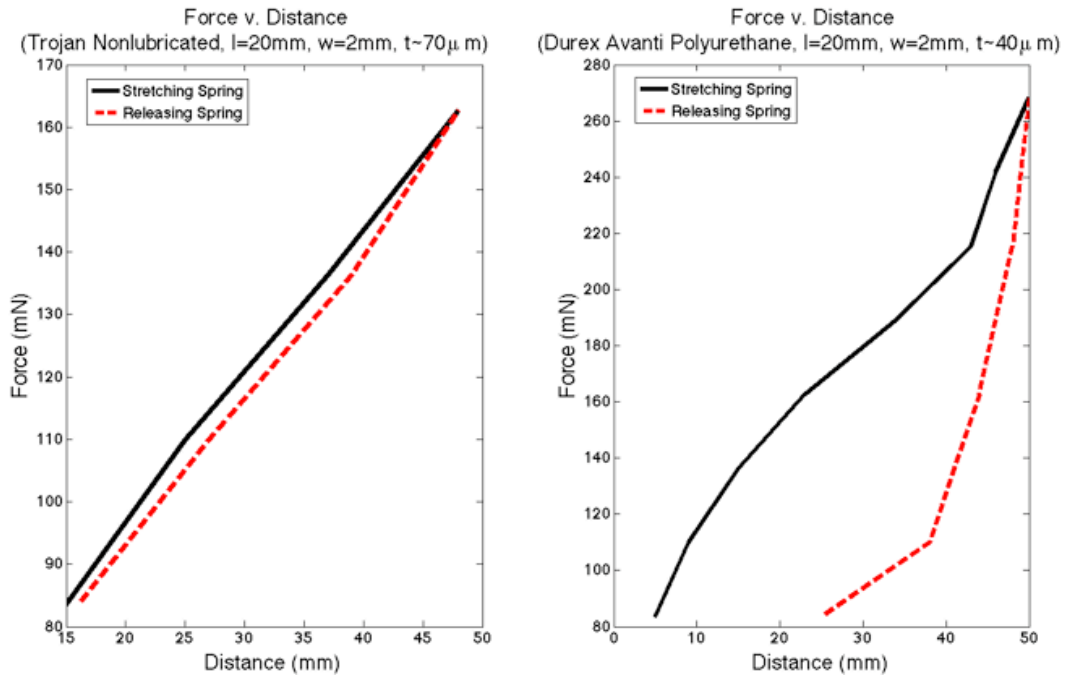


Figure 3.2: Force/Distance Tests for Latex and Polyurethane. The latex returned 97% of the stored energy while the polyurethane only returned 55% of the stored energy.

in the spring to be delivered to the robot upon takeoff. In a related note, the biological material resilin is a highly efficient and resilient spring material and efforts are underway to create a synthetic resilin to provide similar properties [67].

However, even if the material used for the energy storage system is highly efficient, the energy released by that material still needs to be delivered efficiently to the robot. One consequence of a linear spring as discussed in Section 2.1.2 is that the robot may be susceptible to early liftoff as reported by Burdick and Fiorini in [68]. When the force delivered from the spring is significantly greater than the weight of the robot, the robot may leave the ground before the leg is fully extended and all of the energy from the spring is converted to kinetic energy. While a linear spring may be simple to fabricate and model,

its design has consequences on the jumping microrobot's performance. Assuming that the surface the robot is taking off from in Figure 2.6 is perfectly stiff, the robot's position during takeoff is described by

$$y(t) = l_0 (1 - \cos(\omega t)) \quad (3.6)$$

where  $l_0$  is the leg length compensated by gravity  $l_{leg} - g/\omega^2$ ,  $l_{leg}$  is the original leg length and characteristic of the robot's size,  $\omega$  is the robot's resonant frequency  $\sqrt{k_{leg}/m_{robot}}$ ,  $k_{leg}$  is the spring constant of the spring making up the energy storage system, and  $m_{robot}$  is the mass of the robot. The power can be integrated to obtain the amount of kinetic energy delivered to the robot over time which is plotted in Figure 3.3.

$$E(t) = \frac{1}{4} k l_0^2 (1 - \cos(2\omega t)) \quad (3.7)$$

If, however, the spring was not linear but required a constant force while stretching, the equations and energy delivered to the robot happen on a different timescale as seen in Figure 3.3. In the case where a constant force  $F_s$  is used to propel the robot upwards, the robot's position during takeoff is described as

$$y(t) = \frac{1}{m} (F_s - mg) \frac{t^2}{2} \quad (3.8)$$

and the kinetic energy delivered to the robot is

$$E(t) = \frac{1}{m} (F_s - mg)^2 \frac{t^2}{2} \quad (3.9)$$

The force,  $F_s$  has been scaled by half so that both systems deliver the same amount of energy, although they do it in different amounts of time. If the times are normalized, the linear spring delivers 50% of its energy by  $0.5t_{takeoff}$  while the constant force spring

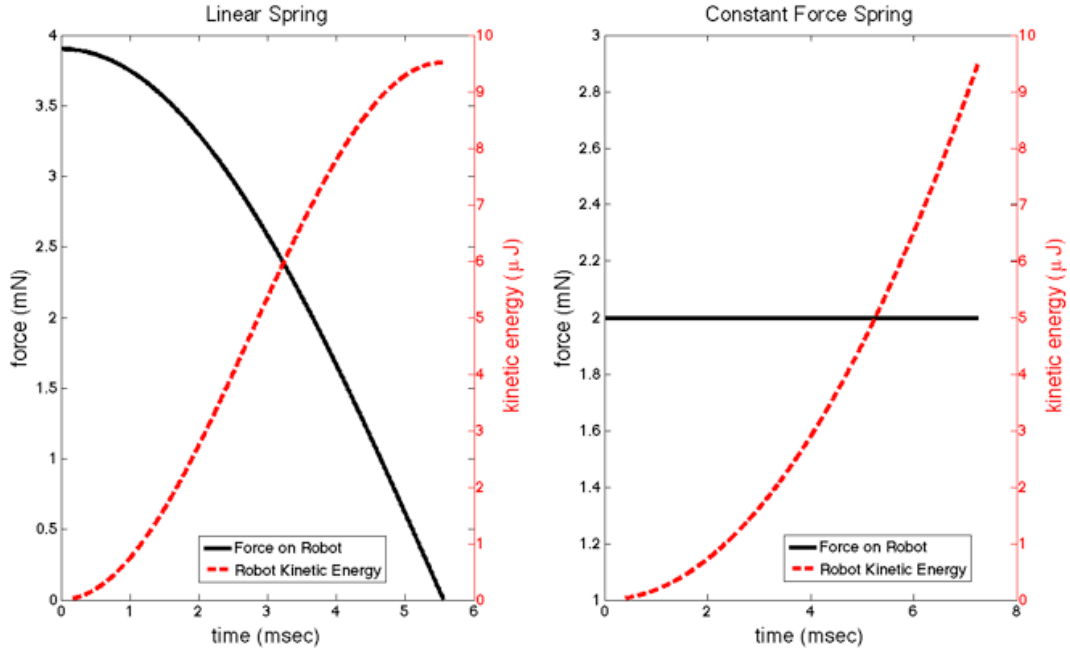


Figure 3.3: Energy Delivered from Linear and Constant Force Springs. The linear spring delivers kinetic energy more quickly, but requires higher forces.

delivers the same amount of energy in  $0.71t_{takeoff}$ . However, it is important to note that the force on the robot at  $t = 0$  is less in the constant force spring case than the linear spring case, which may make the robot less susceptible to jumping early.

By utilizing springs with additional mechanisms, even more interesting characteristics emerge. In Figure 3.4, a linear spring is used in a more complex configuration similar to the one used by Burdick and Fiorini in [68], and the force/distance profile becomes nonlinear as seen in Figure 3.5.

$$F(y) = ky \frac{\left(\sqrt{4l^2 - y^2} - l_0\right)}{\sqrt{4l^2 - y^2}} \quad (3.10)$$

where  $k$  is the spring constant of the linear spring,  $y$  is the leg extension from the ground,  $l$  is the beam length in the 4-bar mechanism, and  $l_0$  is the natural length of the linear spring.

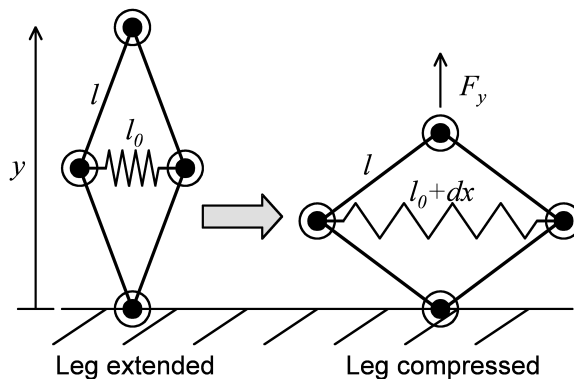


Figure 3.4: Linear Spring in a Nonlinear Force/Distance Profile Configuration.

Figure 3.5 also shows the energy delivered to the robot by the spring if it is compressed to an initial  $y = 1$  mm, and is solved using  $k = 2$  mN/mm,  $l_0 = 2$  mm, and a total leg extension of 5 mm.

By providing the maximum thrust force in the middle of the leg extension, Burdick and Fiorini demonstrated that the robot was less likely to leave the ground before more energy was delivered to the robot. Even though the nonlinear spring delivers 50% of its energy by  $0.77t_{takeoff}$  compared to  $0.5t_{takeoff}$  for the linear spring, the low force profile at the beginning of the jump meant that the spring was more efficient in delivering kinetic energy to the robot. The tradeoff, however, comes from the difficulty in fabricating a mechanism like this on the microscale.

### 3.1.3 Spring Fabrication

The practicality of the materials and spring designs discussed thus far will depend heavily on fabrication capabilities, and the difficulty in fabricating these springs will be primarily governed by integration with the motors. While it is not simple to quantify

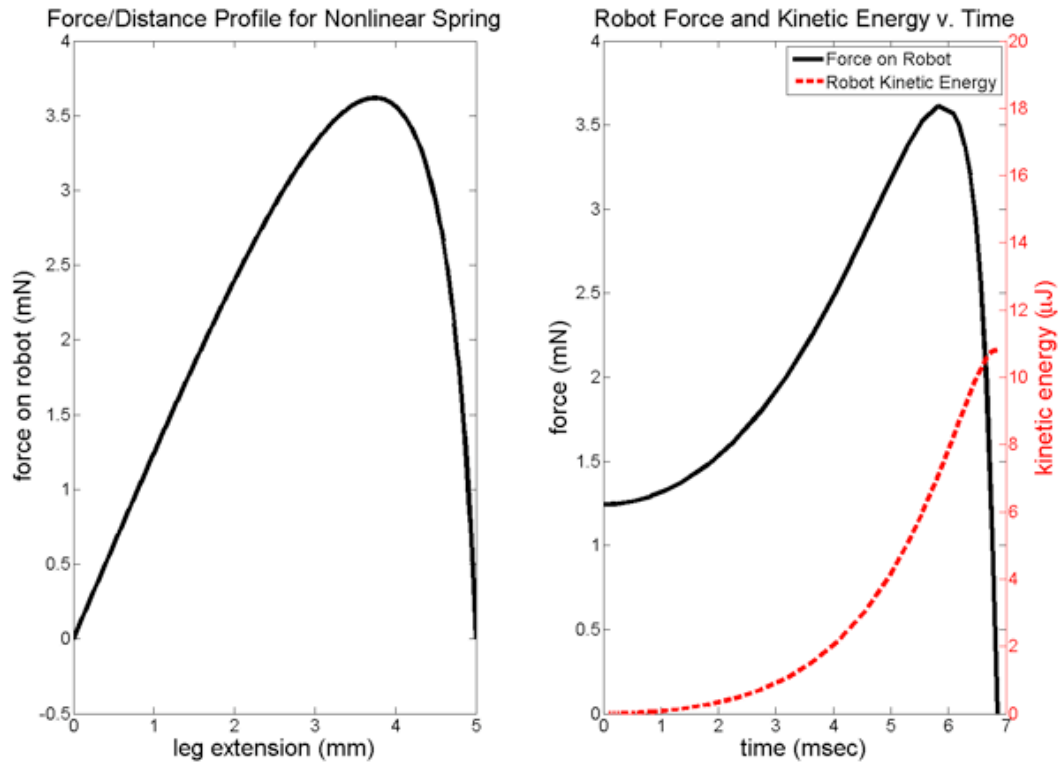


Figure 3.5: Nonlinear Spring Force. The figure on the left shows the force/distance profile of the spring in Figure 3.4. On the right, the force on the robot and the kinetic energy delivered to the robot is plotted versus time.

these challenges, it can be assumed that the robot motors will be fabricated in a silicon MEMS-based process and previous work is used to evaluate some measure of compatibility with these processes. Table 3.2 provides relative measures of fabrication simplicity for the materials and designs discussed above.

Given that the actuators are fabricated in a silicon MEMS process, silicon springs may in fact be the simplest to fabricate with silicon motors as was seen in [52]. Recent work by Suzuki and Tai has shown parylene springs integrated with silicon parts for use in inertial sensors although this adds an extra mask step to the fabrication process [69]. Mahadevon used polyimide for springs to measure the work done by microactuators in [64]. Currently,

Table 3.2: Fabrication Complexity for Spring Materials and Designs

Materials	Silicon	easy
	PDMS	medium/difficult
	Parylene	medium
	Polyimide	medium/difficult
	Polyurethane	medium/difficult
	Latex	medium/difficult
Design	Linear Spring	easy
	Constant Force Spring	difficult
	Nonlinear Spring (Fig. 3.4)	difficult

the most common polymer used in MEMS is PDMS although it is generally used with soft lithography to build microfluidic devices at large scales. However, Tung and Kurabayashi used PDMS as a spring material with silicon actuators, albeit with a relatively complex fabrication process [70].

Spring design is also heavily dependent on the fabrication techniques used. Most MEMS springs have been used in bending modes, and these linear springs are simple to fabricate and use. A constant force spring would require a complex material or mechanisms surrounding it. Finally, the nonlinear spring in Figure 3.4 requires the use of in-plane pin hinges which are notoriously complex in silicon MEMS systems due to the surface forces at small scales [71].

Fabrication, however, may be simplified in a number of ways. The post-process assembly of simple silicon parts in a one-mask process was recently demonstrated by Last in [72] and similar ideas may be translated to the fabrication of an energy storage system. Materials like PDMS which have not been fabricated with silicon structures in the past may instead be assembled post-process. In a linear spring configuration, this may be as simple

as assembling a very tiny rubber band. Innovations with fabrication should be taken into account when designing an energy storage system for a jumping microrobot.

### 3.1.4 Spring Integration

Not only does the energy storage system need to be attached to the motors, it should also match the characteristics of those motors. The material properties listed in Table 3.1 provide data to calculate the forces and displacements that the material can support if designed as a beam placed in tension (Figure 3.1). This section examines the capability of the spring materials and designs discussed above to match with the actuators which will be described later in Chapter 4.

Table 3.3: Spring Sizes for Different Materials in Tension

Material	Length (mm)	Area ( $\mu m^2$ )
Silicon	1900	20
Resilin	3.3	3300
Locust Apodeme	170	17
PDMS	1.7	4500
Parylene	290	180
Polyimide	260	160
Polyurethane	1	260
Latex	0.5	10000

Table 3.3 lists the dimensions required for a beam in tension to support the force/displacement characteristics of the actuators discussed in Chapter 2 (10 mN and 5 mm respectively). While the stiffer materials would generally be used in bending instead of tension, this table provides a rough idea of the compatibility of these spring materials with the actuators. For example, a PDMS spring requires a length of 1.7 mm and a

cross-sectional area of  $45 \times 100 \mu\text{m}^2$  to support these forces and displacements, and a spring with these dimensions would be straightforward to fabricate and fit into a millimeter-sized microrobot. On the other hand, a silicon spring would require a length of 1.9 m and a cross-sectional area of  $4 \times 5 \mu\text{m}^2$  – a significantly greater challenge for fabrication and integration into a robot of this size. PDMS, in fact, matches very well with the force-limited actuators used in this millimeter-sized jumping robot due to the high strains it supports.

In addition, the maximum force required by the actuator to stretch a spring and hold it in place are listed in Table 3.4. A linear spring requires a linear increase in force as the spring is stretched, with the maximum force required when the robot is ready for launch. The nonlinear spring in Figure 3.4 requires a maximum force similar to the linear spring, but only a very small clamping force when the spring is fully stretched.

Table 3.4: Motor Forces Required by Spring Designs

Design	Maximum Total Force (mN)	Force to Hold for Launch (mN)
Linear	4	4
Constant Force	2	2
Nonlinear	3.6	1.25

### 3.1.5 Spring Design Summary

Obviously, a number of factors need to be taken into account when designing the energy storage system for an autonomous jumping microrobot. In an ideal world, the energy storage system would require no mass or volume, be 100% efficient at transferring stored strain energy to robot kinetic energy, be simple to fabricate with the silicon motors, and would perfectly match the force/displacement characteristics of those motors. In reality,

the spring materials and designs described above offer a number of tradeoffs between those design goals as listed in Table 3.5.

Table 3.5: Spring Design Tradeoff Summary

		Density	Efficiency	Fabrication	Integration
Materials	Silicon	average	good	excellent	abysmal
	PDMS	good	good	average	excellent
	Parylene	average	good	good	poor
	Polyimide	average	good	poor	poor
	Polyurethane	excellent	abysmal	average	average
	Latex	good	good	average	excellent
Design	Linear (in tension)	n/a	average	excellent	good
	Constant Force	n/a	poor	poor	excellent
	Nonlinear (Fig. 3.4)	n/a	good	abysmal	good

In the end, it was determined that a linear elastomer spring offered the greatest number of benefits and least number of drawbacks in building an autonomous jumping microrobot. PDMS is small, lightweight, efficient, and matches the actuators described in Chapter 4 very well. The fabrication drawback of integrating PDMS with silicon actuators will be solved by using a post-process assembly technique described in the next section. One of the simplest examples of a linear elastomer spring is the rubber band. The next few sections will discuss the fabrication and characterization of micro rubber bands for autonomous jumping microrobots.

## 3.2 Fabrication

In order to simplify the fabrication component for a PDMS-based energy storage system, new fabrication methods need to be explored. Microassembly is slowly becoming

more popular as a MEMS fabrication technique [72, 73]. While microassembly has only been used to create more complex silicon structures, it is also possible to use the same general idea to create more complex MEMS structures by assembling components made of differing materials. In this case, assembling separately fabricated silicone micro rubber bands onto silicon structures offers a significantly simpler method of fabrication. In addition, using separate fabrication methods for both the silicone and silicon components allow each to be fabricated in more optimal processes. The best elastomer may be used regardless of its compatibility with the silicon process. A simple two-mask silicon process is used to build high force motors (discussed further in Chapter 4), attachment hooks, and test structures to characterize the elastomers. To fabricate the micro rubber bands, both a laser cutting method and molding process are demonstrated and compared. Once both parts have been fabricated, the micro rubber bands are manually assembled.

### 3.2.1 Silicon Fabrication

The primary goals of the silicon fabrication process are to build actuators capable of storing energy in the micro rubber bands, and to fabricate attachment points for connecting micro rubber bands to those actuators. The actuators will be discussed further in Chapter 4 and are fabricated in a process similar to the single-mask silicon-on-insulator (SOI) process described by Yeh [74]. While the actuators in Chapter 4 may be fabricated in a single-mask process, the attachment points for assembling the micro rubber bands into the inchworm motors require a backside etch to leave room for the rubber bands to extend through the wafer. Simple hooks (Figure 3.6) were chosen as attachment points and are fabricated in the top layer of an SOI wafer.

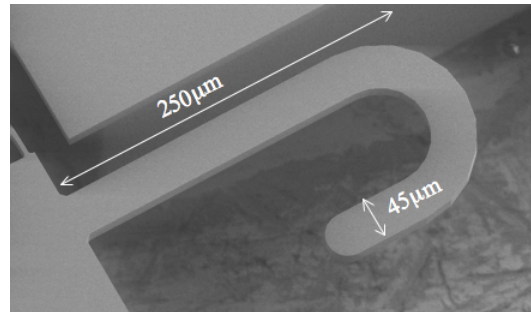


Figure 3.6: Silicon Hook for Assembling Micro Rubber Bands. The hook is fabricated in the top layer of an SOI wafer and in this case is  $20 \mu\text{m}$  thick,  $250 \mu\text{m}$  long, and  $45 \mu\text{m}$  wide.

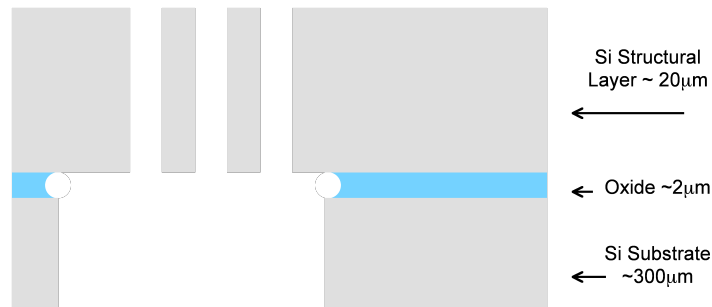


Figure 3.7: Two Mask SOI Process for Fabricating Silicon Components. A deep reactive ion etch is used on each side of the SOI wafer to define silicon structures for the energy storage system.

The final result is a simple two-mask process that etches both sides of an SOI wafer (Figure 3.7). The process starts on a 4-inch SOI wafer with a  $20 \mu\text{m}$  structure layer (frontside),  $2 \mu\text{m}$  buried oxide (BOX), and  $300 \mu\text{m}$  substrate (backside). The front is patterned first and etched using a Surface Technology Systems (STS) Advanced Silicon Etch. The exposed buried oxide is removed using an RIE oxide etcher and the front is protected by depositing  $0.6 \mu\text{m}$  of low temperature oxide (LTO). The backside is aligned and patterned using a Karl Suss contact printer with backside alignment. Another STS Advanced Silicon Etch is used to etch through the backside, terminating on the BOX layer

or LTO deposited earlier. Finally, the structures are released using a timed 49% HF wet etch and a critical point dry.

This very simple process provides all of the silicon components required for an autonomous jumping microrobot such as the actuators, robot chassis, hooks for assembling micro rubber bands, characterization structures, etc. Another benefit of keeping the silicon process as simple as possible is that a very similar process is commercially available on shuttle runs through SOIMUMPs which makes following a similar process flow simpler without extensive cleanroom facilities [75]. However, the more novel aspects of the energy storage fabrication are shown in the next sections with the elastomer fabrication and assembly.

### **3.2.2 Elastomer Fabrication**

While processes similar to the silicon process described above are very common in MEMS, processes to pattern PDMS into micro rubber bands are significantly less common. However, in recent years microfluidics have led the charge in simple fabrication of bulk PDMS devices. In this work, two different processes are used to fabricate the elastomer springs and each is distinguished by the method in which the elastomer is patterned. The first method cuts the elastomer using a laser and the second uses a silicon mold to define the spring shape. The laser cutting method provides a desktop rapid prototyping solution to a MEMS problem, and benefits include no cleanroom time plus quick turnaround time in the design cycle. Molding PDMS is a more traditional MEMS approach and many microfluidic devices have been fabricated using molding and soft lithography. Molding helps create significantly more definable and repeatable PDMS structures.

Both the laser cutting and molding fabrication methods currently use Dow Corning

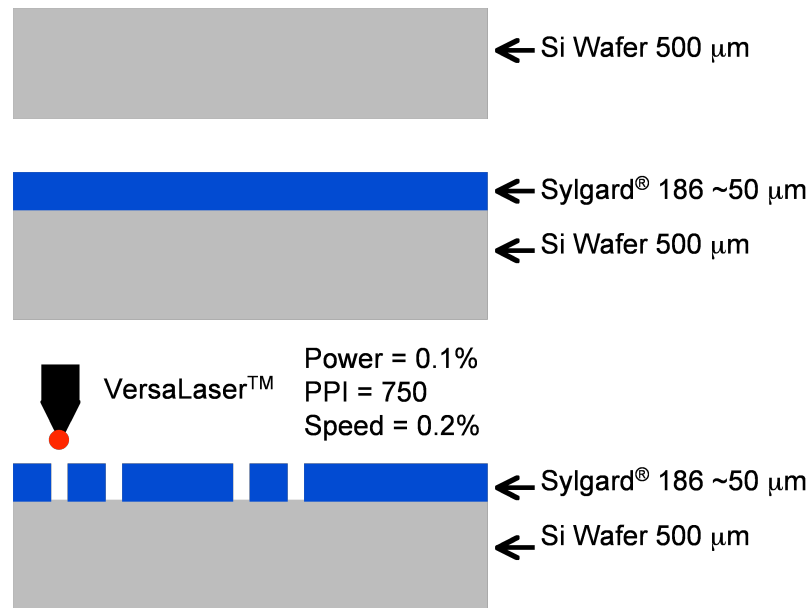


Figure 3.8: Laser Cutting Process. Micro rubber bands can be laser cut from spun-on silicone rubber using a VersaLaser<sup>TM</sup> IR commercial laser cutting tool.

Sylgard ® 186 silicone for the elastomer, although preliminary testing has begun on a number of other elastomers. Sylgard ® 186 was chosen due to its high tear strength and high strains previously characterized by Pelrine in [76]. However, Sylgard ® 186 also has a relatively high viscosity of 65,000 cps making it difficult to work with. To thin the Sylgard ® 186, it is mixed with Dow Corning 200 ® Fluid (50 cst) at a ratio of 10:1 by weight. In addition, before use in either fabrication method, the mixture is placed in vacuum at approximately 1 torr for 30 minutes to reduce the number of bubbles and produce a higher quality silicone.

### Laser Cutting

The first method, laser cutting, does not require the use of a clean room and provides a fast turnaround time. Thinned Sylgard ® 186 is spun onto a silicon wafer

to a thickness of approximately  $50\ \mu\text{m}$  by slowly ramping the spinner speed to 3500 rpm and holding it for 60 seconds. After curing the silicone at  $100^\circ\text{C}$  for 45 minutes, a 25 W VersaLaser<sup>TM</sup> VL-200 IR commercial laser cutting tool with standard lens is used to cut the elastomer into desired patterns. Patterns are designed as a SolidWorks<sup>TM</sup> drawing and are “printed” onto the silicone using the VersaLaser<sup>TM</sup> print driver where power, pulses per inch (PPI), and speed are all definable options. The best settings found thus far for cutting Sylgard<sup>®</sup> 186 are Power = 0.1%, PPI = 750, and Speed = 0.2% (percentages are defined relative to maximum values internal to the VersaLaser<sup>TM</sup>). The process flow is shown in Figure 3.8.

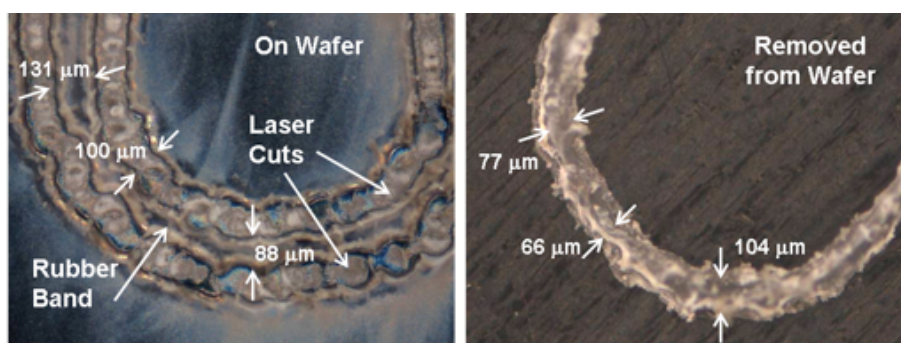


Figure 3.9: Laser Cut Rubber Bands. Micro rubber bands fabricated using the laser cutting process are quick and easy, but suffer from low yield and erratic edges.

While the laser cutting process is quick and easy, it isn't perfect. The cuts provided by the laser result in jagged edges, and the positional resolution is on the edge of “good enough” to cut out  $75\ \mu\text{m}$  wide rubber bands (Figure 3.9). In fact yield is generally only 10-20% due to errant cuts that slice holes through the rubber band. In addition, patterning anything other than circular bands can be difficult with the VersaLaser<sup>TM</sup> due to these same errant cuts.

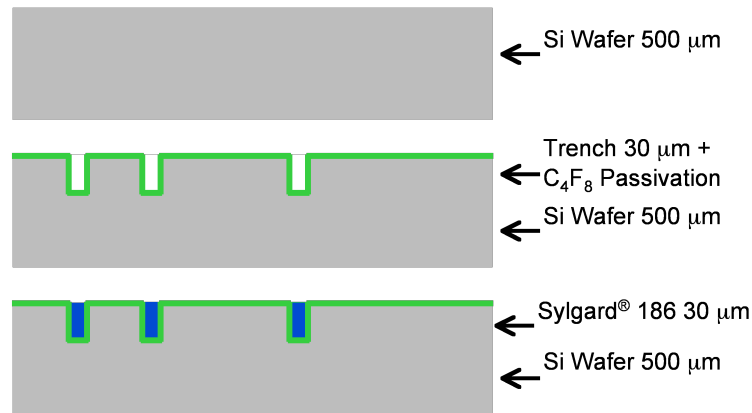


Figure 3.10: Elastomer Molding Process. Micro rubber bands can also be fabricated by using a micromachined mold.

## Molding

Molding provides higher quality rubber bands, higher yield, and more flexibility in spring design. In this fabrication method (Figure 3.10), silicon molds are fabricated by patterning and etching a silicon wafer using the same STS Advanced Silicon Etch used to fabricate the silicon components. The molds are then passivated, using a process similar to that described by Gao in [77]. However, in this process,  $C_4F_8$  gas is used at 600 W for 3 minutes to passivate the mold. Thinned and vacuumed Sylgard<sup>®</sup> 186 silicone is then poured into the mold and placed into the vacuum for an additional 30 minutes. Finally, the excess silicone is scraped off with a razor blade and the silicone remaining in the trenches is cured at 100°C for 45 minutes. After curing, it is possible to simply remove the rubber with tweezers (Figure 3.11). Micro rubber bands with three different thicknesses were fabricated: 20  $\mu\text{m}$ , 30  $\mu\text{m}$ , and 40  $\mu\text{m}$ .

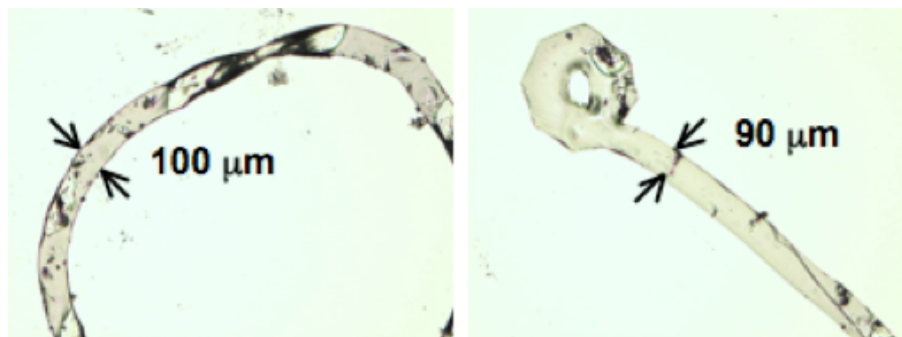


Figure 3.11: Molded Rubber Bands. Micro rubber bands fabricated through molding have significantly cleaner edges and higher yield, but suffer from longer processing times.

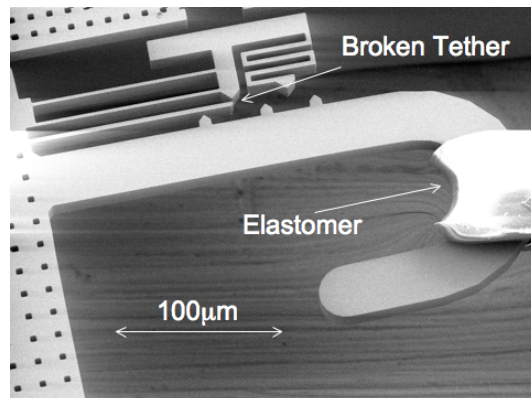


Figure 3.12: Silicon Hook with Assembled Elastomer. Micro rubber bands are assembled onto silicon hooks using fine tip tweezers under a stereo inspection microscope.

### 3.2.3 Elastomer Assembly

After both silicon microstructures and micro rubber bands have been fabricated, fine point tweezers are used to assemble rubber bands onto silicon hooks under a stereo inspection microscope (Figure 3.12). Since at least one of the hooks is generally connected to a moving part, it is critical to assembly success that the moving part be tethered during assembly (Figure 3.13). These tethers need to be strong enough to resist forces encountered during assembly from tweezers or silicone, yet easy enough to break after assembly

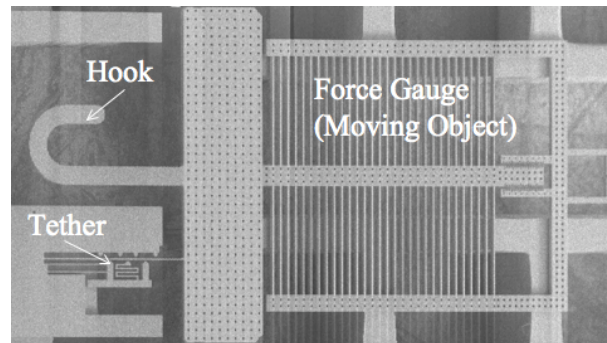


Figure 3.13: Tethered Moving Part Before Assembly. Moving parts are tethered for assembly purposes and the tether is later broken so that the part can move freely.

is completed. A tether design similar to Last's tethers in [78] was used and found to be suitable for this application. Assembly yield has been approximately 80% with failures usually resulting from sudden hand movements, although assembly time and success rate have improved substantially with practice.

### 3.2.4 Pre-Strain

All of the micro rubber bands used in the following experiments were fabricated at a length slightly less than the 2 mm between the hooks. The primary benefit of this approach is that the micro rubber bands are more easily assembled when they are assembled taut between the hooks. The extra stored energy at the point of assembly may also prove beneficial because the actuator does not need to do the work to store it. The tradeoffs of using stiff and compliant springs with pre-strain to store extra energy in the actuator are examined below.

For stiffer springs, the slope of the force/displacement curve is much steeper. As can be seen in Figure 3.14, a microrobot with force-limited actuators that can provide large

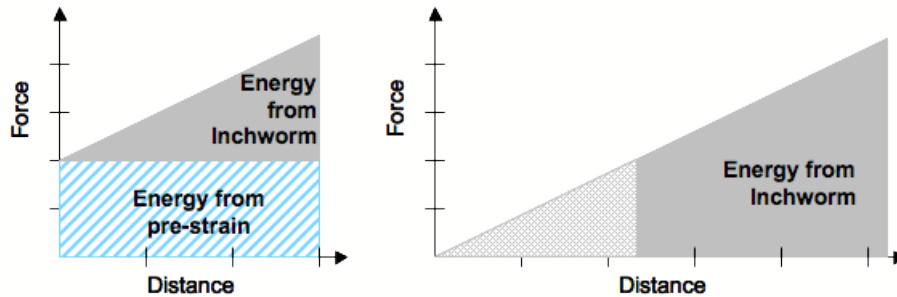


Figure 3.14: Effect of Fabricated Pre-strain on Energy Storage with Stiffer Springs. The graph at left shows a sample force/distance plot of a micro rubber band that has been pre-strained. At right, the same rubber band has been assembled with zero strain. Because the actuators are force limited, but can pull distances like  $F/k$ , the plot on the right in which the micro rubber band has been assembled with zero pre-strain stores more energy.

enough displacements to fully stretch the spring will lose energy when the spring material is pre-strained.

For more compliant springs, the slope of the force/displacement curve as seen in Figure 3.15 is much more shallow. If a method can be devised to stretch the micro rubber band many times the maximum actuator displacement when it is assembled, pre-strain can increase the amount of energy stored for a given actuator displacement. In the limit of a spring with a spring constant of 0 N/m, the force/displacement curve is flat and the amount of energy stored is  $Fx$  instead of  $0.5Fx$ . However, new assembly methods and structures will need to be realized before this approach is practical.

Micro rubber bands in both processes were fabricated with a pre-strain goal of 10% for assembly purposes. Due to variation inherent in the laser cutting process, laser cut micro rubber bands often varied approximately  $\pm 10\%$  from this goal.

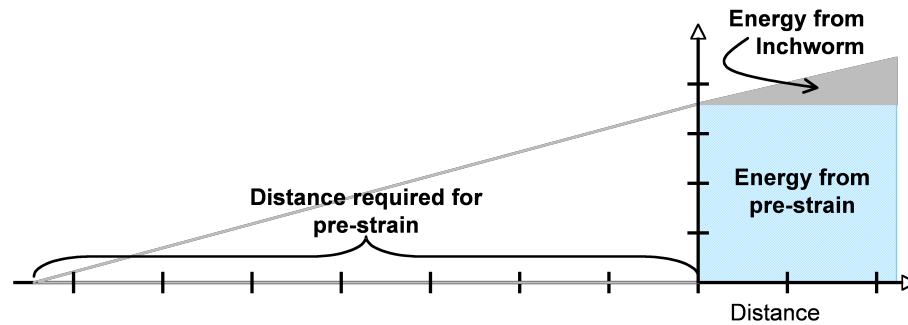


Figure 3.15: Effect of Fabricated Pre-strain on Energy Storage with More Compliant Springs. If the spring is more compliant and the micro rubber band can be stretched many times the actuator displacement when assembled, the actuator can store more energy for a given displacement with pre-strain.

### 3.3 Characterization and Results

Once fabricated and assembled, the micro rubber bands were characterized on their usefulness for energy storage and release. A force gauge was fabricated in the SOI process to measure the force-distance curves and energy storage efficiency of the silicone micro rubber bands (Figure 3.16). This force gauge was designed to withstand forces greater than 10 mN and measure the applied force with a resolution of 200  $\mu\text{N}$ . After breaking the tether holding the force gauge in place, a probe tip was used to pull the force gauge and rubber band while force and distance measurements were recorded. Data was collected for both the laser cut and molded rubber bands.

#### 3.3.1 Force-Displacement Curves

Laser cut micro rubber bands approximately 75  $\mu\text{m}$  wide, 50  $\mu\text{m}$  thick, and 1.1 mm in diameter were assembled with an approximate pre-strain of 16% and tested first. Results from two of the trials for distinct laser cut micro rubber bands are shown in Figure

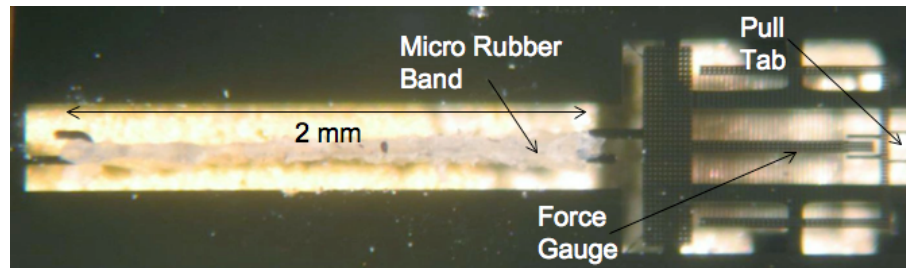


Figure 3.16: Force/Distance Test Structure for Characterizing Micro Rubber Bands. The assembled micro rubber band was stretched and released by using a probe tip to pull the connected force gauge.

3.17. In trial 1, the elastomer band was stretched 165% to store  $7.2 \mu\text{J}$  of energy and 81% of that energy was recovered upon slowly releasing the spring. In trial 2, the elastomer band was stretched 183% and stored  $8.2 \mu\text{J}$  of energy with an efficiency of 85%. Other trials showed up to  $11 \mu\text{J}$  stored and 93% recovered energy efficiency.

The same experiment was performed with molded rubber bands of approximately the same size  $100 \mu\text{m}$  wide,  $30 \mu\text{m}$  thick and  $1.2 \text{ mm}$  in diameter. These rubber bands were measured to have a pre-strain of approximately 11% and results from two trials are shown in Figure 3.18. In trial 1, the molded micro rubber band was stretched 200% to store  $10.4 \mu\text{J}$  of energy and 92% of that energy was recovered upon slowly releasing the spring. In trial 2, the rubber band was stretched to over 220% strain. In this trial,  $19.4 \mu\text{J}$  of energy was stored and  $16.5 \mu\text{J}$  was released for an efficiency of 85%. This  $16.5 \mu\text{J}$  of stored energy is equivalent to a  $16.5 \text{ cm}$  vertical jump in vacuum for a  $10 \text{ mg}$  microrobot.

### Elastomer Properties

The four trials outlined above resulted in calculated spring constants that differ substantially from each other. Both of the spring constants using the laser cut rubber

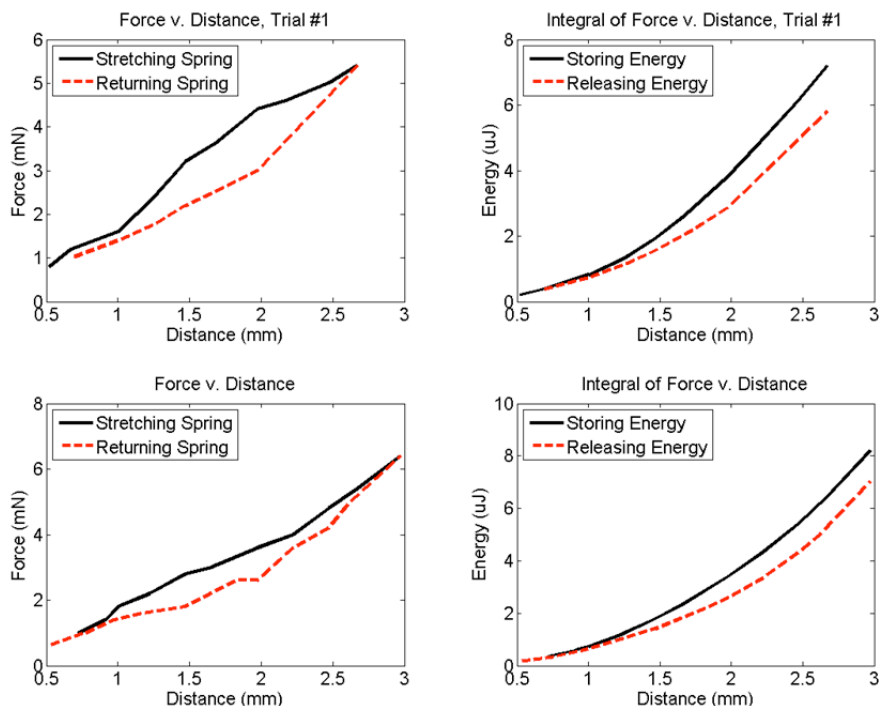


Figure 3.17: Force/Displacement Curves for Laser Cut Micro Rubber Bands.

bands were approximately 2.1 N/m. However, for the molded rubber bands, the calculated spring constant for the first trial was 1.6 N/m while the second trial was calculated at 2.5 N/m even though both rubber bands were fabricated in the same mold. It is assumed that the micro rubber band fabricated in trial 1 was damaged when removed from the mold resulting in the significantly lower spring constant. Occasionally, small tears showed up in the molded micro rubber bands when observed under a microscope. The same damage assumption holds true for the laser cut rubber bands, which were obviously damaged by the laser. Therefore, an approximate Young's Modulus for Sylgard <sup>®</sup> 186 may be calculated from the fourth trial using the equation:

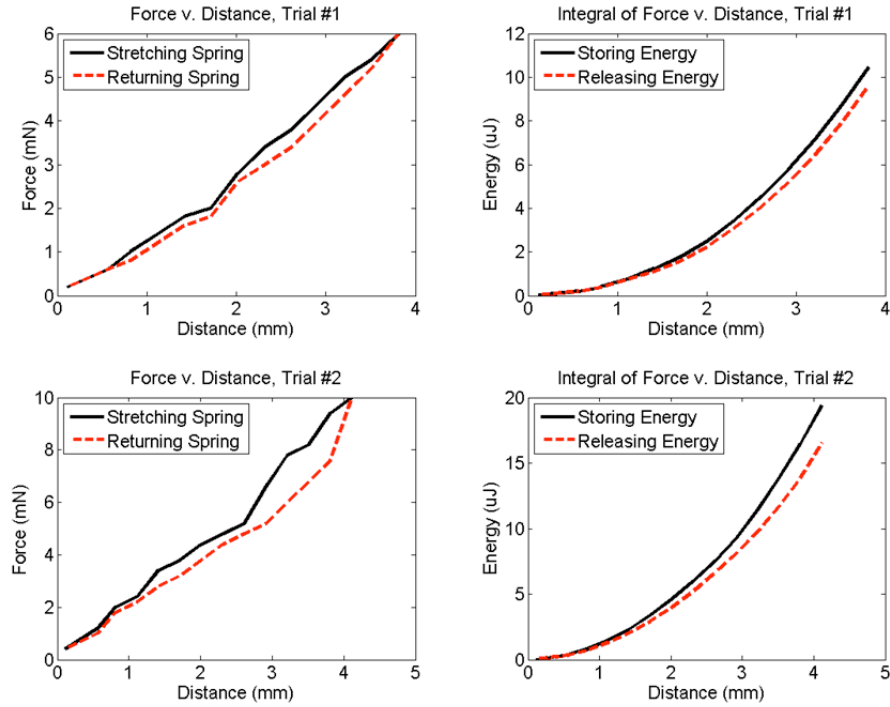


Figure 3.18: Force/Displacement Curves for Molded Micro Rubber Bands.

$$E = \frac{k}{2} \cdot \frac{L}{A} \quad (3.11)$$

where  $k$  is the calculated spring constant (2.5 N/m),  $L$  is the length of the micro rubber band (1.8 mm), and  $A$  is the cross-sectional area of the band ( $3000 \mu\text{m}^2$ ). This calculation results in a Young's Modulus of 750 kPa which is very similar to the 700 kPa calculated by Pelrine in [76].

### 3.3.2 Elongation at Break

In addition to measuring recovered energy efficiency and Young's Modulus of the micro rubber bands, it is also important to know when they break. The failure strain of

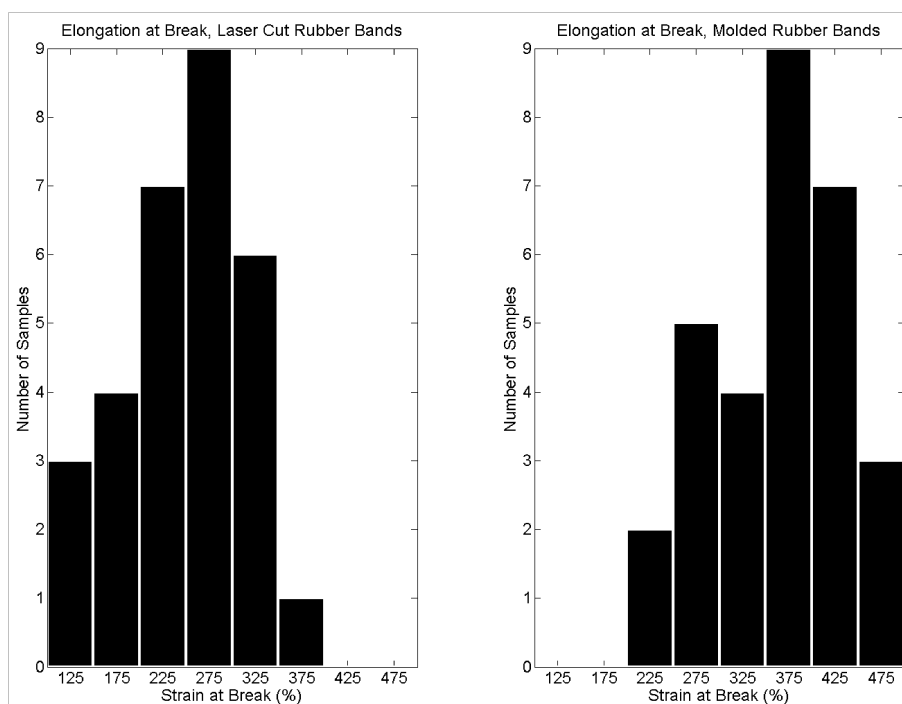


Figure 3.19: Elongation at Break Tests for Laser Cut and Molded Micro Rubber Bands. 30 micro rubber bands of each type were tested.

these bands was measured by stretching the rubber bands with tweezers until they snapped while measuring the distance stretched under a stereo inspection microscope (Figure 3.19). For the laser cut silicone, a mean failure strain was measured at approximately 250% over 30 trials with a standard deviation of 60%. The molded silicone fared significantly better with a mean failure strain of 350% over 30 trials and a standard deviation of 60%. The similar standard deviation in the molded rubber bands is probably due to the current method of removing the rubber bands from the mold with tweezers, which slightly damages them. However, they still demonstrate significantly higher performance than the rubber bands that were laser cut. Future advances in fabrication removal techniques will help make these micro rubber bands significantly more consistent.

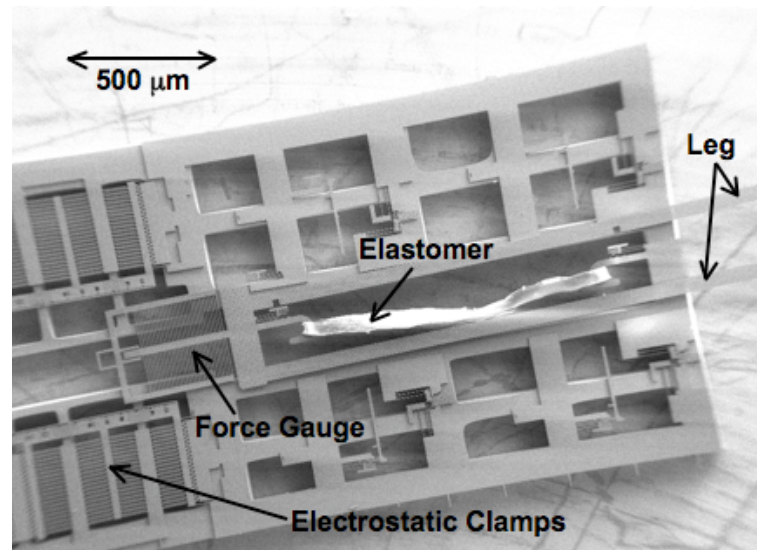


Figure 3.20: Test Structure for Quick Release of Energy from Energy Storage System. The micro rubber band is stretched with a probe tip and clamped in place before release. By shooting a projectile, a qualitative understanding of how energy is released quickly from this energy storage system can be attained.

### 3.3.3 Quick Release

To explore the effects of quickly releasing the stored energy as will be required in a high power application like jumping microrobots, a test structure was designed to shoot a projectile across a surface (Figure 3.20). This test structure consists of a micro rubber band attached to the body of the test structure on one side and a leg connected to a force gauge on the other end. In addition, electrostatic gap closing actuator (GCA) clamps are used to hold the leg in place before release. These clamps are designed to be normally-closed so that the clamps open by actuating away from the leg. The advantage of this method over electrostatically closing normally-open clamps is two-fold. Because the flexure force is linear with respect to displacement, the leg self-centers and equal force is provided on both sides of the leg. In addition, the test structure may also be moved and re-oriented while

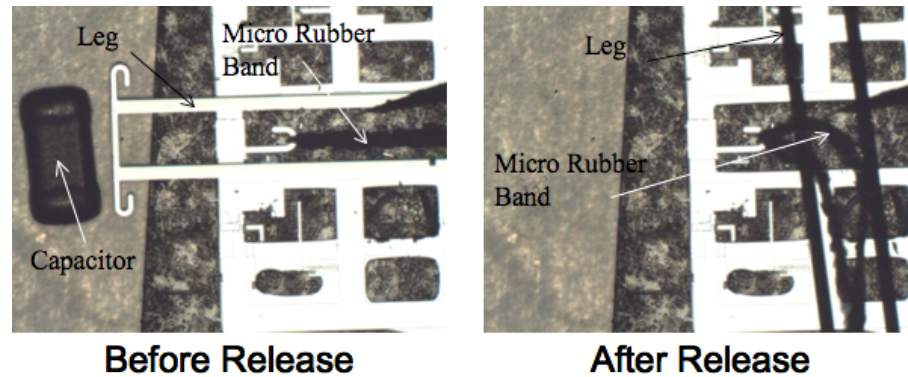


Figure 3.21: Before and After Frames from Quick Release Test Video. A surface mount capacitor was placed in front of the leg before electronically releasing the clamps holding the leg in place. This capacitor was shot 1.5 cm along a glass slide.

the clamps are held closed.

For testing, the test structure was held with double stick tape on a glass slide under a probe station and the leg was pulled back with a probe and clamped. An 0402-sized capacitor with a mass ( $m_{cap}$ ) of approximately 0.6 mg was then maneuvered in front of the leg (Figure 3.21). Finally, the clamps were actuated to release the leg. In the ideal case, the coefficient of friction between the capacitor and the glass ( $\mu_k$ ) along with the stopping distance of the capacitor ( $d_s$ ) can be used to calculate the amount of kinetic energy given to the capacitor when shot.

$$U_{cap} = \mu_k m_{cap} g d_s \quad (3.12)$$

Comparing  $U_{cap}$  to the energy originally stored in the micro rubber band, the efficiency of conversion from stored elastic energy to kinetic energy can be calculated.

Unfortunately, the capacitor tumbled instead of sliding directly along the glass slide due to the off-center impulse provided by the leg impacting the capacitor. The capacitor is only 350-400  $\mu\text{m}$  thick compared to the leg height of approximately 300  $\mu\text{m}$ . This tumbling

makes it difficult to extract any quantitative data on energy released from this test. While the total energy released is not quantified, a 15-fps video showed that the leg released its energy in less than a single video frame (66 ms) and the leg propelled the resistor 1.5 cm along the glass slide. Another failure mechanism was the leg popping out of plane as seen in the right half of Figure 3.21. In the future, assembled staples over the leg as demonstrated by Last should be able to fix this problem by preventing the leg from moving vertically out of plane [78]. Larger projectiles can also be used to prevent energy lost from tumbling.

## Chapter 4

# High Work Density Motors

While the energy storage component quickly releases energy for a jump, a motor is still required to stretch and store energy in the spring. As discussed in Chapter 2, the motor requirements include small size and mass, large forces of approximately 10 mN, large travel of around 5 mm, simple fabrication, and very low input power. In addition, these motors should be able to store energy in the micro rubber band at a speed allowing several jumps per minute. Motors with requirements similar to those used in this jumping microrobot could find use in cell phones [79], neural probes [18], and even in microrobots using other locomotion methods like walking [28].

A number of motor technologies with similar specifications have been designed and used in previous microrobots (Figures 4.1 and 4.2). Thermal actuators were used to provide high forces and large displacements for the walking microrobot in [23]. However, this robot was tethered to a power supply and it is unlikely that thermal actuators will satisfy the low power requirements for an autonomous microrobot. Piezoelectric actuators,

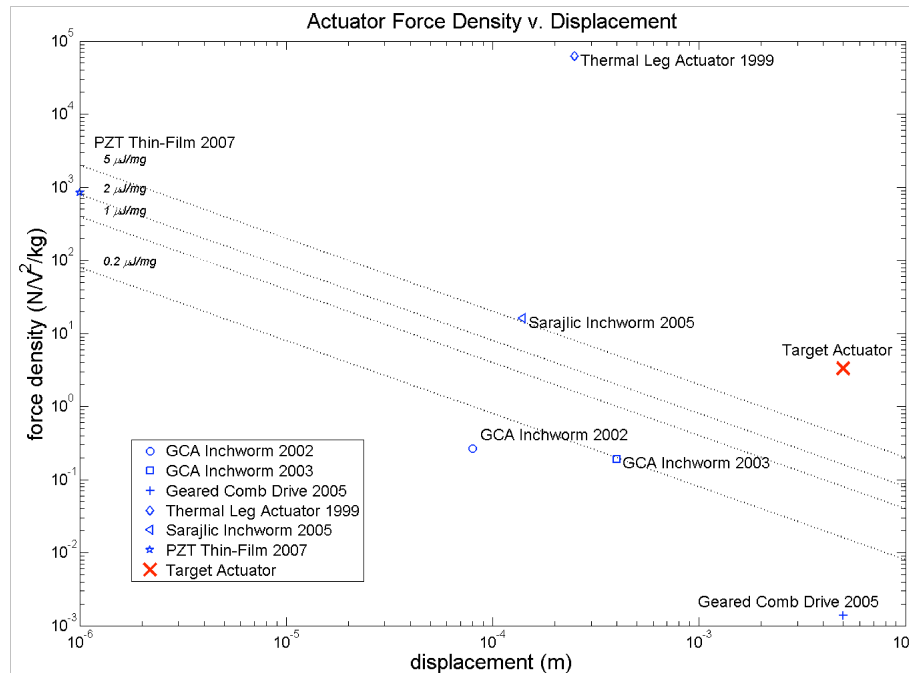


Figure 4.1: Actuator Force Density v. Displacement. The diagonal lines represent the target work per mass required from 5 mg actuators to store energy in the micro rubber bands. Actuator performance numbers are taken from [74, 80, 18, 23, 81, 82] although to calculate mass, estimates were occasionally used. If the actuator required a mechanical substrate to hold the motor pieces together or for additional actuation, motor thickness was automatically placed at 300  $\mu\text{m}$  similar to the motors in [80].

and especially thin-film piezoelectric actuators, are notoriously difficult to fabricate and integrate with other MEMS components. The micro flying insect described in Chapter 1 along with the microrobot proposed by Oldham in [82] both use Lead Zirconate Titanate (PZT) piezoelectric actuators. While the MFI actuators used bulk PZT too large for a 10 mg robot, the thin-film PZT described in [82] was demonstrated to provide forces of 7 mN at a 1  $\mu\text{m}$  throw in an area of 100  $\mu\text{m}$  by 500  $\mu\text{m}$  at 20 V. Piezoelectric materials like PZT provide high force densities and good efficiencies which may provide a future motor technology for microrobots once fabrication challenges are solved.

The small, cantilever-style microrobot in [24] was essentially a single electrostatic scratch drive actuator (SDA). Scratch drives generally provide high force densities and large displacements, but require an electrode that covers the entire length or area covered by the SDA. The resulting large parasitic capacitance often leads to poor efficiencies and higher power consumption. Electrostatic inchworm motors have also been used for microrobots. Inchworm motors take advantage of the high forces provided from electrostatic gap closing actuators (GCAs) and accumulate the GCA's small displacements into much larger displacements [28, 74, 22, 81]. Hollar designed the highest in-plane work density inchworm motors to date that provided a calculated  $400 \mu\text{N}$  of force and a displacement of  $400 \mu\text{m}$  [28] – each an order of magnitude below what is required for an autonomous jumping microrobot.

These motors along with other related ones are shown in the force density versus displacement graph in Figure 4.1. While both force density and motor travel are important for an autonomous jumping microrobot, the product of these two parameters is the most relevant. The mechanical work done by these motors will determine the amount of energy stored in the micro rubber bands from Chapter 3 and therefore, the height of the microrobot jumps. The diagonal lines in Figure 4.1 depict constant work densities. Force has been normalized by voltage squared since most of these actuators can provide higher forces with larger voltages.

The motor power densities are also important. Building a high work density motor for use in jumping microrobots comes with the implicit assumption that a power amplifier will be provided by the energy storage and quick release system described in Chapter 3. However, the motor still needs to be able to store this energy in the micro rubber bands

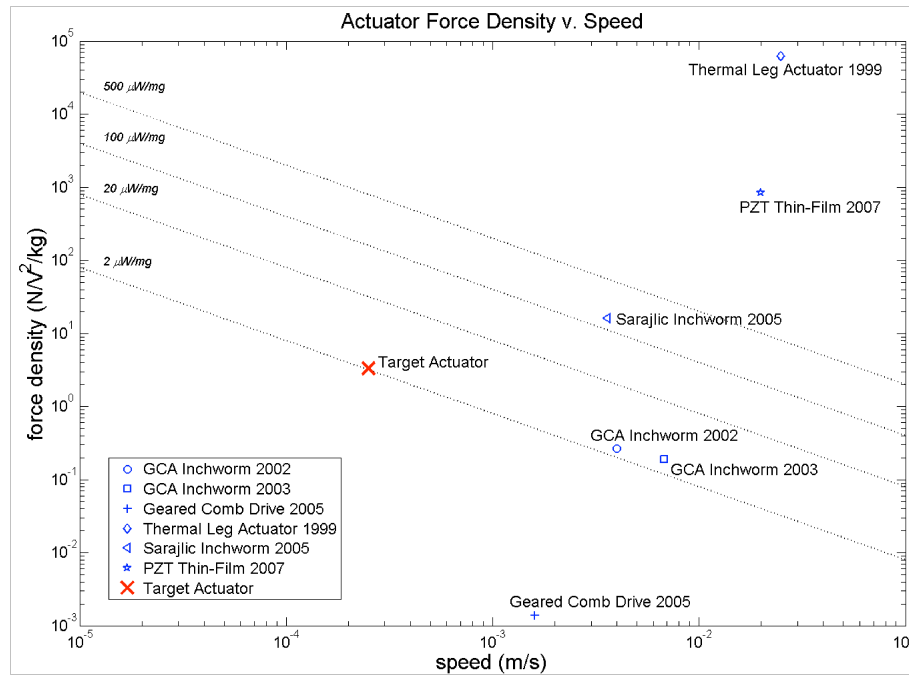


Figure 4.2: Actuator Force Density v. Velocity. Actuator performance numbers are taken from [74, 80, 18, 23, 81, 82] although to calculate mass and speed, estimates were occasionally used. If the actuator required a mechanical substrate to hold the motor pieces together or for additional actuation, motor thickness was automatically placed at  $300 \mu\text{m}$  similar to the motors in [80]. The diagonal lines represent the same power density lines provided in Figure 2.7.

relatively quickly. The target time to store the energy for a jump is 10s of seconds for a jump frequency of several jumps per minute. All of the actuators in Figure 4.2 have high enough power densities to satisfy this requirement. The diagonal lines in this figure represent the same power densities given in Figure 2.7. Sarajlic's inchworm motor provides very high power densities, but also requires large parasitic capacitances like the scratch drive and a more complex fabrication process.

Taking fabrication complexity and efficiency into account along with Figure 4.1, inchworm motors present a compelling choice for integration into an autonomous jumping

microrobot. However, motor travel and force densities demonstrated previously are still approximately an order of magnitude from the actuator targets in this dissertation. The following sections will detail design and fabrication improvements which make it possible to use electrostatic inchworm motors to store tens of microJoules for jumps.

## 4.1 Design

To design an improved electrostatic inchworm motor, the limitations of previous approaches must first be understood. Previous inchworm motors were designed and operated as shown in Figure 4.3. Each inchworm motor consists of four separate gap closing actuator arrays – two drive arrays moving from right to left and two clutch arrays used to engage the drive actuators with the shuttle. In normal operation, the clutch actuator on the left side first engages the shuttle. The left drive actuator is then used to move the shuttle forward a set distance. In step 3, the clutch on the right side holds the shuttle in place. Finally the right drive actuator moves the shuttle forward while the clutch and drive actuator on the left side release and reset. The full inchworm cycle repeats to achieve large displacements limited only by the springs connected to the shuttle.

The electrostatic inchworm motor provides relatively high forces and large displacements, and it does so in a relatively simple fabrication process. The motor designed by Yeh in [74] was fabricated in a single-mask silicon-on-insulator (SOI) process. This process is even simpler than the silicon chip fabrication described in Section 3.2.1 because it does not require a backside etch. Electrostatic inchworm motors also require very low input powers at moderate voltages. Previously designed motors have been driven at 33 V or 50

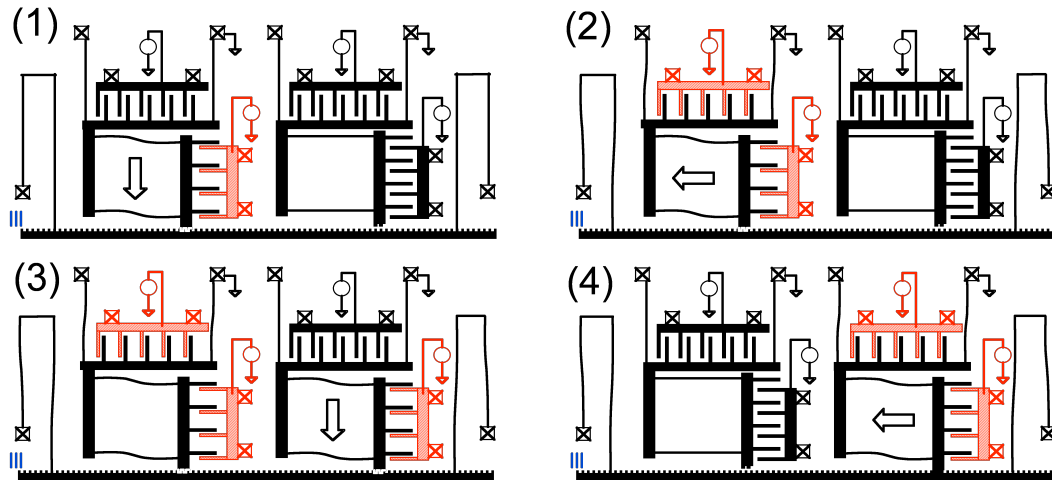


Figure 4.3: Inchworm Motor Operation.

Although the voltage could certainly go higher. Finally, inchworm motors demonstrated previously are relatively efficient at 8% and can be made more efficient by reducing parasitic capacitance and using charge-controlled driving electronics instead of voltage-controlled drivers.

However, as stated previously and shown in Figure 4.1, previous GCA inchworm motors provide relatively low displacements and forces compared to what is needed for an autonomous jumping microrobot. Springs have traditionally been used to keep the shuttle in the motor's plane of operation and provide the recoil force to reset the motor, but these springs limit the possible motor travel. Gear teeth on the shuttle have helped increase the coefficient of friction between the clutch and the shuttle, but these teeth limit the force output from the drive actuator. Electrostatic inchworm motors meet the design requirements for low power at moderate voltage, simple fabrication, and relative efficiency, but lack the motor travel and force density required. The following sections will detail

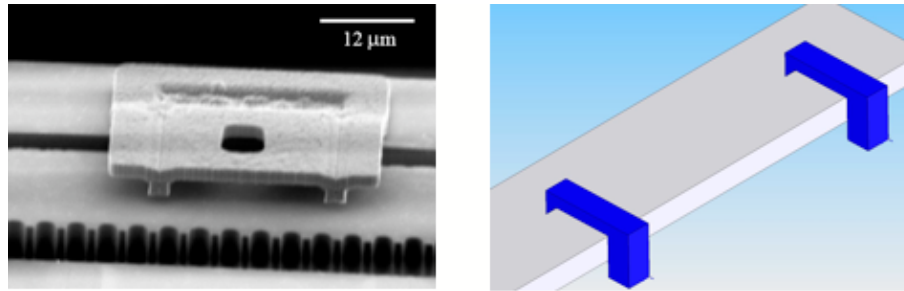


Figure 4.4: Assembled Staples to Increase Motor Travel. The polysilicon flaps on the left were fabricated in a relatively complex process, but did a good job of keeping the motor shuttle in the motor’s plane of operation. To maintain the same design principles with a simpler process, post-process assembly will be used to assemble staples to constrain the motion of the motor shuttle.

a new inchworm motor design intended to provide significantly higher force densities and displacements.

#### 4.1.1 Motor Travel

As seen in Figure 4.3, springs have traditionally been used to keep the shuttle in the motor’s plane of operation. The springs also provide the restoring force to reset the motor after it has been stepped a given distance. In most cases, a simple folded flexure is used to allow for larger (10s or 100s of  $\mu\text{m}$ ) travel distances, but millimeter-order displacements are required to stretch the micro rubber band in Chapter 3. In [28], Hollar used polysilicon flaps along with a serpentine silicon spring on one end of the shuttle to extend inchworm motor operation to 400  $\mu\text{m}$  displacement. Unfortunately, the polysilicon flaps also required a significantly more complex fabrication process that is described in [80].

In order to maintain the simple fabrication requirements of an inchworm motor, post-process assembly as demonstrated in [78] can be used to provide a similar flap-like

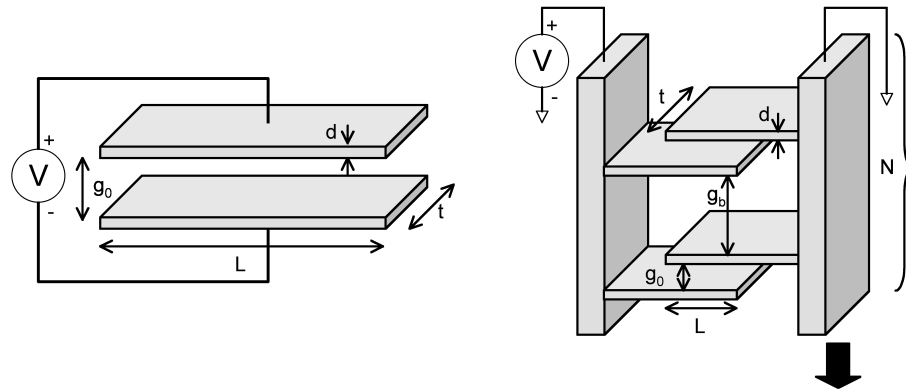


Figure 4.5: Cell Size for a Gap Closing Actuator.

system. Figure 4.4 shows both the previous polysilicon flap design as well as a drawing of what an assembled staple may look like. In addition, the micro rubber band will provide motor recoil for resetting the motor. These relatively simple improvements to the motor design will increase motor displacement to the full length of the shuttle.

#### 4.1.2 Force Density

Now that the motor has been designed to travel many millimeters, it needs to provide higher forces to store energy in the micro rubber band. More importantly, force density should be increased to maintain high forces with a low motor mass. Previous inchworm motor designs have attempted to optimize for force density based on etch aspect ratio, lithography limits, and cell spacing from one gap to another shown in Figure 4.5 [22, 83].

However, previous force optimizations focused on areal force density (force per area), and this design approach will focus on mass force density (force per mass) instead.

The focus on areal force density is due in large part to the fact that motors are fabricated in the device layer of an SOI wafer, and therefore have an additional substrate component to mechanically connect, but electrically isolate each piece of the inchworm motor. Theoretically, this substrate can be quite thin, but in practice due to handling, the motor substrates are generally 300  $\mu\text{m}$  thick or larger. Assuming that the number of fingers,  $N$ , is large, the mass force density for a drive actuator in the inchworm motor can be calculated as shown below where  $\epsilon$  is the permittivity of the gap material (usually air),  $t$  is the gap thickness,  $g_0$  is the gap over which the motor is actuated,  $g_b$  is the back gap,  $d$  is the plate thickness,  $t_{sub}$  is the substrate thickness, and  $\rho$  is the average density of the motor material.

$$FD_{mass} = \frac{F}{m} = \frac{\epsilon V^2 t (g_0^{-2} - g_b^{-2})}{2dt\rho + (2d + g_0 + g_b) t_{sub}\rho} \quad (4.1)$$

Previous work has resulted in force densities of approximately 0.2  $\mu\text{N}/\text{mg}/\text{V}^2$  assuming a 300  $\mu\text{m}$  thick substrate layer and an average density of 1  $\text{mg}/\text{mm}^3$ . At 50 V, this is equivalent to 0.5  $\text{mN}/\text{mg}$ .

As seen in Equation 4.1, there are several approaches to improve force density. First, and perhaps one of the most noticeable is to remove the mass of the substrate. If the motor substrate is 300  $\mu\text{m}$  thick compared to a motor thickness of 30  $\mu\text{m}$ , a great deal of mass is being added to the motor which provides no additional force. Previous designs have removed large chunks of this substrate but a lot still remains. If this substrate can be removed entirely, force density increases by a factor of 10 or more.

In addition, as seen in Figure 4.3, there are two drive actuators required to provide the force which one drive actuator alone can provide. This is due to a combination of factors including lithographic limitations for the inchworm motor teeth among others. For high

force motors where the drive actuator is large, removing one of these GCA arrays could have a large impact on force density. Finally, Equation 4.1 shows a square dependence on the initial gap  $g_0$ . Previous inchworm motors were limited on the size of the initial gap by lithographic limits and allowable etch aspect ratios. If the initial gap could be decreased by a factor of 3, the overall force density would increase another order of magnitude.

Other factors in Equation 4.1 can also increase force density. Voltage obviously has a large effect – force output from the motor increases an order of magnitude if voltage is increased  $3x$ . Of course, voltage is heavily dependent on power supply design and will therefore be limited by other design choices made for the robot as a system. Changing the dielectric material between the gaps from air to something like a soft polymer with a high dielectric constant and low Young's modulus can also potentially increase force density. The system tradeoffs include fairly radical fabrication changes and a slower motor with lower power density. Finally, lowering the average material density will increase force density, but would also require new materials and fabrication techniques. Voltage, dielectric material, and material density is not varied in this motor design to maintain the robot design requirements of a simple power supply, simple fabrication, and reasonable motor speeds.

Instead, the three design changes described below are used to increase force density in electrostatic inchworm motors without sacrificing larger robot design requirements. First, a transmission, or pre-biasing structure, will be used to reduce initial gaps beyond what is possible lithographically. Second, the teeth will be removed from the inchworm motor shuttle to allow for variable step sizes and remove the necessity for more than one drive actuator. Third, low stress silicon nitride will be included in the fabrication process to

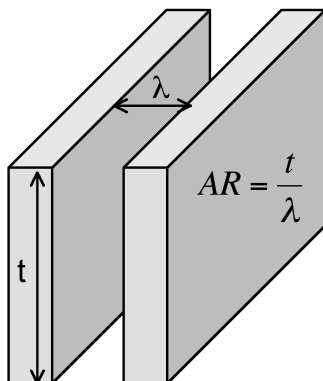


Figure 4.6: Aspect Ratio and Lithographic Limitations in GCA Actuators.

mechanically connect the motor pieces without a substrate and to provide smaller final gaps by integrating gap stops in the fingers to prevent them from shorting out.

### Transmission

The first step to improve the force density of electrostatic inchworm motors is to reduce the initial gap in the drive actuator. The force output from the drive GCA is dependent on the initial gap as defined below where  $L$  is the length of the gap, and  $N$  is the total number of gaps as pictured in Figure 4.5.

$$F_{gca} = \frac{1}{2} \frac{N \epsilon_0 V^2 L t}{g_0^2} \quad (4.2)$$

This initial gap is dependent on a number of fabrication parameters. Primary among these is the aspect ratio  $AR$  available in the deep reactive ion etch step used to define the gaps and the lithographic linewidth  $\lambda$  (Figure 4.6). If the device layer thickness  $t$  is too thick, aspect ratio limitations will make the gaps in the inchworm motor wider than they need to be. If the device layer is too thin, the force density suffers due to limited actuation area  $Lt$ .

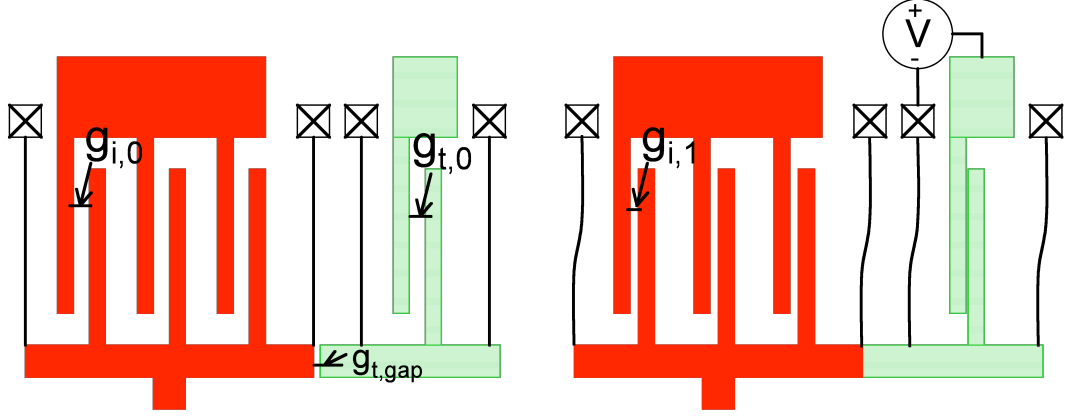


Figure 4.7: Pre-Biasing Transmission Design.

The pre-biasing transmission removes the initial gap's dependence on both aspect ratio and lithographic linewidth limits as shown in Figure 4.7. An additional transmission actuator is used to preset the primary drive actuator to a smaller initial gap. The transmission actuator can utilize a significantly smaller area than the drive actuator since it only needs to overcome the restoring force from the drive actuator springs.

$$F_{transmission} = \frac{1}{2} \frac{N_t \epsilon_0 V^2 L t}{g_{t,f}^2} > k_{drive} (g_{i,0} - g_{i,1}) = F_{drivespring} \quad (4.3)$$

$N_t$  is the number of gaps in the transmission actuator,  $g_{i,0}$  is the initial gap in the drive actuator before the transmission actuator is engaged,  $g_{i,1}$  is the initial gap in the drive actuator after the transmission has been engaged,  $k_{drive}$  is the spring constant for the drive actuator springs, and  $g_{t,f}$  is the final gap in the transmission actuator.

Drive actuator springs typically have a spring constant on the order of 10 N/m to reduce pull-in voltage which implies that very low forces will be required from the transmission actuator. The transmission actuator size will therefore be dependent on the pull-in

voltage available to engage the transmission as well as the change in initial gap width  $g_{i,0} - g_{i,1}$ , the gap between the transmission and drive actuators  $g_t$ , and the final gap in the transmission actuator  $g_f$ .

$$A_{transmission} = \frac{8}{27} \frac{k_t (g_{i,0} + g_t - g_{i,1} + g_f)}{\epsilon_0 V_{pi}^2} \quad (4.4)$$

Given a change in the initial drive actuator gap  $g_{i,0} - g_{i,1} = 2\mu m$ ,  $g_t = 2\mu m$ ,  $g_f = 2\mu m$ , and  $V_{pi} = 50V$ , the transmission actuation area is only  $0.029 \text{ mm}^2$ . Even if the change in the initial drive actuator gap is  $10 \mu m$ , the transmission actuation area is only  $0.37 \text{ mm}^2$ . These numbers are insignificant in comparison to a  $10 \text{ mN}$  drive actuation area of  $23 \text{ mm}^2$  with an initial gap of  $5 \mu m$  and a voltage of  $50 \text{ V}$ .

This tiny additional actuator can increase the force or reduce the amount of actuation area required to provide a fixed force. The force improvement will be:

$$\frac{F_{high}}{F_{low}} = \left( \frac{g_{i,0}}{g_{i,1}} \right)^2 \quad (4.5)$$

If the initial gap in this drive actuator is reduced from  $5 \mu m$  to  $3 \mu m$ , the force would increase over 250% or alternately, the area would decrease to approximately  $8.1 \text{ mm}^2$  for a  $10 \text{ mN}$  actuator. Including the size of the transmission actuator, this leads to an approximately  $3x$  decrease in actuation area. These numbers improve if a thicker device layer is used resulting in a much larger  $g_{i,0}$ . If  $g_{i,0}$  starts at  $13 \mu m$  and reduces to  $3 \mu m$  with the transmission actuator, total actuation area for  $10 \text{ mN}$  reduces  $18x$ .

In addition to increasing force density, a pre-biasing actuator like this one has a number of benefits. The same voltage level used to engage the drive actuator can be used to engage the transmission actuator. This is in contrast to previous pre-biasing structures used

to allow an inchworm motor to operate in reverse which required negative voltages that are difficult to provide in the microrobot electronics [80]. In addition, the transmission actuator does not add to the inchworm cycle sequence and therefore, does not make the motor any slower. The transmission actuator can be engaged when the motor is first switched on to always provide higher forces out of the motor.

Perhaps more interestingly however, the transmission actuator can be used to provide both a low gear and a high gear for the motor. In the high gear, the transmission actuator is not engaged and the motor provides high speeds with low force. The high speeds are due to a larger step size defined by

$$\Delta_{high} = g_{i,0} - g_f \quad (4.6)$$

$$F_{high} = \frac{1}{2} \frac{N\epsilon_0 V^2 L t}{g_{i,0}^2} \quad (4.7)$$

In low gear, the motor provides a higher force when the transmission is engaged, but smaller step sizes result in lower speeds.

$$\Delta_{low} = g_{i,1} - g_f \quad (4.8)$$

$$F_{low} = \frac{1}{2} \frac{N\epsilon_0 V^2 L t}{g_{i,1}^2} \quad (4.9)$$

This is particularly advantageous in a system where the actuator is pulling a linear load like the micro rubber band. The motor can operate in high gear early on and switch to low gear when higher forces are necessary.

### **Friction Clutch**

The second major improvement to electrostatic inchworm motors removes the gear teeth from the inchworm motor shuttle. Previous inchworm motor designs used gear teeth

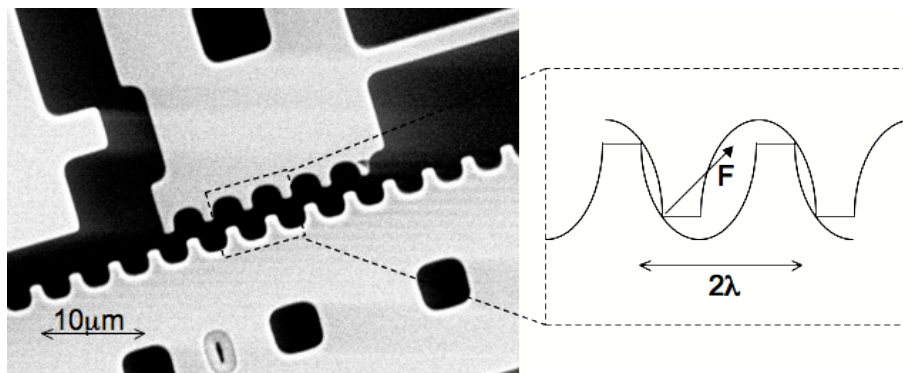


Figure 4.8: Gear Teeth on Inchworm Motor Shuttle.

to prevent the clutch actuator from slipping against the shuttle (Figure 4.8). While clutch slipping continues to be a problem, these teeth led to numerous design and fabrication consequences for the inchworm motors as discussed in [80]. Fabricating square gear teeth can be difficult when operating close to the lithographic and aspect ratio limits as seen in Figure 4.8 and previous work has attempted to deal with a number of these fabrication issues [83].

However, gear teeth also have design repercussions that affect force density. First, the smallest tooth pitch that can be used is two times the lithographic linewidth  $2\lambda$ . Therefore, the inchworm motor needs to displace  $2\lambda$  during a full cycle. There are two ways that an inchworm motor can accomplish this  $2\lambda$  displacement. In the first case, the initial gap in the drive actuator is set to  $2\lambda + g_f$ , where  $g_f$  is the final gap in the drive actuator that prevents the gap fingers from shorting out. In the case where  $\lambda = 2\mu m$  and  $g_f = 2\mu m$ , this implies an initial gap of  $6\mu m$ . For a 10 mN motor, a  $6\mu m$  initial gap requires an actuation area of  $33\text{ mm}^2$  roughly translating to a mass of 6.9 mg (including the substrate). The

second approach uses two drive actuators as seen in Figure 4.3 which each displace  $\lambda$  with an initial gap of  $\lambda + g_f$ . Using the same numbers for  $\lambda$  and  $g_f$ , a 10 mN drive actuator requires  $29 \text{ mm}^2$  actuation area with a mass of approximately 6.1 mg. These numbers do not include the clutch mass or any additional mass added from structural support requirements for the rest of the motor.

While the pre-biasing transmission actuator can be used to reduce the initial gap in the inchworm motor beyond what is possible through fabrication, if gear teeth continue to be used force density numbers will not dramatically improve since it is never possible to make the initial gap smaller than  $\lambda + g_f$ . In addition, using gear teeth negates the advantage of having multiple gears available to the robot while stretching the micro rubber band since multiple-step sizes will not be permissible with the fixed step size imposed by the gear teeth. Finally, it would be incredibly advantageous to be able to use only one drive actuator with the smaller initial gap.

Hence, the new inchworm motor design will use a friction-based clutch. The new inchworm motor uses only a single drive actuator and its operation is shown in Figure 4.9. In this new configuration, the inchworm motor is two-sided; it grips the shuttle from both sides. There are still two clutch actuators – a drive clutch attached to the drive actuator to engage or disengage it from the shuttle, and a static clutch to hold the shuttle in place while the drive actuator resets. In step 1, the static clutch disengages from the shuttle so that the drive actuator can move the shuttle forward as shown in step 2. In step 3, the static clutch closes again to hold the shuttle in place while the drive actuator resets as shown in steps 4 and 5.

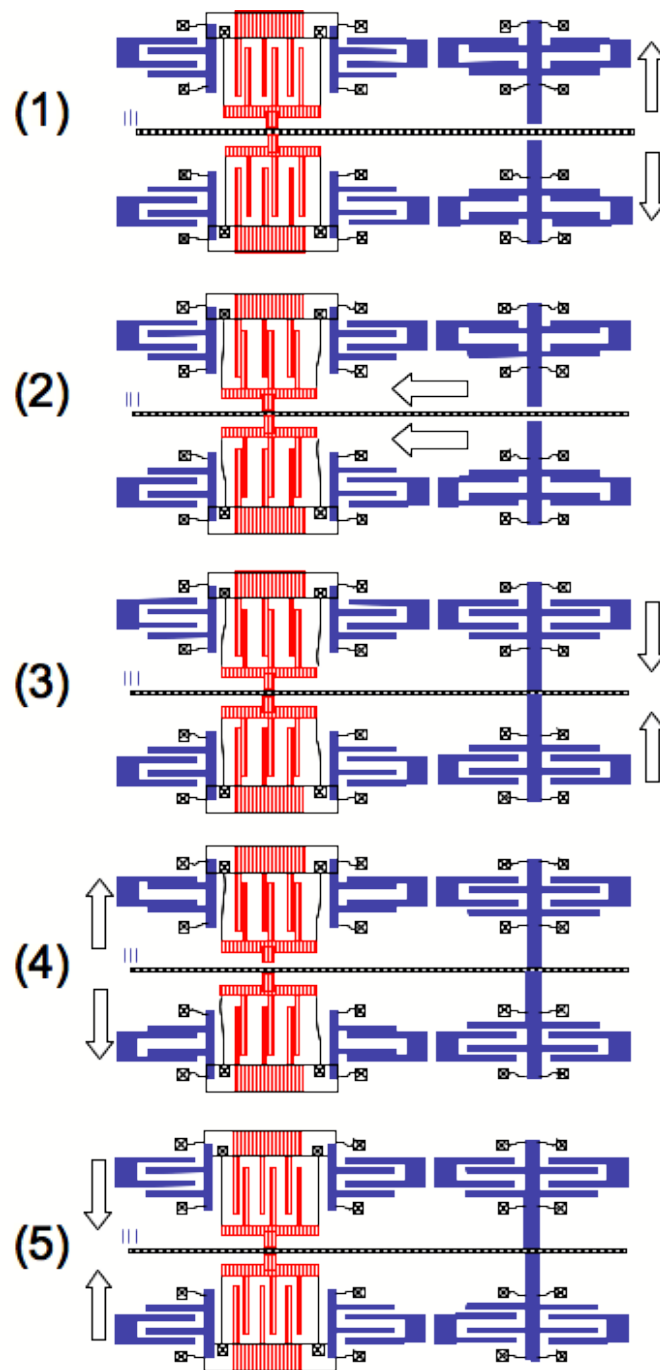


Figure 4.9: New Inchworm Motor Operation with Friction Clutch. In step 1, the static clutch releases the shuttle. In steps 2 and 3, the drive actuator moves the shuttle forward and the static clutch holds the shuttle in this new position. In steps 4 and 5, the drive actuator resets itself for the next cycle.

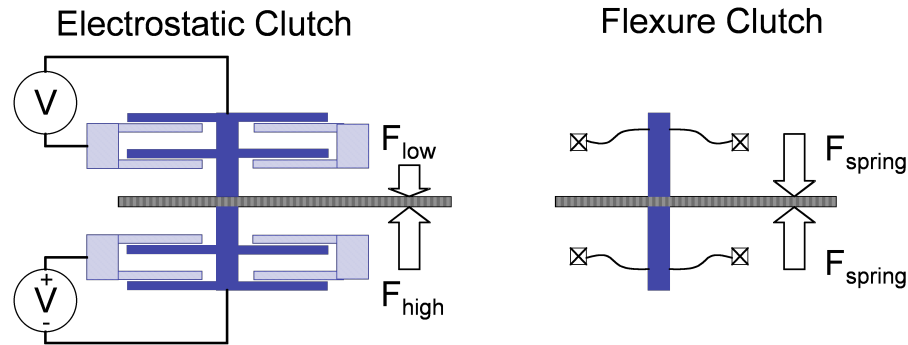


Figure 4.10: Electrostatic v. Flexure Clutch Forces.

The two-sided motor design is another new design feature for inchworm motors. Previous motors pushed the shuttle against a fixed silicon back stop introducing extra friction opposing forward motion [83]. Because the motor is reliant on the friction interface between the clutch and shuttle, the normal force provided by the clutch should be equivalent from both sides. If the clutch engages the shuttle with an electrostatic force, small process variations will lead to an unstable equilibrium point when the two clutches grip the shuttle due to the nonlinear dependence on gap distance. This results in two different forces from each clutch,  $F_{high}$  and  $F_{low}$ , where  $F_{high}$  comes from one of the clutches pulled all of the way in. The resulting normal force used to determine the frictional force between the clutch and shuttle will simply be  $F_{low}$ .

To address this issue, a linear flexural force is used instead to provide a stable equilibrium point and the shuttle self-centers from equivalent forces on both sides (Figure 4.10). The clutch actuators are designed to be normally closed and open outwards with an electrostatic force. The clutch springs are designed to be as stiff as possible with the limit that they still pull-in at the given supply voltage.

The shuttle gear teeth do have the advantage of increasing the coefficient of friction between the clutch and the shuttle. By removing them, the inchworm motor is reliant on the natural coefficient of friction between the two deep reactive ion etched surfaces. Timpe measured the coefficient of friction between polysilicon reactive ion etched sidewalls to be approximately 0.5 [84]. Due to the lower coefficient of friction that results from a toothless interface, larger clutch actuators will need to be designed which will limit some of the force density gains. In addition, half of the force from each clutch is used to counteract the other clutch. If each clutch provides force  $F_{clutch}$ , a total  $F_{clutch}$  is used to squeeze the shuttle.

Table 4.1: Clutch Area Based on Coefficient of Friction

Coefficient of Friction	Flexure Force Required for each Half Clutch (mN)	Total Actuation Area for Static and Drive Clutches (mm <sup>2</sup> )
0.25	40	8.5
0.5	20	4.3
0.75	13	2.9
1.0	10	2.1
teeth <sup>a</sup>	6.3	4.6

<sup>a</sup> Motor in [28] scaled for 10 mN.

Table 4.1.2 lists sample clutch actuation areas for varying coefficients of friction assuming that the clutch springs are displaced  $2.5 \mu\text{m}$  when gripping the shuttle, the clutch initial gap is  $2 \mu\text{m}$ , and the supply voltage is 50 V. The initial gap in the clutch actuator can be made smaller than possible with the lithographic limit of the process using a method similar to the pre-biasing transmission actuator in the previous section. In this case, the clutch actuator is pre-biased by presetting the inchworm motor shuttle by hand as shown in Figure 4.11. While the clutch actuators in [28] are most likely designed much larger

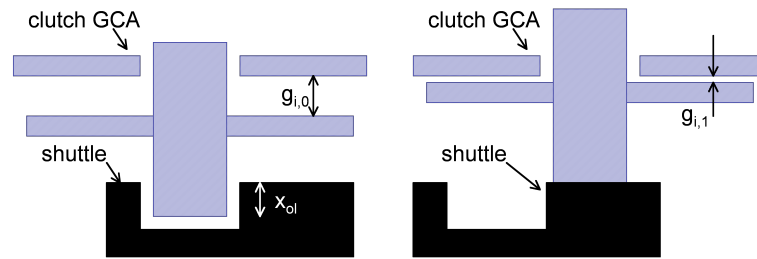


Figure 4.11: Friction Clutch Preset.

than necessary, the required actuation area for both clutches if scaled linearly with force is approximately the same as a friction clutch system with a coefficient of friction of 0.5. It should be noted that this coefficient of friction can also be increased with various coatings or surface treatments [85]. Assuming a coefficient of friction of 0.5 and a  $2 \mu\text{m}$  initial gap provided by the transmission actuator in the previous section, the total motor actuation area is approximately  $7.9 \text{ mm}^2$  with these two improvements. If clutch forces are scaled with drive forces, this is only 1/6th the area of a motor with an initial gap of  $5 \mu\text{m}$  using the original inchworm motor design. As seen in the previous section, this improvement gets even better as the device layer becomes larger.

### Low-Stress Silicon Nitride

The final inchworm motor design change to increase force density is the addition of low-stress silicon nitride to the fabrication process which will allow greater flexibility in motor design. Low-stress silicon nitride (henceforth simply silicon nitride) has been used previously in MEMS devices and circuits as an isolation material on an SOI wafer. In fact, Bellew designed the solar cells discussed later in Chapter 5 to use silicon nitride to isolate

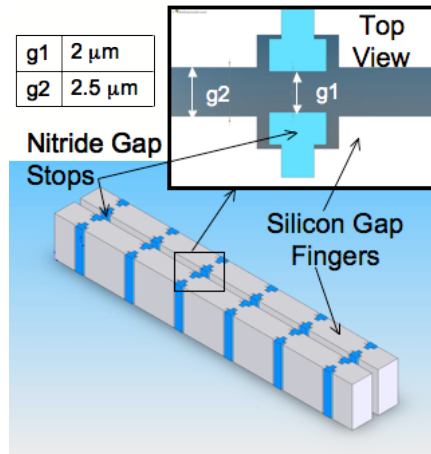


Figure 4.12: Integrated Nitride Gap Stops.

the separate cells and stack them in series to reach high voltages [86]. Silicon nitride has also been used to mechanically connect, yet electrically isolate components in MEMS actuators and has been used to coat the sidewalls of gap closing actuators to prevent shorting [87, 81].

Silicon nitride offers two important advantages for electrostatic inchworm motors. Previous motors used short, 100-150  $\mu\text{m}$  long gap fingers with a final gap  $g_f$  of 2  $\mu\text{m}$  due to concerns about the gap fingers shorting together. Silicon nitride gap stops can be integrated into the silicon gap fingers to define a much smaller final gap as shown in Figure 4.12. Defining a small final gap makes larger step sizes and faster speeds possible even when the transmission actuator is engaged. In addition, the friction clutch force depends heavily on the final gap in the clutch actuators, and smaller is better. Some of the practical fabrication issues that stem from defining this final gap distance are discussed further in Section 4.2.

A second advantage is the removal of the previously required substrate layer. As

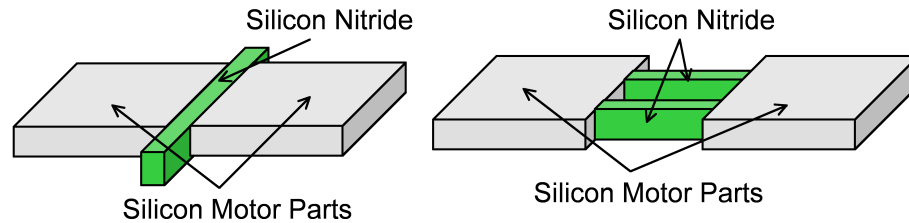


Figure 4.13: Two Approaches to Mechanical Connection with Electrical Isolation.

discussed above, inchworm motors previously required a substrate to mechanically connect, yet electrically isolate parts of the motor. As seen in Figure 4.13, silicon nitride beams can be used to perform this same feat with drastic reductions in mass. Parasitic capacitances can be kept to a minimum by using nitride beams in a truss formation to push the silicon blocks further apart instead of a simple beam holding the two silicon components together. By removing the  $300\ \mu\text{m}$  thick substrate layer, a motor which requires an area of  $10\ \text{mm}^2$  in a  $50\ \mu\text{m}$  thick device layer can achieve a mass savings of approximately 85%.

Overall, adding silicon nitride to the motor design arsenal creates more flexibility in designing inchworm motors. Longer gap fingers can be used to remove much of the suspension support area required previously. Silicon nitride offers greater flexibility in how motor wiring is routed. Previously, if the drive actuator was laid out so that it directly engaged the shuttle instead of engaging through the clutch actuator, the drive actuator bond pad would be inaccessible outside of the motor area. Silicon nitride can also be used to create bumps on the bottom of the SOI device layer to help prevent stiction on moving silicon parts. This process will be described in more detail in Section 4.2.1. While silicon nitride does not increase the force available from the inchworm motor, it greatly reduces

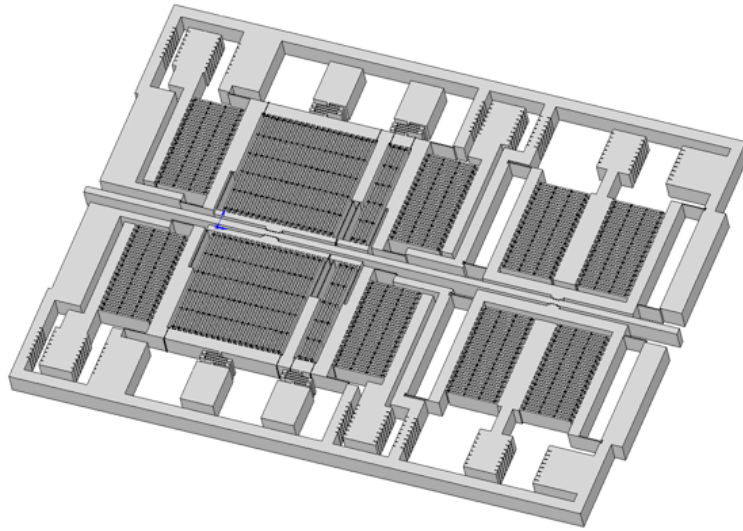


Figure 4.14: New Inchworm Motor Layout.

the mass, helps retain moderate motor speeds even with smaller initial gaps, and provides greater flexibility in motor design.

### 4.1.3 Motor Design Summary

The final inchworm motor design is shown in the Solidworks<sup>TM</sup> layout in Figure 4.14. It should be noted that this picture does not include the staples described in Section 4.1.1 although these will eventually be included in the final motor design. Using the three force density improvements mentioned above, the total force density over previous designs can be improved  $37x$ . The next sections will describe the fabrication and testing results from these motors.

Table 4.2: New Inchworm Motor Design Summary.

	Old Design	New Design	Innovation
$g_0$ ( $\mu\text{m}$ )	5	2	Transmission + Friction Clutch
$t_{sub}$ ( $\mu\text{m}$ )	300	0	Silicon Nitride
Num Drive Actuators	2	1	Friction Clutch
$\text{Area}_{drive}$ ( $\text{mm}^2$ )	45.2	3.6	Transmission + Friction Clutch
$\text{Area}_{clutches}$ ( $\text{mm}^2$ )	4.6	4.3	Silicon Nitride + Friction Clutch
$\text{Area}_{total}$ ( $\text{mm}^2$ )	49.8	7.9	All 3
Cell Width ( $\mu\text{m}$ )	34	23	Transmission
$\text{Mass}_{total}$ (mg)	6.7	0.18	All 3
Force Density (mN/mg)	1.5	55	All 3

## 4.2 Fabrication

While simple inchworm motors can be fabricated in a single-mask SOI process, the improved inchworm motors add an additional mask to fabricate low-stress silicon nitride beams. This new process has been designated the “Froghopper Process” in honor of the jumping champion in the insect world. In addition to the processing itself, there are a number of guidelines laid out in this section for the practical design and layout of the motor given process lateral etch and mask alignment.

### 4.2.1 Froghopper Process

The primary goals of the Froghopper process are to fabricate the motors designed in Section 4.1 and to integrate the energy storage system in Chapter 3. For this reason, a process similar to the silicon process described in Section 3.2.1 has been chosen. The only addition is an extra mask used to define the trenches which will be refilled with silicon nitride. For simplicity in motor fabrication and testing, the final backside etch used in

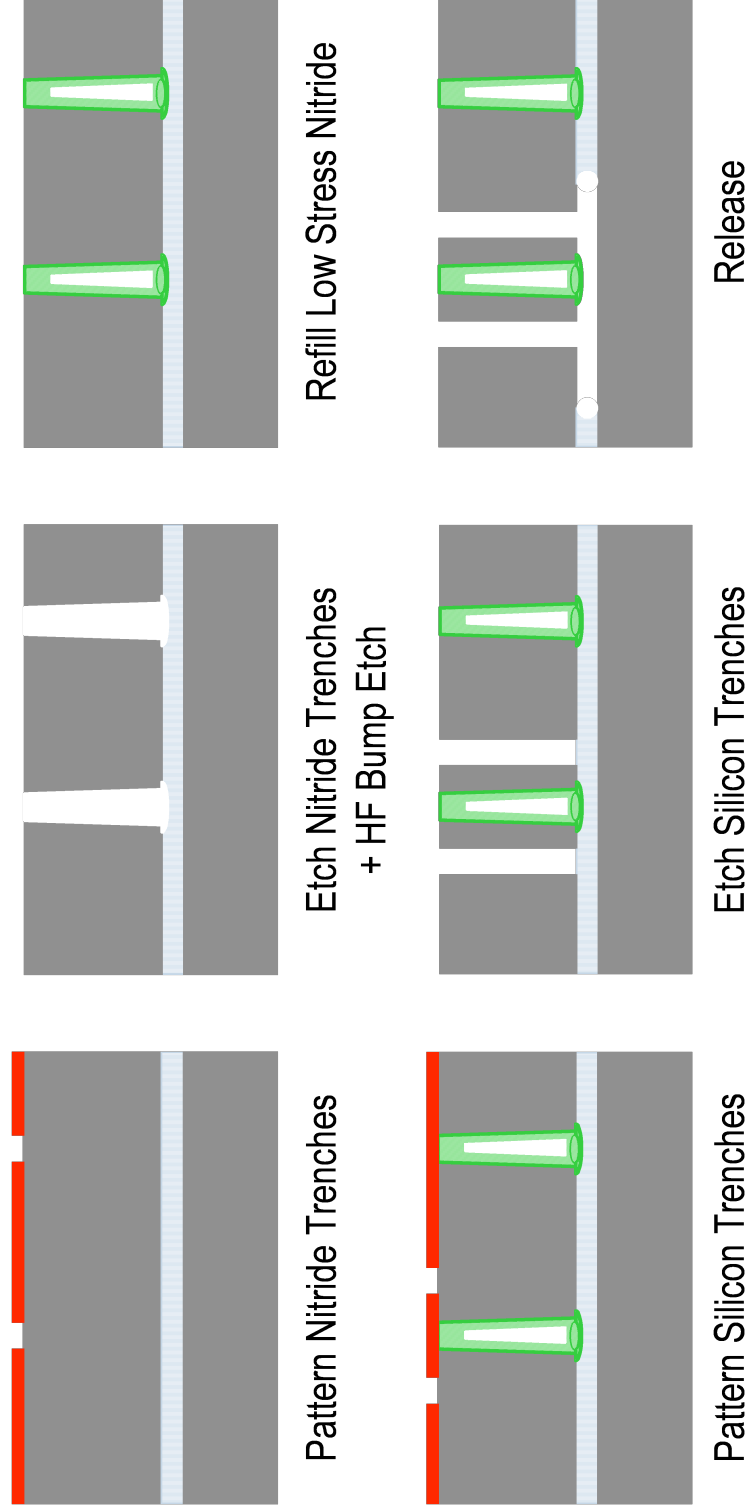


Figure 4.15: Froghopper Process Including Nitride Isolation. The Froghopper process includes an extra mask to create nitride trenches for insulating gap stops and electrical isolation of mechanically connected components. A backside etch will be added later to integrate these new inchworm motors with the micro rubber bands described in Chapter 3.

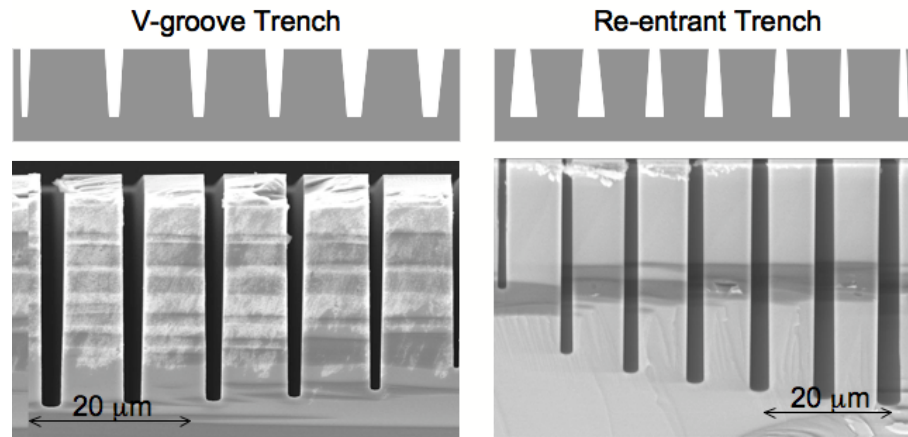


Figure 4.16: Silicon Nitride Trench Etch. Re-entrant trenches are required to prevent silicon from being masked by the nitride during the silicon trench etch.

Section 3.2.1 has been skipped.

The final result is a simple two-mask process (Figure 4.15). The process starts on a 4-inch SOI wafer with a  $20\ \mu\text{m}$  structure layer (frontside),  $5\ \mu\text{m}$  buried oxide (BOX), and  $300\ \mu\text{m}$  substrate (backside). These wafers were fabricated for the assembly process described in [78] and the thicker BOX layer is used for both assembly of staples and to prevent vertical pull-in of the device layer to the substrate.

First, the silicon nitride trenches are patterned and etched using a Surface Technology Systems (STS) Advanced Silicon Etch. This etch step requires re-entrant trenches as seen in Figure 4.16 and described by Bellew in [86]. If a trench is etched as a v-groove instead, the silicon nitride that refills the trench could serve as a mask during the subsequent silicon trench etch. The resulting silicon surrounding the nitride beam would provide a low resistance path along the nitride beam which would defeat the purpose of the silicon nitride for electrical isolation. After these trenches are etched, a 4 minute dip in 5:1 BHF is used to define the targeted  $0.4\ \mu\text{m}$  deep silicon nitride bumps beneath the silicon device

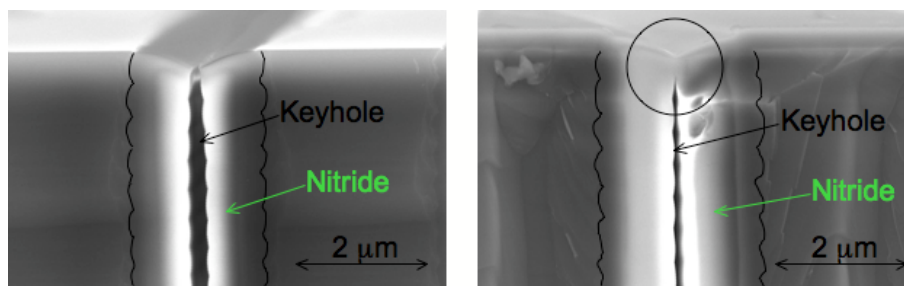


Figure 4.17: Low-Stress Silicon Nitride Deposition. A keyhole will form when depositing low-stress silicon nitride. While a second deposition partially plugs the opening (and others have used undoped polysilicon to plug this hole [86, 87]), it was found that leaving the top of the nitride trench unplugged did not matter in device operation.

layer.

After these trenches have been etched, they are refilled with low-stress silicon nitride. This silicon nitride layer is deposited to a thickness of approximately  $1.8 \mu\text{m}$  and etched back using an oxide etch in the LAM plasma etcher to expose the silicon. The low-stress silicon nitride deposition is not very conformal and the re-entrant nature of the trench leads to keyholes being formed in the silicon nitride. If a single  $2 \mu\text{m}$  layer of silicon nitride is deposited and etched back, the top of the trench remains open as seen in Figure 4.17. A second deposition of  $0.5 \mu\text{m}$  low-stress silicon nitride can be used to plug the top of the silicon nitride beams, but it was determined that this extra step was not necessary to the performance of motors. Other work has used undoped polysilicon to better refill these trenches successfully as well [86, 87].

Once the silicon nitride has been deposited and etched back, the silicon trenches are patterned and etched using the same STS Advanced Silicon Etch. The resulting structures are released using a timed 49% HF wet etch and a critical point dry. Since HF etches silicon nitride, the hole in the refilled trenches gets larger at a rate of approximately  $50 \text{ \AA}/\text{min}$  as

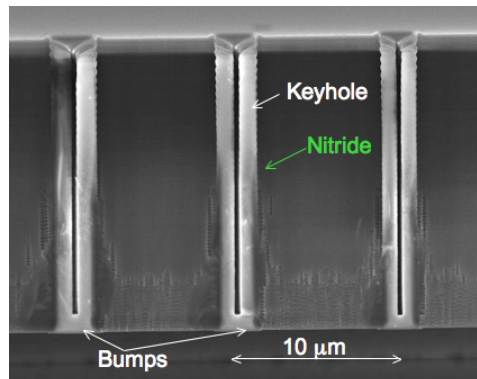


Figure 4.18: Nitride Trenches After Oxide Release. The keyhole in the silicon nitride trenches opened up a bit more after the 49% HF etch and the silicon nitride bumps can be seen after the buried oxide is removed.

seen in Figure 4.18. Finally, an AMST Molecular Deposition System MVD100 is used to deposit a monolayer of fluoro octyl trichloro silane (FOTS) to further reduce stiction to the substrate.

#### 4.2.2 Layout Guidelines

The fabrication steps listed above result in a number of differences between the original two dimensional layout and the resulting devices. If ignored, these differences will lead to non-working motors or motors with significantly limited performance. Chief among the processing considerations is the lateral etch that occurs during both of the STS Advanced Silicon Etches – one for the refilled silicon nitride trenches and one for the silicon trenches. Due to the cyclic nature of the repeated etch/deposition steps that occur during this etch, the trenches grow in size from the devices which were originally laid out and masked onto the wafer (Figure 4.19). Because the silicon nitride trenches are refilled, the silicon nitride beams expand  $\delta$  in size from the layout and the silicon beams shrink  $\delta$  in size.

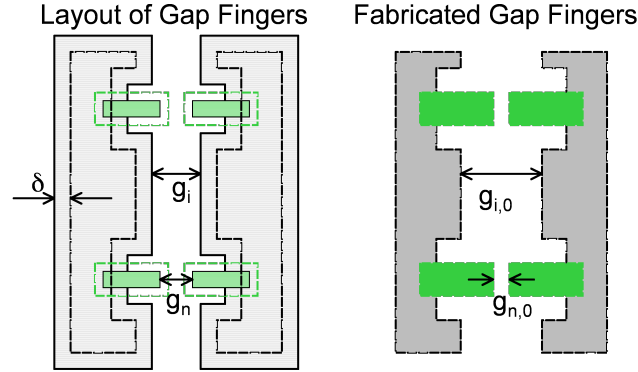


Figure 4.19: Effect of Lateral Etch on Fabricated Devices.

The following sections detail the consequences of this lateral etch on the devices intended to improve the work density of inchworm actuators designed in the sections above.

### Transmission

The lateral etch that occurs in the interface between the transmission actuator and the drive actuator shown in Figure 4.20 will have a large impact on the drive actuator's initial gap once the transmission actuator is engaged. Even without the transmission engaged, the initial gap in the drive actuator will be expanded by the lateral etch  $\delta$ .

$$g_{i,0} = g_i + 2\delta \quad (4.10)$$

With the transmission engaged, the initial gap in the drive actuator becomes even more dependent on the lateral etch. In this case, the distance traveled by the transmission actuator when fully engaged  $g_{tn}$  is reduced and the gap between the drive and transmission actuators  $g_t$  is expanded.

$$g_{i,1} = g_{i,0} - g_{tn,0} + g_{t,0} = g_i - g_{tn} + g_t + 6\delta \quad (4.11)$$

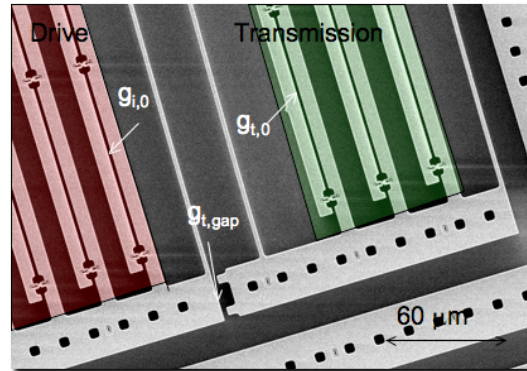


Figure 4.20: Fabricated Transmission Interface. The lateral etch that occurs during the silicon trench etch will affect the initial gap that results in the drive actuator when the transmission is engaged.

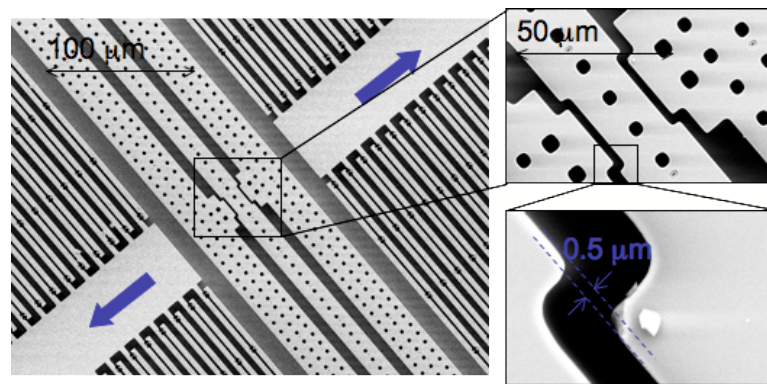


Figure 4.21: Fabricated Friction Clutch. The lateral etch that occurs during the silicon trench etch also has a large affect on the flexure force provided by the clutch actuator.

In order to ensure that the transmission is effective, an inequality can be used to define  $g_{tn}$  based on  $g_t$  and the lateral etch.

$$g_{tn} > g_t + 6\delta \quad (4.12)$$

As the lateral etch increases, the initial gap in the transmission actuator will also increase.

## Friction Clutch

The fabricated friction clutch shown in Figure 4.21 also depends heavily on the lateral etch that occurs during the DRIE steps. In this case, there are two primary culprits which will lessen the force available from the clutch significantly over what was originally designed in the clutch layout.

The first issue is the clutch spring displacement when the clutch is gripping the shuttle (Figure 4.11). The motor shuttle is fabricated with the motor, but because the friction clutch is designed to be normally closed, a small cut-out is provided in the shuttle. This cut-out defines an overlap distance between the clutch and the shuttle which determines the amount of spring displacement and therefore motor force when the clutch is closed. This overlap is also subject to the lateral etch and will decrease as the lateral etch increases.

$$x_{ol,0} = x_{ol} - 2\delta \quad (4.13)$$

When this overlap shrinks, the clutch gripping force is less than originally designed.

$$F_{clutch} = k_{clutch}x_{ol,0} \quad (4.14)$$

In addition to the spring displacement, the beams used to define the clutch spring constant  $k_{clutch}$  are thinned by the lateral etch. The spring constant is proportional to the beam width,  $b$ , cubed.

$$k_{clutch} \propto (b - 2\delta)^3 \quad (4.15)$$

Weaker springs coupled with a smaller displaced distance when the clutches are closed lead to a significantly weaker clutch force. For a lateral etch of  $0.2 \mu\text{m}$  and the layout dimensions

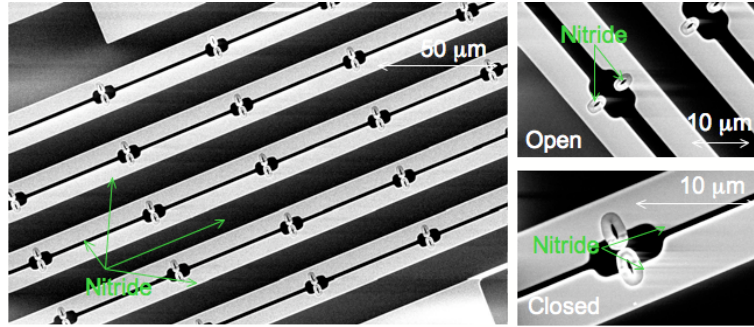


Figure 4.22: Fabricated Silicon Nitride Gap Stops. The lateral etch during both the nitride trench etch and the silicon trench etch both determine the final gap in the drive and clutch actuators.

for the clutch actuator in Figure 4.21, the clutch force is reduced 50%. Of course, if the lateral etch is known ahead of time, the original layouts can be adjusted accordingly.

### Gap Stops

The silicon nitride gap stops in Figure 4.22 are designed with a number of alignment and lateral etch issues in mind. As described in the sections above, the lateral etch will impact the final gap when these gap fingers are closed. The gap drawn between the silicon fingers  $g_i$  and the gap drawn between the nitride gap stops  $g_n$  will determine the final gap  $g_f$ .

$$g_{f,0} = g_{i,0} - g_{n,0} = g_i - g_n + 4\delta \quad (4.16)$$

If the lateral etch  $\delta$  is large and the desired final gap small, the gap drawn between the nitride gap stops can be drawn larger than the gaps between the silicon gap fingers – a somewhat unintuitive result.

The other more subtle fabrication design concern is the alignment between the silicon nitride trenches and the silicon trenches. Each gap stop has a piece of the silicon gap

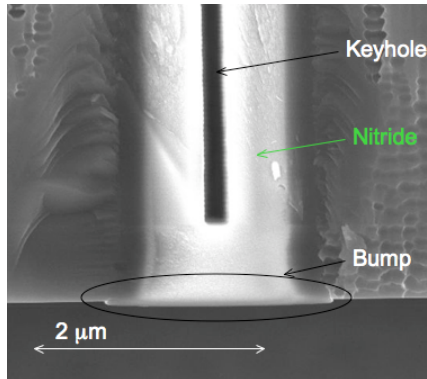


Figure 4.23: Fabricated Silicon Nitride Bump. The silicon nitride bumps were not nearly as large as expected and only extended approximately 50-100 nm below the bottom of the device layer.

finger etched around it to allow for the gap stops to work properly even in the case where the two masks are badly misaligned.

### Nitride Bumps

Finally, the nitride bumps discussed in the fabrication section have been included on all moving parts of the motor including the motor shuttle. While these bumps were originally fabricated with the intent of being much larger to prevent stiction, the fabricated bumps only extended approximately 50-100 nm below the bottom of the device layer (Figure 4.23). Due to the significantly reduced etch rate at the bottom of the trenches, the presence of stiction will have serious ramifications on the motor performance in Section 4.3.2.

## 4.3 Characterization and Results

Once the motors were fabricated in the new Frogopper process, the new motor components were characterized and the motors were tested. Several test structures were

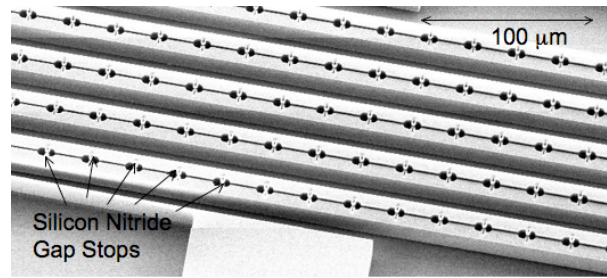


Figure 4.24: Pull-In Test with Varied Gap Stop Spacing.

fabricated separately to measure pull-in limits on silicon nitride gap stops, the coefficient of friction for DRIE silicon sidewalls, and the efficacy of the silicon nitride for isolation purposes. Finally, a test setup was built to program and test the new motors for force, displacement, and speed.

### 4.3.1 Process Characterization

While adding silicon nitride to an SOI process like this one is not new, some process characterization is necessary to design better motors in future runs. Specifically, the pull-in voltage for gap fingers with the nitride gap stops is measured as well as the coefficient of friction between deep reactive ion etched silicon sidewalls.

#### Gap Stops

Multiple test structures like the one shown in Figure 4.24 were used to measure the pull-in voltage for gap fingers with integrated silicon nitride gap stops. Each silicon nitride gap stop reduces the actuation area in the motor however, so it is important to minimize the number of gap stops. An analytical model described by Pamidighantam in

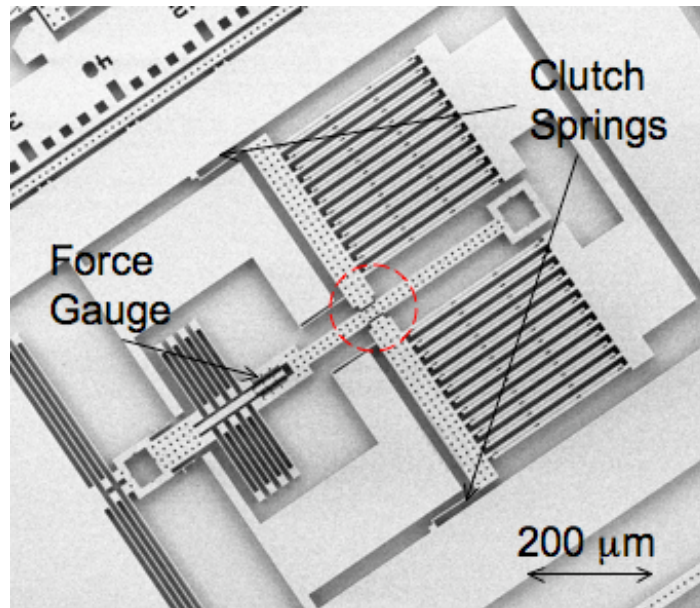


Figure 4.25: Coefficient of Friction Test Structure.

[88] was used to calculate estimated pull-in voltages for clamped-clamped beams. With a length between gap stops of  $240\ \mu\text{m}$ , the beams in Figure 4.24 were estimated to pull in at  $104\ \text{V}$ . A gap stop spacing of  $100\ \mu\text{m}$  was estimated to pull-in at over  $650\ \text{V}$ .

Using the test structure in Figure 4.24, gap stops spaced  $100\ \mu\text{m}$  with a final gap of  $0.7\ \mu\text{m}$  have been shown to prevent shorting at voltages over the maximum tested  $135\ \text{V}$ . Gap stops spaced  $240\ \mu\text{m}$  apart with a final gap of  $0.7\ \mu\text{m}$  failed at  $45\ \text{V}$ . The discrepancy between the estimated and experimental pull-in voltages is likely due to the fact that the beams are not fully clamped on each end. The nitride gap stops are also allowed to rotate when they are in contact with each other resulting in a lower than estimated pull-in voltage.

## Friction Clutch

Because the coefficient of friction has not been measured between deep reactive ion etched silicon surfaces in the past, it is also necessary to obtain some preliminary coefficient of friction measurements for future friction clutch designs. The device in Figure 4.25 was used to measure the coefficient of friction. It uses a similar shuttle preset design to the one described in Section 4.2.2 and mimics the full clutch design as closely as possible.

To measure the coefficient of friction, the clutch is first opened and the shuttle is manually preset with a probe tip. Then the shuttle is displaced a given distance so that the spring in the force gauge is applying a “load” force on the shuttle. The clutch is engaged and shuttle slipping is observed through a microscope. The load on the shuttle is increased until the clutch slips. All of the spring beam widths were measured in a SEM to more accurately calculate applied forces. In the first trial, the calculated coefficient of friction when the shuttle slipped was 2.6. In trials 2-4, the calculated coefficient of friction at the onset of slipping was approximately 1.6.

Unfortunately, this test structure is not set up so that this number can be measured easily multiple times. A test structure similar to the one designed by Timpe in [84] would be more conducive to accurately measuring the coefficient of friction. Because the coefficient of friction numbers varied, it is expected that adhesion plays a large role in the interface between the clutch and the shuttle, especially in the first clutch/shuttle interaction.

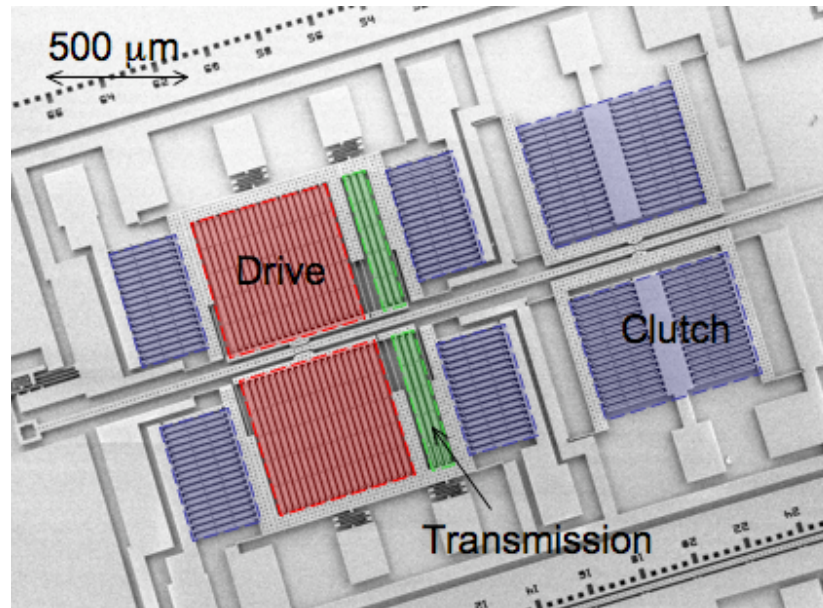


Figure 4.26: Fabricated Inchworm Motor.

### 4.3.2 Motor Characterization

The next step was to test the new motor designs. The motor in Figure 4.26 was designed to provide 1 mN of force with a displacement of 1 mm. It was tested using a National Instruments PCI-6503 digital I/O board controlled through Matlab and connected to an Agere Systems LSP2916 16-channel high voltage amplifier chip. A simple Matlab program controls the outputs of the PCI-6503 board and an Analog Devices AD8403 digital potentiometer which sets the voltage level output up to 160 V. The highest frequency square wave output available is approximately 1 kHz.

Using this test setup, the inchworm motor shuttle was stepped approximately 50 μm with the transmission actuator engaged (Figure 4.27). Unfortunately, stiction proved to be a larger problem than originally anticipated and the shuttle experienced large adhesion

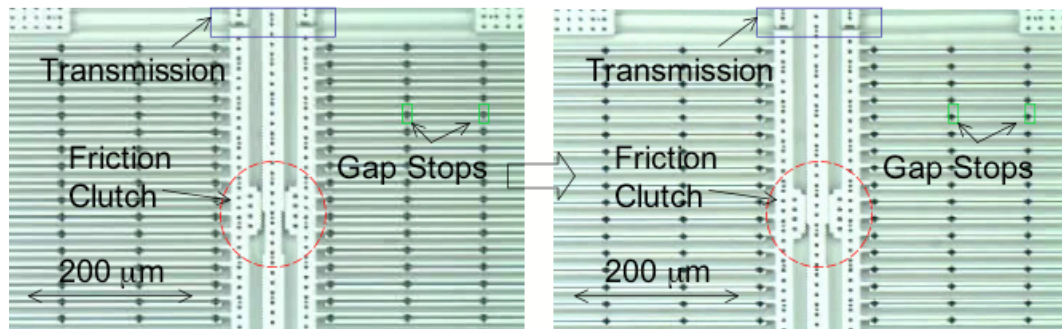


Figure 4.27: Frames from New Inchworm Motor Operation. With the transmission actuator engaged, the shuttle was translated approximately  $50 \mu\text{m}$ . Motor travel was limited due to stiction between the shuttle and the substrate and the shuttle would not move at all if the transmission was not engaged.

forces from the substrate. These forces were apparent even when a probe tip was used to preset the shuttle. When the transmission actuator was not engaged, the motor did not have enough force to pull the shuttle.

Several solutions exist to improve the performance of these motors in future fabrication runs. First, much of the substrate beneath the shuttle can be removed and the nitride bumps beneath the device layer can be enlarged to further reduce shuttle stiction. This motor also suffered decreased performance due to a larger than expected lateral etch described in Section 4.2.2. Better efforts to characterize this lateral etch and working on ways to cancel it out will be a priority for future motor designs.

## Chapter 5

# Power, Control, and Integration

The only two remaining components required for an autonomous jumping micro-robot are the power and control systems. While power and control are not the focus of this dissertation, the mechanical components described above still need to be designed to integrate with available power and control technologies. Designing an appropriate power supply for an autonomous jumping microrobot offers a particularly difficult challenge. This power supply should provide enough energy for multiple jumps (preferably rechargeable in some fashion), occupy small area and mass, and offer simple integration to the actuators. The controller should be able to sequence the motors properly and consume low power. Ideally this controller should also be programmable to allow for future iterations in robot and motor design as well as the integration of sensors.

In addition, all of the components (energy storage, motor, power, and control) need to work together and be assembled into the final microrobot. Ideally, this integration process will be simple and robust. However, simple and robust integration is another particularly

difficult challenge for building autonomous mobile microrobots.

## 5.1 Power

Power supplies in small packages are a hot topic for research and a crucial one for microrobots and small wireless sensors. One area of research is in thin-film printable batteries like the polymer printed by Steingart in [54]. These batteries and other polymers usually only have open circuit voltages of approximately 3 V or lower. Larger off-the-shelf lithium ion batteries are also sizing down to sub-gram masses, but these are too large for 10 mg microrobots and still supply low voltages [89]. Even though these batteries may supply high energy densities, matching the power supply to the actuators is crucial for both power efficiency and mass. Many batteries are available at low voltages, but would require additional power circuitry, and therefore extra mass and area, to provide the high voltages required by many actuators. Connecting batteries like these in series to provide higher voltages is an opportunity for future research.

Other, more unique small sources of power include nuclear power supplies and energy scavenging technologies. Lal used small amounts of radioactive isotopes to provide power by bending a small cantilever with piezoelectric material [90]. While, power sources like this are promising, the power output is only 10s of nW for now – not quite enough power for these microrobots. Energy scavenging is another interesting approach for providing power. In this case, the robot would scavenge energy from its environment through vibration, heat, light, etc. [56].

This robot will use the solar cells demonstrated by Hollar and Bellew with the

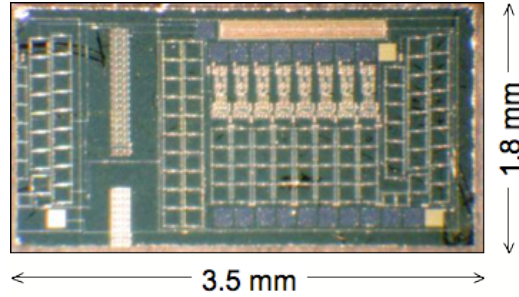


Figure 5.1: High Voltage Solar Cells [86]

microrobot in [28]. By using an SOI wafer and trench isolation to separate solar cells, they may be stacked to achieve higher voltages. In [86], arrays greater than 88 V were demonstrated with efficiencies of up to 14%. Each solar cell chip also provides eight high voltage buffers to amplify signals from the microcontroller to the voltages required to drive the motor. These chips are  $3.6 \times 1.8 \text{ mm}^2$  in area and 2.3 mg and are shown in Figure 5.1. While these solar cells were custom made in the UC Berkeley Microlab, commercial variations are starting to come on the market including the CPC1840 with a 16 V supply [91].

While solar cells may not be the perfect answer for microrobots in the long run, they satisfy the basic jumping microrobot requirements. It is more important to examine the power requirements of the autonomous jumping microrobot designed in this dissertation so that an improved power supply may be designed in the future. One source of power dissipation in this microrobot design is the motor. Because the motor is capacitive, the input power can be calculated as

$$P_{motor} = 2(C_{clutch} + C_{clutch,parasitic})V_c^2 f + (C_{drive} + C_{drive,parasitic})V_d^2 f \quad (5.1)$$

With an initial gap of  $2\ \mu\text{m}$  and a final gap of  $1\ \mu\text{m}$ , the drive capacitance  $C_{drive}$  is calculated to be  $32\ \text{pF}$  in the closed position for a  $10\ \text{mN}$  motor. The closed position is used for a worst-case estimate. With an initial gap of  $1.5\ \mu\text{m}$  and a final gap of  $1\ \mu\text{m}$ , the total clutch capacitance assuming a coefficient of friction of  $0.5$  is  $38\ \text{pF}$ . Parasitic capacitances are due to bond pads and the substrate as well as the nitride isolation structures between silicon blocks. Based on the layout in Figure 4.14, the parasitic capacitance for both the motor and clutch is estimated to be approximately  $1.6\ \text{pF}$ . With a voltage of  $50\ \text{V}$  and a frequency of  $500\ \text{Hz}$ , the total motor input power is expected to be  $45\ \mu\text{W}$  at  $50\ \text{V}$ . Obviously, this power can be decreased by moving the motor more slowly, but this will reduce the robot's jump frequency.

Table 5.1: Power Requirements for Autonomous Jumping Microrobot.

	Voltage (V)	Current ( $\mu\text{A}$ )	Power ( $\mu\text{W}$ )
Motor	50	0.9	45
High Voltage Buffers	50	0.5	25
Microcontroller	2	5.8	11.6
Total			81.6

Other components which will draw power include the microcontroller described below and the high voltage buffers in the solar cells. In [83], the high voltage buffers were demonstrated drawing approximately  $25\ \mu\text{W}$  when operating at  $500\ \text{Hz}$ . The microcontroller below draws  $5.8\ \mu\text{A}$  of current at  $2\ \text{V}$  for a total power dissipation of  $11.6\ \mu\text{W}$  in active mode at  $32\ \text{kHz}$ . In sleep mode, the microcontroller only draws  $3.3\ \mu\text{A}$ . Overall, the expected power required for an autonomous jumping microrobot is given in Table 5.1. Obviously, most of this power is only required when the robot is stretching the micro rubber band

to get ready for a jump. It is conceivable that the microrobot remains ready for a jump with very low power dissipation for long time intervals. Behavior like this could be very conducive to a power solution like energy scavenging.

## 5.2 Control

The control requirements for the microrobot at this stage are fairly simple – sequence the motors to store energy in the micro rubber band and release it. Previous microrobot designs have generally been controlled off-chip, although Hollar used a custom CMOS sequencer to control the microrobot motors in [28]. This sequencer was extremely low power and consumed only 22 nW of power at 1 V.

To eventually realize some of the microrobot applications listed in Chapter 1, controllers will be required to provide more than simple state machines. Sensors and communication will be required to complete the microrobot. Smart dust provides one example of sensing and optical communication in a very low-power package, and Warneke designed a custom CMOS controller to provide the brains [10]. Warneke also designed an ultra-low power microcontroller that consumes 5.9  $\mu$ W at 1 V for the smart dust project and something similar could be useful in future microrobot designs [92].

However, all of these approaches have been custom and it would be ideal to find an off-the-shelf microcontroller that requires minimal power instead. Dust Networks sells an off-the-shelf system-in-package with both a microcontroller and low-power radio that consumes 6-7 mA at 3 V when the radio is transmitting or receiving [94]. Due to the power requirements of using a radio, wireless microrobots may still be a long way off.

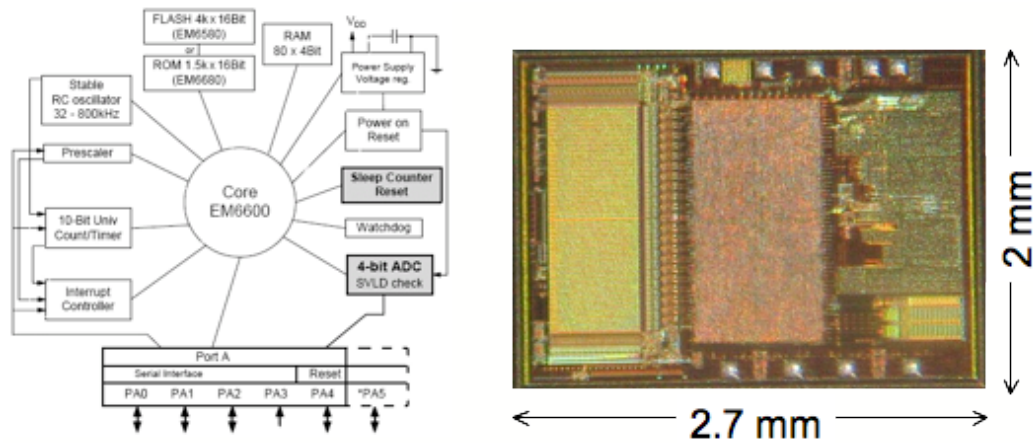


Figure 5.2: EM6580 Programmable Microcontroller [93]

Without the radio, the commercially available EM Microelectronics EM6580 4-bit microcontroller (Figure 5.2) requires no external components and runs on  $5.8 \mu\text{A}$  active and  $3.3 \mu\text{A}$  standby current at  $2 \text{ V}$  [93]. The EM6580 microcontroller has flash memory for reprogrammability as well as 5 output channels which are more than enough to drive a single inchworm motor. These microcontrollers are also small in size at  $2 \times 2.7 \text{ mm}^2$  and  $3.5 \text{ mg}$  with the potential of weighing even less if thinned down.

The required motor sequencing is fairly simple and described by the motor steps pictured in Figure 4.9. The EM6580 also provides an extra pin connected to a 4-bit ADC as seen in Figure 5.2 for future sensor integration. With such a large commercial interest in ultra low power wireless sensor networks, it is expected that even more options for ultra low power microcontrollers will be available in the near future.

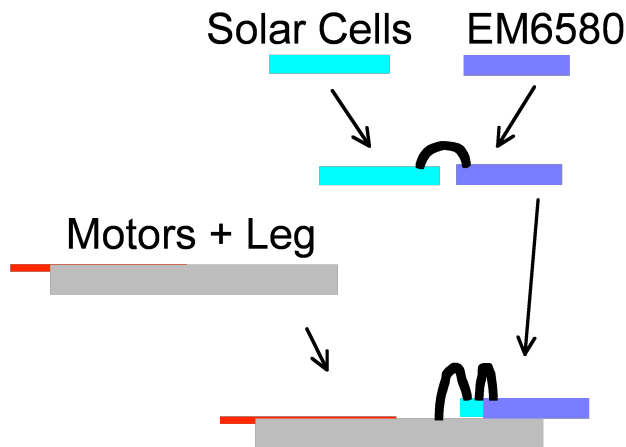


Figure 5.3: Microrobot Assembly through Wirebonds.

### 5.3 Integration

Finally, these power and control solutions need to be integrated with the energy storage component from Chapter 3 and the motor from Chapter 4. Previous work in integrating these components has been fairly limited. Fluidic self-assembly in which components are placed in a fluid and capillary forces are used to pull devices together has always provided an attractive assembly option for microrobots [95]. Unfortunately, assembling fragile MEMS components can still be difficult due to the same fluidic forces that encourage assembly.

The microrobot in [28] demonstrated the most complete robot assembly solution to date. Hollar used simple wirebonds to assemble each component. However, the vibrational energy used to secure the wire in place also had numerous consequences on the fragile microrobot. Still, wirebonding is an effective means of integration and is the proposed integration method for this jumping microrobot as shown in Figure 5.3.

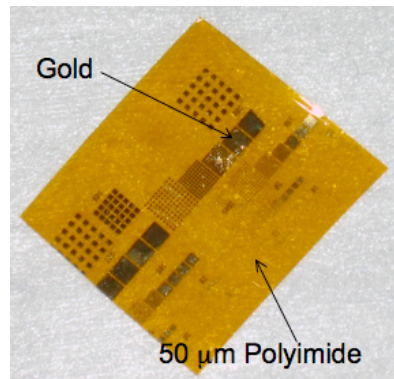


Figure 5.4: Flexible Printed Circuit Board for Microrobot Assembly (provided by Subramanian Venkatraman).

While wirebonds will likely suffice for the first jump of the microrobot, future microrobots will require a more robust integration method. One idea for integrating microrobot parts of the future is to use an ultra thin ( $50\ \mu\text{m}$ ) flex printed circuit board (PCB) like the one in Figure 5.4. Components, especially chip components like microcontrollers and power supplies can easily be integrated before the MEMS components are added and the flex PCB can even become part of the robot's body. In a jumping microrobot, a flex PCB could even be used to set the initial take-off angle for the robot.

## 5.4 Prototypes

Several prototypes have been built to demonstrate total system functionality. First, a small-scale version of the full system has been prototyped with the solar cells and EM6580 driving an inchworm motor. Separately, an inchworm motor has been demonstrated pulling and storing energy in a micro rubber band. Finally, a mechanical mockup of the full robot has been built to better understand how these pieces will eventually fit

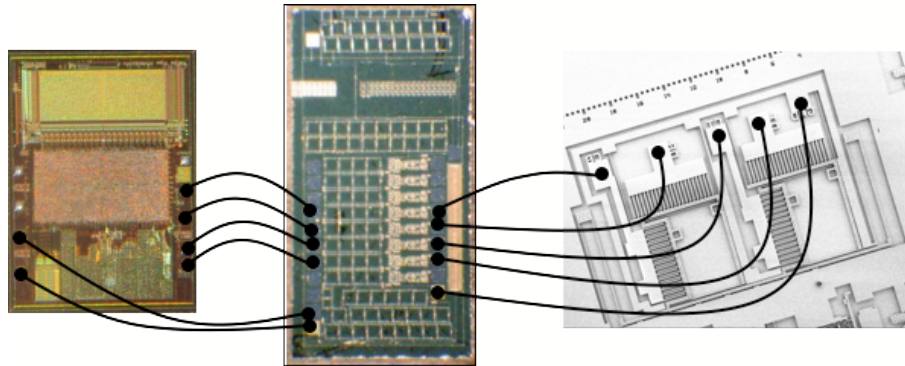


Figure 5.5: System Integration Test.

together.

#### 5.4.1 Solar Cells, Microcontroller, and Inchworm Motor

For the first prototype system, a small solar cell array has been used to power the EM6580 microcontroller which drives a small inchworm motor. Due to the use of a solar cell array designed to provide approximately  $2 \mu\text{A}$  of current at 1 sun for the microcontroller power, a much higher powered light source was used in testing. The measured open-circuit voltage ( $V_{oc}$ ) and short-circuit current for the solar cell microcontroller supply were 3.5 V and  $15 \mu\text{A}$  respectively. For the particular solar cell array used, the voltage controlling the inchworm motors was measured at 19 V.

For this test, the solar cell array, microcontroller, and inchworm motor were all bonded into separate packages and wired together on a single breadboard for convenience (Figure 5.5). Black electrical tape was placed over the high voltage buffers on the solar cell chip to prevent light-related current leakage since a metal light shield was not provided during processing. The microcontroller was programmed to step the inchworm 10 times

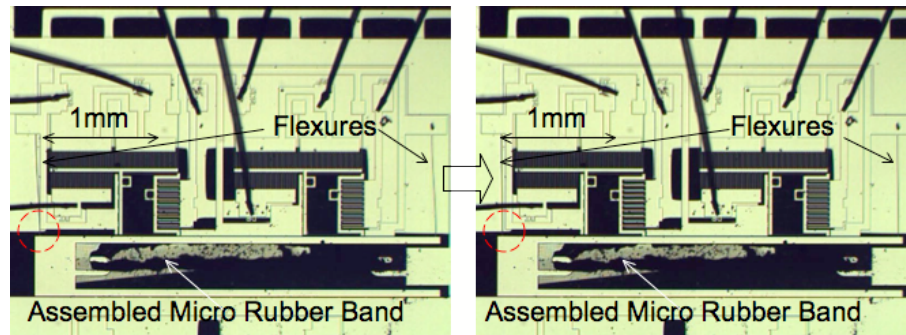


Figure 5.6: Inchworm Motor Stretching a Micro Rubber Band. Although only a limited force was available from this motor, the motor was still able to stretch the micro rubber band  $30\ \mu\text{m}$  to store an estimated  $4.9\ \text{nJ}$  of energy.

at a slow speed of  $1\ \text{Hz}$  for observation. Unfortunately, slipping in the motors gear teeth (Figure 4.8) prevented the shuttle from moving very far, but it did take 1.5 steps for a total displacement of  $6\ \mu\text{m}$  at an estimated force of  $2.5\ \mu\text{N}$ . The  $50\ \text{V}$  solar cells would provide much greater force, but were not used in this test due to limited availability.

#### 5.4.2 Inchworm Motor and Micro Rubber Band

To test the integration of the micro rubber bands with an inchworm motor, a fully integrated micromechanical energy storage system was designed and tested by stretching a micro rubber band with an old inchworm motor. Because the Frogopper process does not include a backside etch to easily assemble a micro rubber band, an inchworm motor without the innovations described in Chapter 4 was fabricated in the silicon process from Chapter 3. A laser cut silicone micro rubber band was assembled pre-strained into this small electrostatic inchworm motor (Figure 5.6). The inchworm motor was actuated with the off-board controller described in Section 4.3.2 at  $90\ \text{V}$  for approximately  $225\ \mu\text{N}$  of force and displaced  $30\ \mu\text{m}$ , at which point the motor's gear teeth began to slip.

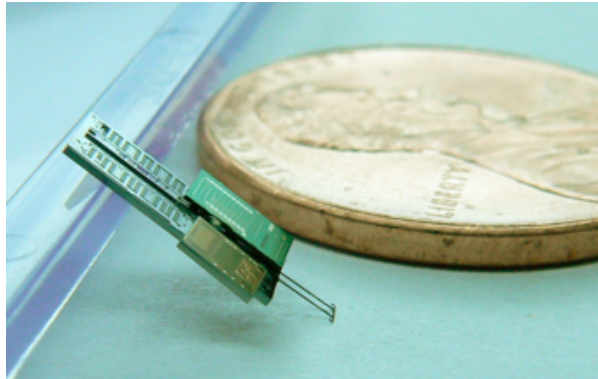


Figure 5.7: Fully Integrated Mockup.

The energy stored by the inchworm motor was calculated by assuming that a maximum force of  $225 \mu\text{N}$  was used to stretch the micro rubber band. Because the micro rubber band is assembled “pre-strained,” energy is also stored in the micro rubber band during assembly as described in Section 3.2.4. A load force of  $100 \mu\text{N}$  from pre-straining was estimated by assembling a similarly fabricated micro rubber band into a force gauge elsewhere on the chip, and approximately  $3 \text{ nJ}$  was stored due to pre-straining during assembly. Therefore, it was estimated that the inchworm stored an additional  $1.9 \text{ nJ}$  of energy before slipping for a total of  $4.9 \text{ nJ}$  stored and quickly released. The new inchworm motors designed in Chapter 4 will increase this stored energy to the tens of microJoules needed for tens of centimeters jumps.

### 5.4.3 Final Robot Mockup

Finally, a mechanical mockup of what the final robot might look like was assembled and is shown in Figure 5.7. This mockup gives some perspective on the final size of the robot as well as better ideas on how to assemble the separate components.

## Chapter 6

# Conclusions and Future Work

This dissertation has described the design of an autonomous jumping microrobot and the fabrication of the micro-scale components necessary for jumping. Three major challenges in building autonomous mobile microrobots were addressed – locomotion, mechanisms, and motors. Small legs and small steps make simple locomotion across a room difficult for millimeter-scale microrobots. Jumping has been presented as a relatively energy efficient means of transportation in which the robot can simply jump over obstacles. Fabricating capable mechanisms in simple processes is another challenge, and an elastomer-based micromechanical energy storage system has been designed and fabricated to store 10s of microjoules to jump without complex fabrication. Micro rubber bands are assembled onto silicon hooks for simple integration with other MEMS components. Making motors to stretch the micro rubber bands is another challenge and high work density electrostatic inchworm motors were designed and fabricated. While these motors have the potential of improving work density 550x over previous designs, fabrication problems led to limited

performance in the fabricated motors. Power and integration remain challenges to address in future work, and the above components were demonstrated working with high voltage solar cells and an off-the-shelf microcontroller.

Even with the accomplishments of this dissertation, jumping microrobots still have a long way to go before they reach the performance of the insects described in Chapter 1. One of these challenges will be in the microrobot landing and taking off again. Very simple mechanisms or passive structures may be utilized for the robot to land or reset itself correctly each time. For example, rat fleas land on their feet in 78% of their jumps if landing on a flat surface. During the descent, the flea spreads its legs laterally to help control the landing [41]. Another example of a relatively simple mechanism for a microrobot to right itself and even orient could be the toy Weebles [96]. By using a weighted and rounded base, the Weeble toys “wobble, but they don’t fall down.”

Power supplies that do not require direct sunlight will be important for applications which require the robot to go into darker places. Robust integration of the microrobot components is not a solved problem either. In addition, the ideas put forth in this dissertation have spawned countless new ones. The following sections discuss some ideas on future work related to the research done in this dissertation.

## 6.1 New Locomotion Paradigms

In Chapter 2, jumping was proposed as an effective means of transport for autonomous microrobots. While jumping is fairly efficient in practice, other modes of transport can theoretically provide even greater efficiency. Much like the Scout and Mini Whegs

robots in [33, 37], jumping can be used as a second means of transport on a walking microrobot to avoid larger obstacles. The energy storage system combined with an inchworm motor could be one component added to other microrobots.

Jumping can also be combined with other locomotion methods including flying and gliding. In many cases, flying insects jump to take off before flapping is engaged. A jumping mechanism could prove very useful on a robot like the micro flying insect (MFI) [21]. Gliding can be used to extend the range of a jump. If wings are deployed at the top of the jump, the cost of transport could decrease considerably. One can imagine Buzz Lightyear style wings which pop out when needed.

Finally, jumping offers another very efficient means of transportation – parasitic locomotion. In this case, the jumping microrobot could jump onto a much larger object moving nearby and use that object to move to a new location. The robot would then jump off and wait for the next larger entity moving in the direction it would like to go. One power source that could potentially match very well with parasitic locomotion is energy scavenging. While the robot waits for an object to move through its area, the robot could slowly be storing mechanical energy for a jump based on scavenged energy from the environment (vibrational, or otherwise).

## 6.2 New Fabrication Techniques

Many of the new fabrication techniques used to make the jumping microrobot components in this dissertation have inspired further ideas for microrobot fabrication. One way to improve robot performance and robustness is to add an elastomer like PDMS directly

into a standard SOI MEMS process. This addition can further improve motor force density, spring performance, and integration. The silicon/elastomer process will also add robustness so that the robot will be able to land and jump again.

Using silicon in combination with elastomer can provide substantial improvements for microrobot components over previous silicon-only designs as well as enable other MEMS systems. The elastomer can provide high friction surfaces for clamp-based electrostatic inchworm motors as well as non brittle springs to improve the motor force density and robustness. In addition, springs capable of storing enough energy to jump 20 cm when stretched can be directly integrated into the motors. The robot skeleton can also be made more robust to withstand the impact from landing after jumping 20 cm in the air.

While the energy storage system in Chapter 3 was successful, the separately fabricated and assembled springs led to low yields for the assembled system as well as poor consistency between springs due to the fabrication methods. Using the same elastomers integrated into the silicon process, yield is expected to improve by eliminating error-prone fabrication and assembly steps. In addition, elongation-at-break mean and standard deviation are expected to approach numbers seen in work not requiring elastomer assembly. Motor force density will improve over previous motor designs by using the elastomer as a high friction source in the motor clutches. Using clever device design to indent an elastomer coated sidewall with silicon teeth, the coefficient of friction and force density of the motor can be increased even further. Motor robustness can also be improved by using elastomer instead of brittle silicon springs.

Two big challenges remain before making these improved components a reality.

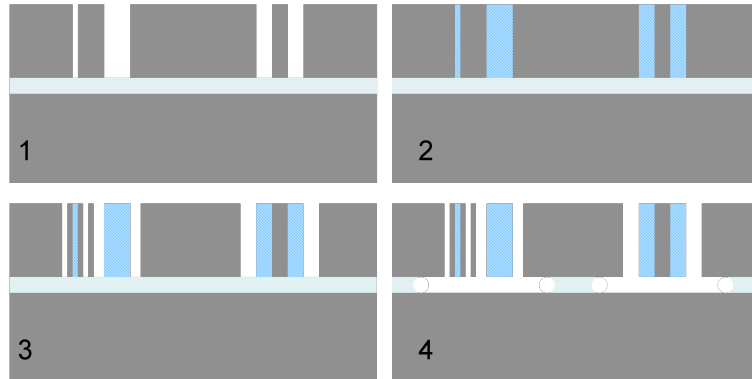


Figure 6.1: Proposed Silicon/Elastomer Process.

The first challenge is in process development and characterization. The elastomer needs to be integrated into an SOI process and adding a new material to any MEMS process is never a trivial task (Figure 6.1). The first step of this challenge will be to choose an elastomer which meets the mechanical and electrical characteristics required but can also survive the processing demands specifically the DRIE step (step 3) and the oxide release (step 4). In separate work, PDMS rubber has been shown to have high resilience to  $\text{SF}_6$  plasma and repeated short etches in BHF [97]. Survival of these steps along with elastomer adhesion to silicon and elastomer voltage breakdown will all need to be better understood before seriously approaching the second challenge.

The second challenge is to design high performance and robust springs and motors for jumping microrobots with the new processing capabilities. Springs will need to store and efficiently release as much energy as possible while staying in the same plane as the motor. The motor will require a high friction interface for the clutch and high forces to stretch and store energy in the spring. The robot skeleton, leg, and foot offer even more

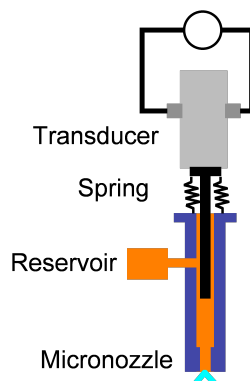


Figure 6.2: Microjet Injector.

design challenges to increase energy absorption for landing and improve the ability to take off in various environments. Silicon/Elastomer components open up a wide range of exciting possibilities for microsystems that need to be robust and adaptable to their environment, including autonomous jumping microrobots.

### 6.3 New Component Applications

Finally, future work will focus on new applications for the components developed for this autonomous jumping microrobot. While the microrobots themselves are a fun goal, the technology and ideas developed while building a microrobot can provide a greater impact on commercial technologies.

One interesting application for the micromechanical energy storage system in Chapter 3 is for medical devices. Specifically, microjet injectors as shown in Figure 6.2 and described in [51] require high shuttle velocity and power over a short period of time. Microjet injectors can be used to inject nanoliters of drug without pain or bruising. Batch

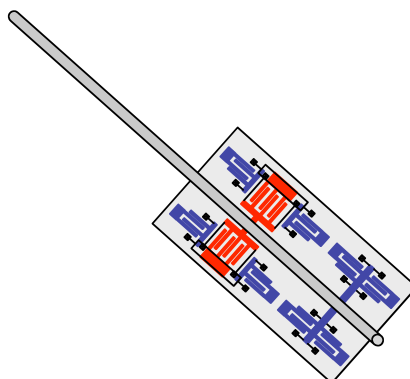


Figure 6.3: Inchworm Motor Robot Crawling along a Wire.

fabrication of cheap injector technology could provide an interesting means of dosing medication, especially in third world countries where skilled doctors and nurses may not be available.

The inchworm motors designed in Chapter 4 meet the design criteria necessary for cell phone zoom and autofocus microactuators – approximately 10 mN of force and several millimeters of motor travel. The Squiggle motor from Newscale is a somewhat larger piezoelectric solution to the same problem [79]. Squiggle motors have also found a market in nanopositioning for microscope applications that could potentially be improved with a smaller motor.

Finally, the inchworm motors can be used to build other microrobots. Instead of moving a shuttle, the inchworm motor could move itself in a microrobot which can climb along fibers or wires (Figure 6.3). Microrobots like these could find potential application for small-scale inspection tasks.

The work in this dissertation has demonstrated new ideas and designs for mobility,

mechanisms and actuation for mobile microrobots. Even more work is needed to reach the eventual goal of an army of networked mobile robots carrying sensor payloads, talking to each other, and realizing the applications in Chapter 1. It is hoped that many of the design ideas presented in this dissertation can spark future ideas for making autonomous mobile microrobots a reality.

# Bibliography

- [1] NASA-JPL. Mars exploration rover mission. [Online]. Available: <http://marsrovers.nasa.gov/home/>
- [2] J. Casper and R. R. Murphy, “Human-robot interactions during the robot-assisted urban search and rescue response at the world trade center,” *IEEE Transactions on Systems, Man, and Cybernetics - Part B: Cybernetics*, vol. 33, no. 3, pp. 367–385, 2003.
- [3] iRobot. irobot roomba vacuuming robot. [Online]. Available: <http://www.irobot.com>
- [4] N. Stephenson, *The Diamond Age*. New York: Bantam Books, 1995.
- [5] M. Crichton, *Prey*. New York: HarperCollins Publishers, 2002.
- [6] R. P. Feynman, “There’s plenty of room at the bottom,” *Journal of Microelectromechanical Systems*, vol. 1, no. 1, pp. 60–66, 1992.
- [7] P. Dario, R. Valleggi, M. C. Carrozza, M. C. Montesi, and M. Cocco, “Microactuators for microrobots: a critical survey,” *Journal of Micromechanics and Microengineering*, vol. 2, pp. 141–157, 1992.

- [8] S. D’Attanasio, R. Lazzarini, C. Stefanini, M. C. Carrozza, and P. Dario, “A one cubic centimeter mobile microrobot with a steering control,” in *IEEE/RSJ International Conference on Intelligent Robots and Systems*, 1997, pp. 1318–1324.
- [9] *IEEE Micro Robots and Teleoperators Workshop*, Hyannis, MA, 1987.
- [10] B. A. Warneke, M. D. Scott, B. S. Leibowitz, L. Zhou, C. L. Bellew, J. A. Chediak, J. M. Kahn, B. E. Boser, and K. S. J. Pister, “An autonomous 16mm<sup>3</sup> solar-powered node for distributed wireless sensor networks,” in *IEEE Sensors*, 2002.
- [11] J. Hill, R. Szewczyk, A. Woo, S. Hollar, D. Culler, and K. Pister, “System architecture directions for networked sensors,” in *International Conference on Architectural Support for Programming Languages and Operating Systems*, vol. 34, 2000, pp. 93–104.
- [12] S. Oh, L. Schenato, P. Chen, and S. Sastry, “Tracking and coordination of multiple agents using sensor networks: system design, algorithms and experiments,” *Proceedings of the IEEE*, vol. 95, no. 1, pp. 234–254, 2007.
- [13] M. P. Hamilton, E. A. Graham, P. W. Rundel, M. F. Allen, W. Kaiser, M. H. Hansen, and D. L. Estrin, “New approaches in embedded networked sensing for terrestrial ecological observatories,” *Environmental Engineering Science*, vol. 24, no. 2, pp. 192–204, 2007.
- [14] A. Kansal, M. Rahimi, D. Estrin, W. J. Kaiser, G. J. Pottie, and M. B. Srivastava, “Controlled mobility for sustainable wireless sensor networks,” in *IEEE Communications Society Conference on Sensor and Ad Hock Communications and Networks*, 2004, pp. 1–6.

- [15] S. Bergbreiter and K. S. J. Pister, “Cotsbots: An off-the-shelf platform for distributed robotics,” in *IEEE/RSJ International Conference on Intelligent Robots and Systems*, 2003.
- [16] A. Mainwaring, “Personal communication,” 2007.
- [17] A. Koga, K. Suzumori, H. Sudo, S. Iikura, and M. Kimura, “Electrostatic linear microactuator mechanism for focusing a ccd camera,” *Journal of Lightwave Technology*, vol. 17, no. 1, pp. 43–47, 1999.
- [18] J. Muthuswamy, M. Okandan, T. Jain, and A. Gilletti, “Electrostatic microactuators for precise positioning of neural microelectrodes,” *IEEE Transactions on Biomedical Engineering*, vol. 52, no. 10, pp. 1748–1755, 2005.
- [19] Epson. Monsieur: The ultraminiature robot that propelled itself into the guinness book. [Online]. Available: [http://www.epson.co.jp/e/company/milestones\\_23\\_monsieur.htm](http://www.epson.co.jp/e/company/milestones_23_monsieur.htm)
- [20] D. Strok, “Parking on a nickel,” *IEEE Intelligent Systems*, vol. 16, no. 2, pp. 6–7, 2001.
- [21] S. Avadhanula, R. J. Wood, E. Steltz, J. Yan, and R. S. Fearing, “Lift force improvements for the micromechanical flying insect,” in *IEEE/RSJ International Conference on Intelligent Robots and Systems*, 2003.
- [22] R. Yeh, “Articulated mechanisms and electrostatic actuators for autonomous micro-robots,” Ph.D. dissertation, University of California, Berkeley, 2001.

- [23] T. Ebefors, J. U. Mattsson, E. Kälvesten, and G. Stemme, “A walking silicon micro-robot,” in *International Conference on Sensors and Actuators (Transducers)*, 1999.
- [24] B. R. Donald, C. G. Levey, C. D. McGray, I. Paprotny, and D. Rus, “An untethered, electrostatic, globally controllable mems micro-robot,” *Journal of Microelectromechanical Systems*, vol. 15, no. 1, pp. 1–15, 2006.
- [25] T. Yasuda, I. Shimoyama, and H. Miura, “Microrobot actuated by a vibration energy field,” *Sensors and Actuators A - Physical*, vol. 43, pp. 366–370, 1994.
- [26] K. Suzuki, I. Shimoyama, and H. Miura, “Insect-model based microrobot with elastic hinges,” *Journal of Microelectromechanical Systems*, vol. 3, pp. 4–9, 1994.
- [27] M. H. Mohebbi, M. L. Terry, K. F. Böhringer, G. T. A. Kovacs, and J. W. Suh, “Omnidirectional walking microrobot realized by thermal microactuator arrays,” in *ASME International Mechanical Engineering Congress and Exposition*, 2001.
- [28] S. Hollar, A. M. Flynn, C. Bellew, and K. S. J. Pister, “Solar powered 10 mg silicon robot,” in *IEEE Conference on MicroElectroMechanical Systems*, 2003.
- [29] J. Burdick and P. Fiorini, “Minimalist jumping robots for celestial exploration,” *The International Journal of Robotics Research*, vol. 22, no. 7-8, pp. 653–674, 2003.
- [30] S. B. Kesner, J.-S. Plante, P. J. Boston, T. Fabian, and S. Dubowsky, “Mobility and power feasibility of a microrobot team system for extraterrestrial cave exploration,” in *IEEE International Conference on Robotics and Automation*, 2007, pp. 4893–4898.
- [31] J. German, “Hop to it: Sandia hoppers leapfrog conventional wisdom about

- robot mobility,” Sandia National Labs, Tech. Rep., 2000. [Online]. Available: [http://www.sandia.gov/LabNews/LN10-20-00/hop\\_story.html](http://www.sandia.gov/LabNews/LN10-20-00/hop_story.html)
- [32] U. Scarfogliero, C. Stefanini, and P. Dario, “Design and development of the long-jumping ”grillo” mini robot,” in *IEEE International Conference on Robotics and Automation*, 2007, pp. 467–472.
- [33] S. A. Stoeter and N. Papanikolopoulos, “Kinematic motion model for jumping scout robots,” *IEEE Transactions on Robotics*, vol. 22, no. 2, pp. 398–403, 2006.
- [34] M. Kovac, M. Fuchs, A. Guignard, J.-C. Zufferey, and D. Floreano, “A miniature 7g jumping robot,” in *submitted to IEEE International Conference on Robotics and Automation*, 2008.
- [35] M. Kovac, A. Guignard, J.-D. Nicoud, J.-C. Zufferey, and D. Floreano, “A 1.5g sma-actuated microglider looking for the light,” in *IEEE International Conference on Robotics and Automation*, 2007, pp. 367–372.
- [36] Q. Pei, R. Pelrine, M. Rosenthal, S. Stanford, H. Prahlah, and R. Kornbluh, “Recent progress on electroelastomer artificial muscles and their application to biomimetic robots,” in *Proceedings of SPIE: Smart Structures and Materials: Electroactive Polymer Actuators and Devices (EAPAD)*, Y. Bar-Cohen, Ed., vol. 5385, 2004, pp. 41–50.
- [37] J. M. Morrey, B. Lambrecht, A. D. Horchler, R. E. Ritzmann, and R. D. Quinn, “Highly mobile and robust small quadraped robots,” in *IEEE/RSJ International Conference on Intelligent Robots and Systems*, 2003, pp. 82–87.

- [38] Y. Sugiyama and S. Hirai, "Crawling and jumping by a deformable robot," *The International Journal of Robotics Research*, vol. 25, no. 5-6, pp. 603–620, 2006.
- [39] H. C. Bennet-Clark, "Scale effects in jumping animals," *Scale Effects in Locomotion*, pp. 185–201, 1977.
- [40] H. C. Bennet-Clark and E. C. A. Lucey, "The jump of the flea: a study of the energetics and a model of the mechanism," *The Journal of Experimental Biology*, vol. 47, pp. 59–76, 1967.
- [41] M. Rothschild, Y. Schlein, K. Parker, C. Neville, and S. Sternberg, "The flying leap of the flea," *Scientific American*, vol. 229, pp. 92–100, 1973.
- [42] M. Burrows, "Froghopper insects leap to new heights," *Nature*, vol. 424, p. 509, 2003.
- [43] —, "Neural control and coordination of jumping in froghopper insects," *Journal of Neurophysiology*, vol. 97, pp. 320–30, 2007.
- [44] J. C. Solem, "The motility of microrobots," in *Artificial Life III*, C. G. Langton, Ed., vol. XVII, 1992, pp. 359–380.
- [45] H. C. Bennet-Clark and G. M. Alder, "The effect of air resistance on the jumping performance of insects," *The Journal of Experimental Biology*, vol. 82, pp. 105–121, 1979.
- [46] S. Hollar, S. Bergbreiter, and K. S. J. Pister, "Bidirectional inchworm motors and two-dof robot leg operation," in *Transducers*, 2003.

- [47] S. H. Collins and A. Ruina, “A bipedal walking robot with efficient and human-like gait,” in *IEEE International Conference on Robotics and Automation*, 2005, pp. 1983–1988.
- [48] R. M. Alexander, *Principles of animal locomotion*. Princeton University Press, 2003.
- [49] A. Lipp, H. Wolf, and F.-O. Lehmann, “Walking on inclines: energetics of locomotion in the ant *Camponotus*,” *The Journal of Experimental Biology*, vol. 208, pp. 707–719, 2005.
- [50] (2007). [Online]. Available: <http://www.fentbattery.com/english/products5.htm>
- [51] A. Arora, I. Hakim, J. Baxter, R. Rathnasingham, R. Srinivasan, D. A. Fletcher, and S. Mitragotri, “Needle-free delivery of macromolecules across the skin by nanoliter-volume pulsed microjets,” *Proceedings of the National Academy of Sciences of the United States of America*, vol. 104, no. 11, pp. 4255–4260, 2007.
- [52] M. S. Rodgers, J. J. Allen, K. D. Meeks, B. D. Jensen, and S. L. Miller, “A micromechanical high-density energy storage / rapid release system,” in *SPIE Conference on Micromachined Devices and Components V*, vol. 3876, 1999, pp. 212–222.
- [53] C. Rose and G. Wright, “Inscribed matter as an energy-efficient means of communication with an extraterrestrial civilization,” *Nature*, vol. 431, pp. 47–49, 2004.
- [54] D. Steingart, C. C. Ho, J. Salminen, J. W. Evans, and P. K. Wright, “Dispenser printing of solid polymer - ionic liquid electrolytes for lithium ion cells,” in *IEEE Polytronic*, 2007.

- [55] M. Hill and C. O. Mahony, “Modelling and performance evaluation of a mems dc/dc converter,” *Journal of Micromechanics and Microengineering*, vol. 16, pp. S149–S155, 2006.
- [56] S. Roundy, P. K. Wright, and K. S. J. Pister, “Micro-electrostatic vibration-to-electricity converters,” in *ASME International Mechanical Engineering Congress and Exposition*, 2002.
- [57] E. S. Leland and P. K. Wright, “Resonance tuning of piezoelectric vibration energy scavenging generators using compressive axial preload,” *Smart Materials and Structures*, vol. 15, pp. 1413–1420, 2006.
- [58] W. Lindsay, D. Teasdale, V. Milanovic, K. S. J. Pister, and C. Fernandez-Pello, “Thrust and electrical power from solid propellant microrockets,” in *IEEE Conference on MicroElectroMechanical Systems*, 2001.
- [59] D. Y. R. Chong, W. E. Lee, B. K. Lim, J. H. L. Pang, and T. H. Low, “Mechanical characterization in failure strength of silicon die,” in *IEEE Thermal and Thermomechanical Phenomena in Electronic Systems*, vol. 2, 2004, pp. 203–210.
- [60] H. C. Bennet-Clark, *The Insect Integument*. Elsevier Scientific Publishing Company, 1976, ch. Energy Storage in Jumping Insects, pp. 421–443.
- [61] (2007). [Online]. Available: <http://web.mit.edu/6.777/www/matprops/pdms.htm>
- [62] J. C. Lotters, W. Olthuis, P. H. Veltink, and P. Bergveld, “The mechanical properties of the rubber elastic polymer polydimethylsiloxane for sensor applications,” *Journal of Micromechanics and Microengineering*, vol. 7, pp. 145–147, 1997.

- [63] (2007). [Online]. Available: <http://www.vitekres.com/vitekparylene.htm>
- [64] R. Mahadevan, M. Mehregany, and K. J. Gabriel, "Application of electric microactuators to silicon micromechanics," *Sensors and Actuators A - Physical*, vol. A21-A23, pp. 219–225, 1990.
- [65] M. J. Howard, Ed., *Elastomeric Materials*. San Diego, CA: The International Plastics Selector, 1977.
- [66] Y. Li and J. Unsworth, "Dynamic mechanical behaviours of epoxy insulating composites," in *Electrical Electronics Insulation Conference*, 1993, pp. 7–11.
- [67] C. M. Elvin, A. G. Carr, M. G. Huson, J. M. Maxwell, R. D. Pearson, T. Vuocolo, N. E. Liyou, D. C. C. Wong, D. J. Merritt, and N. E. Dixon, "Synthesis and properties of crosslinked recombinant pro-resilin," *Nature*, vol. 437, no. 13, pp. 999–1002, 2005.
- [68] P. Fiorini and J. Burdick, "The development of hopping capabilities for small robots," *Autonomous Robots*, vol. 14, no. 2-3, pp. 239–254, 2003.
- [69] Y. Suzuki and Y.-C. Tai, "Micromachined high-aspect-ratio parylene spring and its application to low-frequency accelerometers," *Journal of Microelectromechanical Systems*, vol. 15, no. 5, pp. 1364–1370, 2006.
- [70] Y.-C. Tung and K. Kurabayashi, "A single-layer pdms-on-silicon hybrid microactuator with multi-axis out-of-plane motion capabilities-part 1: design and analysis," *Journal of Microelectromechanical Systems*, vol. 14, no. 3, pp. 548–557, 2005.
- [71] A. M. Mehta and K. S. J. Pister, "Flexure-based two degree-of-freedom legs for walk-

- ing microrobots,” in *ASME International Mechanical Engineering Congress and Exposition*, 2006.
- [72] M. Last, S. Venkatraman, and K. S. J. Pister, “Out of plane motion of assembled microstructures using single-mask soi process,” in *Transducers*, 2005, pp. 684–687.
- [73] N. Dechev, W. L. Cleghorn, and J. K. Mills, “Microassembly of 3-d microstructures using compliant, passive microgripper,” *Journal of Microelectromechanical Systems*, vol. 13, no. 2, pp. 176–189, 2004.
- [74] R. Yeh, S. Hollar, and K. S. J. Pister, “Single mask, large force, and large displacement electrostatic linear inchworm motors,” *Journal of Microelectromechanical Systems*, vol. 11, pp. 330–336, 2002.
- [75] (2007). [Online]. Available: <http://www.memsrus.com/nc-mumps.soi.html>
- [76] R. Pelrine, R. Kornbluh, J. Joseph, R. Heydt, Q. Pei, and S. Chiba, “High-field deformation of elastomeric dielectrics for actuators,” *Materials Science and Engineering C*, pp. 89–100, 2000.
- [77] J. X. Gao, L. P. Yeo, M. B. Chan-Park, J. M. Miao, Y. H. Yan, J. B. Sun, Y. C. Lam, and C. Y. Yue, “Antistick postpassivation of high-aspect ratio silicon molds fabricated by deep-reactive ion etching,” *Journal of Microelectromechanical Systems*, vol. 15, no. 1, pp. 84–93, 2006.
- [78] M. Last, “Pick and place silicon on insulator microassembly,” Ph.D. dissertation, University of California, Berkeley, 2005.

- [79] (2007). [Online]. Available: <http://www.newscaletech.com/>
- [80] S. Hollar, A. M. Flynn, S. Bergbreiter, and K. S. J. Pister, “Robot leg motion in a planarized-soi, two-layer poly-si process,” *Journal of Microelectromechanical Systems*, vol. 14, pp. 725–740, 2005.
- [81] E. Sarajlic, E. Berenschot, N. Tas, H. Fujita, G. Krijnen, and M. Elwenspoek, “High performance bidirectional electrostatic inchworm motor fabricated by trench isolation technology,” in *Transducers*, vol. 1, 2005, pp. 53–56.
- [82] K. Oldham, J. Pulskamp, R. Polcawich, P. Ranade, and M. Dubey, “Thin-film piezoelectric actuators for bio-inspired micro-robotic applications,” in *19th International Symposium on Integrated Ferroelectrics*, 2007.
- [83] S. Hollar, “A solar-powered, milligram prototype robot from a three-chip process,” Ph.D. dissertation, University of California, Berkeley, 2003.
- [84] S. J. Timpe and K. Komvopoulos, “The effect of adhesion on the static friction properties of sidewall contact interfaces of microelectromechanical devices,” *Journal of Microelectromechanical Systems*, vol. 15, no. 6, pp. 1612–1621, 2006.
- [85] M. P. de Boer, D. L. Luck, W. R. Ashurst, R. Maboudian, A. D. Corwin, J. A. Walraven, and J. M. Redmond, “High-performance surface-micromachined inchworm actuator,” *Journal of Microelectromechanical Systems*, vol. 13, no. 1, pp. 63–74, 2004.
- [86] C. Bellew, S. Hollar, and K. S. J. Pister, “An soi process for fabrication of integrated solar cells, transistors and electrostatic actuators,” in *Transducers*, 2003.

- [87] K. Oldham, “Microdevices for vibration suppression in computer hard disk drives,” Ph.D. dissertation, University of California, Berkeley, 2006.
- [88] S. Pamidighantam, R. Puers, K. Baert, and H. A. C. Tilmans, “Pull-in voltage analysis of electrostatically actuated beam structures with fixed-fixed and fixed-free end conditions,” *Journal of Micromechanics and Microengineering*, vol. 12, pp. 458–464, 2002.
- [89] [Online]. Available: <http://www.atomicworkshop.co.uk>
- [90] A. Lal, R. Duggirala, and H. Li, “Pervasive power: A radioisotope-powered piezoelectric generator,” *Pervasive Computing*, 2005.
- [91] [Online]. Available: <http://www.clare.com/Products/SolarCell.htm>
- [92] B. A. Warneke and K. S. J. Pister, “An ultra-low energy microcontroller for smart dust wireless sensor networks,” in *IEEE International Solid-State Circuits Conference*, vol. 1, 2004, pp. 316–317.
- [93] [Online]. Available: <http://www.emmicroelectronic.com/Products.asp?IdProduct=215>
- [94] [Online]. Available: <http://www.dustnetworks.com/products/dn2510.shtml>
- [95] U. Srinivasan, M. A. Helmbrecht, R. S. Muller, and R. T. Howe, “Mems: some self-assembly required,” *Optics and Photonics News*, vol. 13, no. 11, pp. 20–56, 2002.
- [96] [Online]. Available: <http://www.hasbro.com/playskool/weebles/>

- [97] X. Yang, C. Grosjean, and Y.-C. Tai, "Design, fabrication, and testing of micromachined silicone rubber membrane valves," *Journal of Microelectromechanical Systems*, vol. 8, pp. 393–402, 1999.
- [98] E. Sarajlic, E. Berenschot, G. Krijnen, and M. Elwenspoek, "Versatile trench isolation technology for the fabrication of microactuators," *Microelectronic Engineering*, vol. 67-68, pp. 430–437, 2003.
- [99] Y. P. Jaecklin, C. Linder, J. Brugger, N. F. de Rooij, J.-M. Moret, and R. Vuilleumier, "Mechanical and optical properties of surface micromachined torsional mirrors in silicon, polysilicon and aluminum," *Sensors and Actuators A - Physical*, vol. 43, pp. 269–275, 1994.
- [100] S. Hur, S. I. Hong, and D. kil Shin, "Mechanical properties of photosensitive polyimide film by nanoindentation and microtensile test," *Key Engineering Materials*, vol. 297-300, pp. 237–243, 2005.
- [101] A. M. Flynn, "Gnat robots (and how they will change robotics)," in *IEEE Micro Robots and Teleoperators Workshop*, Hyannis, MA, 1987.
- [102] A. M. Flynn, L. S. Tavrow, S. F. Bart, R. A. Brooks, D. J. Ehrlich, K. R. Udayakumar, and L. E. Cross, "Piezoelectric micromotors for microrobots," *Journal of Microelectromechanical Systems*, vol. 1, no. 1, pp. 44–51, 1992.
- [103] U. Scarfogliero, C. Stefanini, and P. Dario, "A bioinspired concept for high efficiency locomotion in micro robots: the jumping robot grillo," in *IEEE International Conference on Robotics and Automation*, 2006, pp. 4037–4042.

- [104] T. E. Wei, G. M. Nelson, R. D. Quinn, H. Verma, and S. L. Garverick, "Design of a 5-cm monopod hopping robot," in *IEEE International Conference on Robotics and Automation*, 2000, pp. 2828–2833.